Experimental realization of atomtronic circuit elements in non-equilibrium ultracold atomic systems

by

Seth C. Caliga

B.A., University of Colorado, 2009

M.S., University of Colorado, 2013

A thesis submitted to the

Faculty of the Graduate School of the

University of Colorado in partial fulfillment

of the requirements for the degree of

Doctor of Philosophy

Department of Physics

2016

This thesis entitled:
Experimental realization of atomtronic circuit elements in non-equilibrium ultracold atomic systems
written by Seth C. Caliga
has been approved for the Department of Physics

_____

Dana Z. Anderson

_____

Murray J. Holland

Date _____

The final copy of this thesis has been examined by the signatories, and we find that both the content and the form meet acceptable presentation standards of scholarly work in the above mentioned discipline.

Caliga, Seth C. (Ph.D., Physics)

Experimental realization of atomtronic circuit elements in non-equilibrium ultracold atomic systems

Thesis directed by Dana Z. Anderson

Research in the field of atomtronics aims to develop a new paradigm for the use of ultracold atomic systems in a manner that mimics the functionality of electronic circuits and devices. Given the ubiquity of the electronic transistor and its application to a vast array of signal processing tasks, the development of its atomtronic counterpart is of significant interest. This dissertation presents the experimental studies of two atomtronic circuit elements: a battery and transistor. Experiments are conducted in an atom-chip-based apparatus utilizing hybrid magnetic and optical trapping techniques that enable one to "pattern" atomtronic circuit elements. An atomtronic battery is realized in a double-well trapping potential in which a finite-temperature Bose-Einstein condensate is prepared in a non-equilibrium state to generate thermodynamic gradients that drive atom current flow. Powered by the atomtronic battery, a triple-well atomtronic transistor is demonstrated, and quasi-steady-state behavior of the device is characterized. Results are found to be in agreement with a semi-classical model of the transistor that is also used to study the active properties of the device, including current gain. Based on these results, future directions regarding signal processing operations are proposed.

Dedication

To my wife, Kristen, and parents, David and Tina.

In loving memory of Grandma Margaret and Grandpa Charles

Acknowledgements

It goes without saying that the work contained in a Ph.D. dissertation is not the result of a singular effort. First among those who deserve recognition is my wife, Kristen, who has stood by my side since the very beginning. Her unending encouragement significantly eased the stresses of graduate school. I cannot thank her enough for the sacrifices that she made along the way to support the two of us. She adds balance to my life, keeping me focused on my goals while also providing enough distraction to keep me sane. Next are my parents, David and Tina, who raised me in an environment that encouraged the pursuit of any activity that intrigued me. Their love and guidance have been invaluable. A big thank you to my sister, Sasha, and her beautiful family, my awesome in-laws, Dave and Pattie, along with all of my extended family in both TX and CO for their continued support. I would also like to acknowledge my best friend, Kyle Thatcher. After living together for many years (and a few emergency room visits) he has become a brother to me.

Thank you to my advisor, Dana Anderson, who has overseen my development as an experimental physicist for nearly nine years. I am grateful that he recognized my passion for physics during his undergraduate optics lab course and invested his time to help me pursue my dream. He has afforded me a great deal of freedom in the lab, allowing me to steer the research path while ensuring that I didn't stray too far off course. He also taught me the importance of both written and verbal scientific communication, and impressed upon me his knack for conjuring intuitive descriptions of complex physics concepts.

While working in Dana's lab, I had the pleasure of working alongside many fantastic individuals, some of whom have moved on to bigger and better things. My first mentor,

Stephen Segal, exhibited unyielding patience as I cut my teeth in the research world. I consider myself lucky to have added his methodical approach to apparatus design and construction to my own toolbox. Evan Salim's intuition for all things mechanical never ceases to amaze me. Even more so does his range of talents outside of the lab. My first postdoc, Dan Farkas, shared just a sliver of his knowledge with me during the time we overlapped at JILA, including the ins and outs of laser cooling, the importance of proper electrical shielding and cable construction, and a healthy appreciation for hip hop. Leslie Czaia, with her steady hands and immaculate attention to detail, helped create the numerous vacuum chambers used throughout my research. In addition to her technical skills, I greatly appreciate Leslie's outlook on life and the many interesting conversations that we shared. Lastly, Kai Hudek, a man after my own heart. The knowledge that Kai passed on to me is difficult to summarize. He continues to be an inspiring role model and a true friend.

In the latter half of my time at JILA, I had the pleasure of working with several talented graduate students. I could not have found two better labmates and friends than Cameron Straatsma and Carrie Weidner. The significant contributions of Cameron are reflected in much of the work presented in this dissertation. As an optical engineer, Cameron's skill set was originally quite different from my own. In the end, I hope to have taught him as much physics as he taught me about programming and optics. I wish Cameron the best of luck as he continues on the atomtronics experiment. While I did not work with Carrie directly, her humor and passion for physics (and the Chicago Cubs) were contagious. I will miss the hours of ice time that the three of us spent together on our IM hockey team (Champions, Spring 2016!). Thank you also to my second postdoc, Hoon Yu, fellow graduate students Brad Dinardo, Doug Bopp, Ava "Queso" Ashby, Phoebe Tengdin, and Evolene Premillieu, and undergraduate, Taylor Froelich, for keeping life in the lab interesting.

Outside of Dana's lab, JILA houses a myriad of talented individuals who helped me along the way. Members of the instrument shop Hans Green, Blaine Horner, Todd Asnicar, Tracy Keep, Kim Hagen, Ariel Paul, and of course Kyle Thatcher, have tolerated innumerable

questions regarding machining and mechanical design for which I am most grateful. The same appreciation goes to the electronics shop staff. Thanks to Terry Brown, Carl Sauer, and James Fung-A-Fat, for always pointed me in the right direction when a circuit was misbehaving.

I also had the pleasure of collaborating with a handful of excellent people. Alex Zozulya helped develop a great deal of the theory presented in this dissertation. Imaging guru Jay Margolis of Infinity Photo-Optical was instrumental in developing the optical system used in my research. David Van Wie of Boulder Labs developed the LiveAtom software used to model our atom chip traps. Also, Marine Pigneur whose visit to JILA may have been short but resulted in a lasting friendship.

Finally, I would like to thank Wes Mangney, my first mentor in physics, who inspired many young minds and was taken from us too soon. Both he and Kevin LaBella helped me to discover my passion for physics at Air Academy High School.

Contents

Chapter

Figures

Figure

Chapter 1

Introduction

1.1 Motivation

The historical development of devices for the purpose of generating and manipulating electronic signals arguably began following Thomas A. Edison's invention of the lightbulb, at the end of the 19th century [1]. Shortly after its invention, more complicated light bulbs enclosing multiple electrically isolated filaments were constructed, leading Owen W. Richardson to discover thermionic emission from hot bodies, previously known as the Edison effect [2]. By 1904, John A. Fleming invented the first vacuum tube specifically for the purpose of measuring AC signals and signal rectification (see Figure 1.1(a)), marking the beginning of electronic signal processing. Fleming's thermionic valve gave way to many successive iterations of vacuum tube amplifier designs, including triodes and pentodes that can still be found in the amplifiers of today's audio enthusiast. Signal processing technology took its next big leap in 1948, with the invention of the semiconductor transistor [3], at Bell Laboratories (see Figure 1.1(b)), which ushered in the era of integrated circuitry and contemporary electronics.

Moore's law observes that the number of transistors on an integrated circuit doubles approximately every two years. Quite apart from a comment about the remarkable evolution of electronics and fabrication techniques, Moore's law highlights the cardinal role of the transistor in modern technology. What is it that distinguishes the transistor from other electronic elements? The canonical transistor is a three-terminal device that derives its

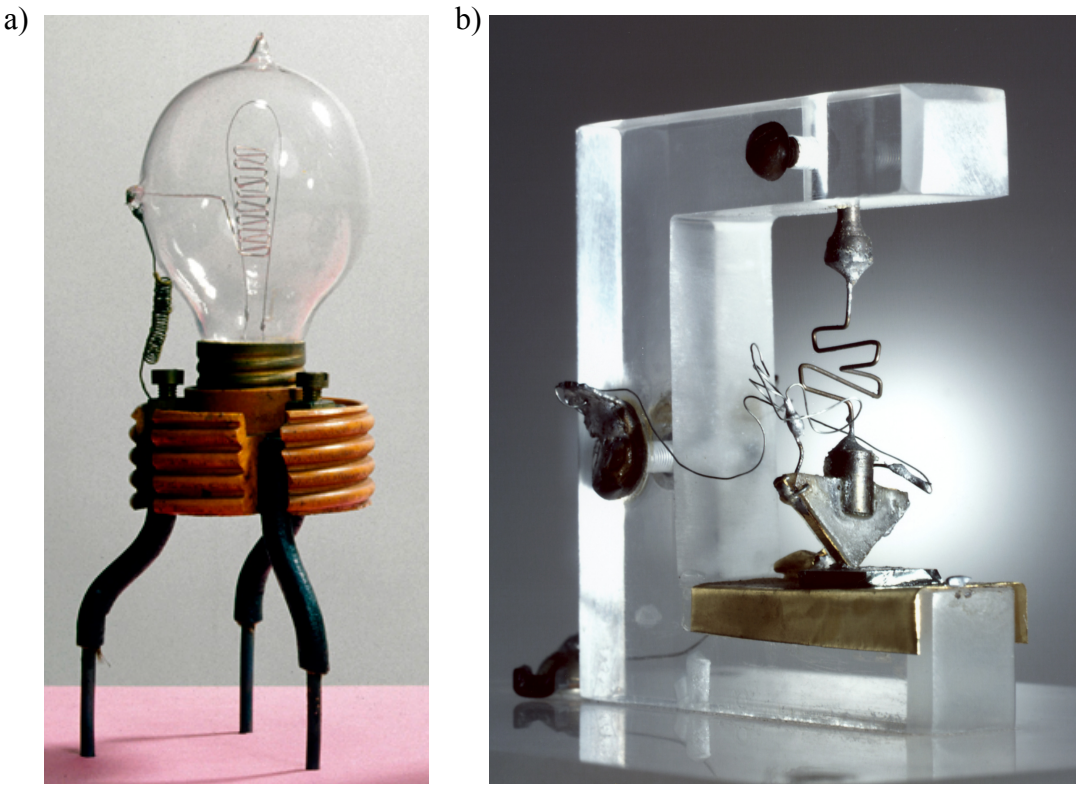

Figure 1.1: a) Original thermionic valve invented by J. A. Fleming [4]. When heated by an alternating electric current (AC), thermally excited electrons are ejected from the coiled filament in a process known as thermionic emission [5, 6]. The second, straight filament in the tube acts as a sink to the liberated electrons when charged positively, resulting in a measurable current between the two wires. b) Original point contact transistor invented at Bell Laboratory by J. Bardeen, W. H. Brattain, and W. Shockley [3]. This somewhat haphazard looking device was constructed with a PN-doped slab of Germanium (Ge) resting atop a gold sheet, which serves as the base contact of the transistor [7]. Two gold additional gold contacts, named the emitter and collector, are supported by a plastic wedge and seen pressed against the Ge slab by a vertical metal spring-like structure.

utility by enabling a small electric current or voltage to control a large current. In particular, transistors are active devices that provide electrical gain—gain that can be used to amplify a signal, sustain coherent oscillation, perform switching, provide storage, and implement logic. Such are a few of the many functions that reflect the ubiquity of the transistor in modern electronics.

Along with the aforementioned statements about transistors, research thrusts in the field of quantum signal and information processing (see References [8, 9]) are ongoing. These endeavors motivate research towards the realization of a device capable of performing the classical signal processing duties of electronic transistors in the realm of quantum mechanical signals. Therefore, the road towards developing quantum signal processing technology brings us back to vacuum tubes, or should I say ultra high vacuum (UHV) chambers, in which we seek to realize an atomtronic transistor. At the heart of the Anderson lab atomtronics apparatus is the double-MOT vacuum chamber shown in Figure 1.2. The atom chip that forms the top wall of the vacuum chamber is designed specifically for the experiments described in this dissertation. In particular, it includes a transparent window that, in conjunction with external optics, enables the projection of optical potentials with micron length-scale features onto the magnetic potential generated by the atom chip. Just as the layout of electronic circuit dictates its functionality, this optical potential determines the flow and dynamics of ultracold atoms as they propagate through the atomtronic system. The work described throughout this dissertation represent one vein of research in the growing field of atomtronics.

1.2 Atomtronics

The field of atomtronics has emerged in tandem with the development of experimental techniques in the field of atomic, molecular, and optical physics (AMO), that allow one to create and manipulate the state of ultracold atoms. Utilizing said atoms in place of electrons, atomtronics lives in a challenging arena of physics involving many-body, interacting, and

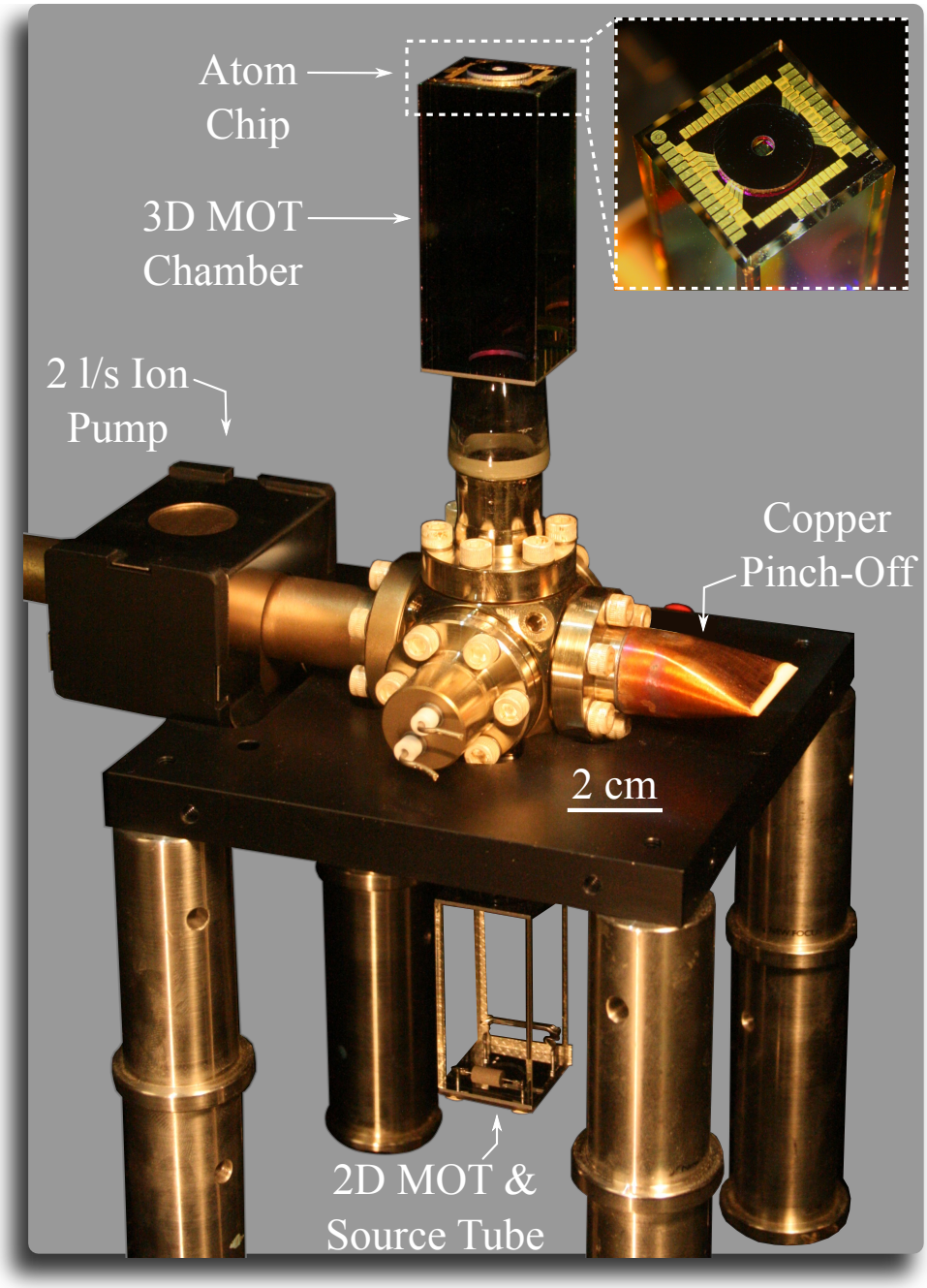

Figure 1.2: Double-MOT vacuum chamber used to conduct atomtronics experiments. The inset shows the atom chip, which forms the upper wall of the vacuum chamber and is used to form the confining magnetic potentials in the atomtronics experiments. Once constructed and baked-out to pressures $< 10^{-10}$ torr, the vacuum chamber is pinched off from a larger station, after which the UHV pressure required for experiments is maintained solely by a 2 l/s ion pump and other passive gettering elements. The atom source is located in the lower of the two glass cells, labeled "2D MOT & Source Tube", in which initial laser cooling techniques produce a stream of pre-cooled atoms upwards, into the 3D MOT chamber. The remainder of the experiment occurs in this upper chamber, which appears dark in the figure due to an anti-reflection coating. Additional information regarding the construction and functionality of the Double-MOT vacuum chamber can be found elsewhere [10, 11, 12, 13].

open quantum systems in non-thermal equilibrium. It is likely not possible to develop complete descriptions of any but the simplest atomtronic circuits. Indeed, most theoretical and experimental works thus far involve fully quantum atomtronic circuits, i.e., operating as a closed system that is described by unitary evolution [14, 15, 16, 17, 18, 19, 20]. Transistor-like gain, on the other hand, requires an open system approach [21, 22, 23, 24, 25, 26]. Moreover, accepting the connection between information processing and entropy change suggests that dissipation and heat generation are fundamental aspects to be taken into account in atomtronic circuit design [27, 28, 29, 30, 31]. In classical circuits, electrons are strongly coupled to the thermal environment of the medium in which they propagate. Ultracold atomic systems, by contrast, are isolated from the surrounding environment such that dissipation and heat generation contribute to the state of the system. To make headway toward the understanding of atomtronic circuits one can either treat such dissipation as a perturbation to an otherwise quantum system, or introduce quantum effects to an otherwise classical system. Both can be instructive.

1.3 The pursuit of an atomtronic transistor

Driving an interest in atomtronics is the possibility of developing a paradigm for addressing problems in quantum signal and information processing that parallels the power of electronics in the classical realm. Thus, an atomtronic version of transistor action has been a central theme of research in atomtronic devices and circuits. Transistor-like behavior has been studied in both cold and ultracold atomic systems revealing a variety of approaches for realizing an atomtronic transistor. The mechanisms responsible for transistor action explored thus far can be distinguished into three categories: (1) interatomic interactions of a single species in a single state, A, i.e., A_{in} controls A_{out} [21, 22, 23, 24]; (2) Interatomic interactions of two species or states, A and B, i.e., B_{in} controls A_{out} [25, 32]; and, (3) an external coupling field, C, that drives internal state transitions of atom A, i.e., C_{in} controls A_{out} [33, 34]. The atomtronic transistor described in this work falls into the first category

and follows from the analogy with electronic transistors, which operate based on the flow or buildup of a single carrier species, namely electrons. The first two categories, both of which derive functionality from interatomic interactions, are differentiated solely by experimental implementation. By introducing a second species or state, B, to control the flow of A, the transistor system becomes more complex, requiring the superposition of two species- or state-dependent trapping potentials. By contrast, the third category utilizes a coupling, C, other than atoms to control the flow of A. In such systems the coupling strength of field C is converted into the flow of atoms A, a process akin to transduction. As in electronics, the development of various types of transistors for specific applications emphasizes their utility.

1.4 Fundamental atomtronic circuit elements

The experimental work presented in this dissertation characterizes the behavior of two atomtronic devices and represents a step towards the development of devices that can be readily applied to the challenges of quantum signal processing. The first device, often overlooked due to its integral role in nearly every circuit, is a power supply. In the context of the experiments presented here, a finite-temperature Bose-Einstein condensate (BEC) of Rubidium 87 atoms (^{87}Rb) is stored in a double-well potential. This devices is more aptly referred to as a battery, providing both particles and energy to the connected circuit components in order to maintain circuit functionality, until the stored energy of the BEC is depleted. The atomtronic battery, when considered as part of the entire circuit, embodies a system that is far from thermodynamic equilibrium, with many atoms stored in a reservoir, waiting to be doled out to the rest of the circuit as required. Figure 1.3(a) shows an *in situ* image of the atomtronic battery as it outputs a current of ultracold atoms. In the end, all but the most mundane circuits, electronic or otherwise, operate in a state of non-equilibrium, and it is the roll of the power supply to provide and sustain the potential gradients that drive circuit operation. The second device is, of course, an atomtronic transistor, which can be seen in Figure 1.3(b).

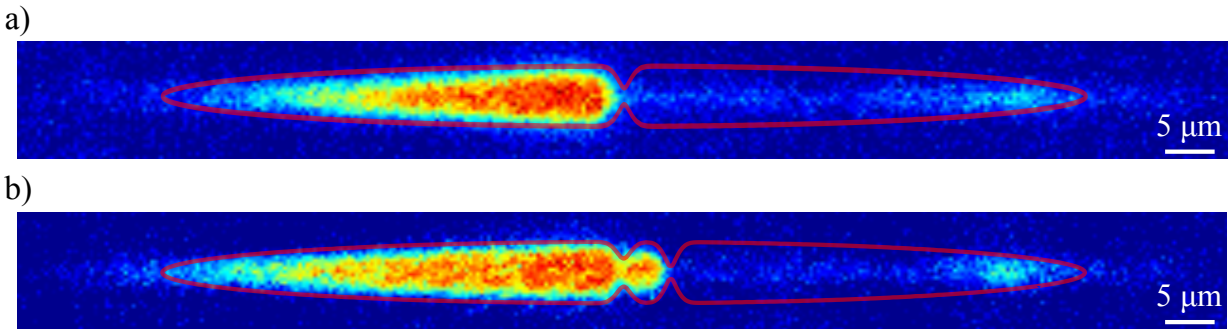

Figure 1.3: a) *In situ* image of the atomtronic battery illustrating the current output from the reservoir well due to the non-equilibrium distribution of atoms in a double-well potential (indicated by the red outline of a representative energy contour) that is separated by a repulsive barrier with finite height. b) A similar image, this time showing the triple-well transistor, illustrates the transport dynamics between the three wells, separated by barriers of differing height, result in transistor-like behavior.

The name "transistor," an amalgam of "transfer" and "resistor," refers to the effective resistance, or transresistance of the device when treated as a two-port, input/output device. It is precisely that this resistance can be negative that corresponds to the gain that transistors are known for [35, 36]. More than just a conceptual convenience, the negative resistance of a transistor is a thermodynamic reality: the transresistance corresponds to negative power dissipation during current flow [37]. Here, the concepts of negative transresistance and gain are applied to the atomic system to investigate the principles of an atomtronic transistor where transistor-like behavior arises due to the interplay of atom currents between the three wells.

1.5 Dissertation outline

The remainder of this dissertation is organized as follows: Chapter 2 presents the theoretical treatment of Bose-Einstein condensates, as it pertains to the experimental system. Additionally, a semiclassical treatment of the triple-well atomtronic transistor is presented that analyzes the system in steady-state and calculates relevant transistor-like properties, such as current gain and negative transconductance. Chapter 3 provides an overview of the theory and development of a key component in the experimental apparatus, the atom chip. As executed, the atomtronics experiment presents experimental challenges as far as atom chip development is concerned. These difficulties were overcome by including an optically transparent window, which enables the simultaneous use of optical potentials in conjunction with the magnetic potential generated by the atom chip. Chapter 4 then describes the processes of both imaging atoms trapped in the magnetic potential as well as the projection of dynamic optical potentials that define the functionality of our atomtronic devices. Finally, Chapter 5 presents the experimental realization of an atomtronic battery, which is characterized according to a Thévenin equivalent circuit. The battery is subsequently used to power the atomtronic transistor in order to study the transport dynamics of atoms between the three wells of the potential and the resulting quasi-steady-state behavior of the

system. Chapter 6 provides some concluding remarks, including the future direction of the atomtronics experiment.

Chapter 2

Theory

The atomtronic devices studied throughout this dissertation rely on the non-linear behavior of interacting Bose gases at finite-temperature. This chapter covers the salient concepts of trapped BEC systems and their role in transistor-like behavior. To start, a theoretical description of Bose-Einstein condensates is provided, beginning from the idealized case of a non-interacting BEC. Building upon this simplified description, the influences of both intraparticle interactions as well as finite-temperature effects are included to the description of the trapped gas. Next, a semiclassical description of an atomtronic transistor is presented. Within this theory, we begin by determining the steady-state behavior of finite-temperature ensembles trapped within a triple-well potential. Based on the steady-state characteristics, transistor-like current gain and power dissipation are explored. Finally, the theoretical basis for generating the hybrid magnetic and optical triple-well potential is provided.

2.1 Theoretical description of Bose-Einstein condensates

Following the experimental realization of BEC, the field of ultracold atomic physics has burgeoned, experiencing a thrust towards the study of quantum phenomena in many-body systems, both in the pursuit of fundamental physics research [38], as well as real-world applications [39, 40]. This chapter begins by introducing the salient equations that describe trapped, non-interacting BECs that can be found in many statistical mechanics texts [41]

and others dedicated solely to BEC physics [42, 43]. Corrections to these equations are then discussed, which account for finite size and temperature effects as well as interatomic interactions [43, 44]. The expressions provided in this section are then used in Section 2.2 to derive analytic relations that describe steady-state behavior in a triple-well transistor-like potential.

2.1.1 Non-interacting Bose-Einstein condensates

While the atomic systems studied throughout this dissertation rely heavily on the interactions between atoms, it is informative to start from the simplest scenario in which interactions are not considered in order to develop a notion for the behavior of trapped Bose gases. At temperatures, T, that are well above the onset of BEC, the distribution of particle energies, ϵ, within the gas is approximately described by the Boltzmann distribution,

$$f_{MB}(\epsilon) \simeq \frac{1}{\mathrm{e}^{(\epsilon-\mu)/k_B T}}, \tag{2.1}$$

where the chemical potential $\mu \ll \epsilon$ and k_B is the Boltzmann constant. As the temperature of the gas is reduced further, quantum statistics become non-negligible and the bosonic nature of the atoms begins to play a dominant role. In this ultracold regime, the distribution of particle energies is described by the Bose-Einstein (BE) distribution,

$$f_{BE}(\epsilon) = \frac{1}{\mathrm{e}^{(\epsilon-\mu)/k_B T} - 1}, \tag{2.2}$$

which accounts for macroscopic occupation of the ground state of the system and the formation of a BEC.

When the gas is confined in an externally applied potential, the density of states of the trap modifies the distribution and requires the inclusion of the energy level degeneracy, $g(\epsilon)$. Our atomtronics experiments are conducted in an anisotropic 3-dimensional potential that can be described by

$$V(\mathbf{r}) = \frac{m}{2}\left(\omega_x^2 x^2 + \omega_y^2 y^2 + \omega_z^2 z^2\right), \tag{2.3}$$

where x_i and ω_i are the three spatial coordinates and corresponding harmonic trapping frequencies, respectively, and m is the atomic mass. The length scales of the potential are then defined by the harmonic oscillator lengths, $a_i = \sqrt{\hbar/m\omega_i}$, and the overall confinement is characterized by the geometric mean trap frequency $\bar{\omega} = (\omega_x\omega_y\omega_z)^{1/3}$. This potential has a degeneracy factor

$$g(\epsilon) = \frac{\epsilon^2}{2(\hbar\bar{\omega})^3}, \tag{2.4}$$

where $\hbar$ is the reduced Planck constant [43]. Given the degeneracy factor, the total particle number is obtained by integrating over the distribution of particles,

$$N = \int_0^\infty d\epsilon \frac{g(\epsilon)}{\mathrm{e}^{(\epsilon-\mu)/k_BT} - 1}. \tag{2.5}$$

The transition point between a gas that behaves classically and the onset of quantum statistics, i.e., macroscopic occupation of the ground state, is determined by the critical temperature, T_c. In the absence of interatomic interactions, $T = T_c$ when $\mu = 0$ and $N = N_{th}$. Solving Equation (2.5) under these conditions, one finds

$$N = N_{th} = \int_0^\infty d\epsilon \frac{g(\epsilon)}{\mathrm{e}^{\epsilon/k_BT_c} - 1}, \tag{2.6}$$

$$= \frac{\Gamma(3)\zeta(3)}{2}\left(\frac{k_BT_c}{\hbar\bar{\omega}}\right)^3, \tag{2.7}$$

where N_{th} is the number of thermally excited atoms at the threshold of condensation, Γ is the gamma function, and ζ is the Riemann zeta function. The integral in Equation (2.6) is evaluated according to Appendix D in Reference [41]. Solving Equation (2.7) for the critical temperature yields

$$T_c = \frac{\hbar\bar{\omega}}{k_B}\sqrt[3]{\frac{N}{\zeta(3)}}. \tag{2.8}$$

From Equation (2.7) it is clear that the total number of atoms scales relative to the ratio $\tilde{T} \equiv T/T_c$ and is related to the number of thermally excited atoms by $N_{th} = N\tilde{T}^3$, which leads to the expression for the condensate fraction,

$$\frac{N_c}{N} = 1 - \tilde{T}^3. \tag{2.9}$$

The total energy of the trapped atomic ensemble can be calculated in a similar manner to the total atom number by including the energy of each state in the integrand,

$$E = \int_0^\infty d\epsilon \frac{\epsilon\ g\left(\epsilon\right)}{\mathrm{e}^{(\epsilon-\mu)/k_B T} - 1}. \tag{2.10}$$

Solving Equation (2.10) with $\mu = 0$ yields the energy of the condensed phase,

$$E_c = 3Nk_BT\frac{\zeta(4)}{\zeta(3)}\tilde{T}^3. \tag{2.11}$$

From E, the heat capacity can be calculated according to the relation $C = \partial E/\partial T$. Therefore, the heat capacity of the condensed phase is

$$C_c = 12Nk_B\frac{\zeta(4)}{\zeta(3)}\tilde{T}^3. \tag{2.12}$$

To determine the energy of the normal phase Equation (2.10) is solved given the approximation $f_{BE}(\epsilon) \simeq \exp[-(\epsilon-\mu)/k_BT] + \exp[-2(\epsilon-\mu)/k_BT]$ [43], which yields

$$E_{th} = 3Nk_BT\left(1 - \frac{\zeta(3)}{16\tilde{T}^3}\right), \tag{2.13}$$

and the corresponding heat capacity,

$$C_{th} = 3Nk_B\left(1 + \frac{\zeta(3)}{8\tilde{T}^3}\right). \tag{2.14}$$

Equations (2.12) and (2.14) behave differently as $T \to T_c$, which causes the heat capacity to peak at the critical temperature, indicating the transition between normal and condensed phases. As the temperature becomes large, $T \gg T_c$, one recovers the classical limits, $E = 3Nk_BT$ and $C = 3Nk_B$.

In addition to thermodynamic variables of the gas, the in-trap spatial distribution of the atoms plays a role in the behavior of our atomtronic systems. Furthermore, when imaging atoms *in situ*, the spatial distribution of the atoms can be used to extract quantitative information about the atomic ensemble. As one might expect, the condensed and thermal components of the gas exhibit different spatial distributions. Whereas the thermal gas is

best described as particle-like, the condensate behavior is wave-like, since the intraparticle spacing is on the order of the de Broglie wavelength. The thermal cloud density is determined by Boltzmann statistics, with $\exp[\epsilon/k_BT] \rightarrow \exp[V(\mathbf{r})/k_BT]$, and exhibits Gaussian characteristics,

$$n_{th} = \frac{N}{\pi^{3/2}\sigma_x\sigma_y\sigma_z} \mathrm{e}^{-x^2/2\sigma_x^2 - y^2/2\sigma_y^2 - z^2/2\sigma_z^2}. \tag{2.15}$$

Thus, the spatial extent along each direction of the trap is dictated by the characteristic width, $\sigma_i = \sqrt{2k_BT/m\omega_i^2}$, which relates the thermal energy of the atoms to the strength of the harmonic confinement. The momentum distribution is also Gaussian but isotropic and determined by the mean thermal energy,

$$p_{th} \propto \mathrm{e}^{p^2/2mk_BT}. \tag{2.16}$$

Both the spatial and momentum distributions of trapped thermal gases are used extensively in the simulations discussed in Section 5.4.1. The spatial distribution of the condensate is addressed in the next section under the Thomas-Fermi (TF) approximation.

Near the critical temperature and below, the gas can be described by the semiclassical distribution function,

$$f(\mathbf{r},\mathbf{p}) = \frac{1}{\mathrm{e}^{(p^2/2m + V(\mathbf{r}) - \mu)/k_BT} - 1}, \tag{2.17}$$

in which atoms occupy a phase space $d\mathbf{r}d\mathbf{p}$. The density of thermally excited atoms is then given by

$$\begin{aligned} n_{th}(\mathbf{r}) &= \int \frac{dp}{(2\pi\hbar)^3} f(\mathbf{r},\mathbf{p}), \\ &= \frac{g_{3/2}(z(\mathbf{r}))}{\lambda_{th}}, \end{aligned} \tag{2.18}$$

where $z = \exp[-(V(\mathbf{r}) - \mu)/k_BT]$ is the fugacity, $\lambda_{th} = \sqrt{2\pi\hbar^2/mk_BT}$ is the de Broglie wavelength, and $g_{3/2}$ is the polylogarithm function for atoms in a 3D harmonic oscillator potential. Whereas the Boltzmann distribution is often trivial to integrate, the same operations on the Bose-Einstein distribution produce polylogarithm functions, which are described in

depth in Appendix D of Reference [41] and Appendix B.1 in Reference [45]. Equation (2.18) provides an intuition to the behavior of Bose gases near the transition temperature where the effects of Bose enhancement manifest as a peak in the central density of the cloud.

2.1.2 Interacting Bose-Einstein condensates at zero-temperature

While the expressions introduced in Section 2.1.1 are sufficient in describing a non-interacting gas, the theoretical work described in Section 2.2 and experiments described in chapter 5 utilize ^{87}Rb atoms. In its electronic ground state, ^{87}Rb is a neutral species, devoid of long-range interaction mechanisms. However, as a massive boson, short range interactions via collisions are sufficient to alter the characteristics described in the previous section and provide non-linear behavior that is fundamental to our atomtronic systems.

The collision process can be understood via scattering theory, which is described thoroughly in chapter 5 of Reference [43]. At the low temperatures of the atomic ensembles we consider, the scattering cross-section is solely s-wave and given by

$$\sigma_s = 8\pi a_s^2, \tag{2.19}$$

where $a_s = 95.47a_0 \approx 5$ nm is the s-wave scattering length of ^{87}Rb atoms in the $|F = 2, m_F = 2\rangle$ state, and a_0 is the Bohr radius. The scattering process can be viewed as an effective contact interaction between two atoms and is well characterized by the Lippmann-Schwinger (LS) equation. In the Born approximation, the LS equation predicts an effective pseudopotential,[1] $U_{eff} = g\delta(\mathbf{r} - \mathbf{r}')$, with an interaction strength

$$g = \frac{4\pi\hbar^2 a_s}{m}, \tag{2.20}$$

which is equivalent to the scattering matrix at zero energy [43].

[1] The effective interaction due to collisions is typically treated according to the regularized zero-range pseudopotential, $V_{eff}\psi = (4\pi\hbar^2 a_s/m)\delta(\mathbf{r})\partial(r\psi)/\partial r$, which corrects for the divergent behavior of the Dirac delta function as $r \to 0$ [43, 46]. Treating the collision process in the Born approximation, which neglects the scattered wave, simplifies the effective interaction to $U_{eff} = (4\pi\hbar^2 a_s/m)\delta(\mathbf{r})$, since the role of $\partial(r\psi)/\partial r$ is to eliminate the contribution of the scattered wave to the potential.

Given this scattering interaction, one can accurately describe the condensed phase using the effective many-body Hamiltonian,

$$H = \sum_{i=1}^{N} \left(-\frac{\hbar^2 \nabla_i^2}{2m} + V(\mathbf{r}_i) \right) + g \sum_{i<j} \delta(\mathbf{r}_i - \mathbf{r}_j). \tag{2.21}$$

Constraining the solution of the wave function by the relation $\partial E/\partial N = \mu$ ensures consistency between E and N and yields the time independent Gross-Pitaevskii equation,

$$\left[-\frac{\hbar^2 \nabla^2}{2m} + V(\mathbf{r}) + g|\psi(\mathbf{r})|^2 \right] \psi(\mathbf{r}) = \mu \psi(\mathbf{r}), \tag{2.22}$$

where the eigenvalue for the non-linear condensate eigenstate $\psi(\mathbf{r})$ is the chemical potential [45]. The GPE is a powerful tool that can be used to model the behavior of zero-temperature gases, and simulation techniques are well documented [47]. If the contribution due to the kinetic energy is small compared to the potential or collision pseudopotential, then Equation (2.22) can be reduced to

$$\mu \psi(\mathbf{r}) = \left[V(\mathbf{r}) + g|\psi(\mathbf{r})|^2 \right] \psi(\mathbf{r}), \tag{2.23}$$

under the well-known Thomas-Fermi (TF) approximation. The TF approximation holds true for trapped clouds that satisfy $Na_s/\bar{a} \gg 1$, where $\bar{a} = \sqrt{\hbar/m\bar{\omega}}$ is the mean harmonic oscillator length [43]. Since the atoms are confined within a harmonic potential, the TF approximation leads to an inverted parabola density profile of the condensate,

$$n_c(\mathbf{r}) = \frac{\mu - V(\mathbf{r})}{g}, \tag{2.24}$$

with TF widths $R_i = \sqrt{2\mu/m\omega_i}$. The total atom number in the condensate can then be determined by integrating n_c across R_i, yielding

$$N_c = \frac{8\pi}{15} \frac{\mu}{g} \left(\frac{2\mu}{m\bar{\omega}^2} \right)^{3/2}. \tag{2.25}$$

Solving for μ, one obtains the TF approximation for the chemical potential,

$$\mu = \frac{\hbar\bar{\omega}}{2} \left(\frac{15 N_c a_s}{\bar{a}} \right)^{2/5}, \tag{2.26}$$

which is used throughout the remainder of this dissertation.

2.1.3 Corrections due to finite temperature, size, and interatomic interactions

Corrections to the thermodynamic quantities introduced in Section 2.1.1 arise due to finite number of particles, intraparticle interactions, and finite temperature. Throughout the work covered in this dissertation, the atomic systems that are considered have temperatures below the critical temperature yet higher than the effective temperature associated with interatomic interactions, $T_0 = 2\mu/7Nk_B$. In this regime, $T_c \gtrsim T > T_0$, the two components of the cloud can be treated separately under the Hartree-Fock (HF) approximation [43, 45]. Using this description of the system, the presence of a condensate produces an effective potential known as the mean field,

$$U_{HF}(\mathbf{r}) = V_{trap}(\mathbf{r}) + 2g\left[n_c(\mathbf{r}) + n_{th}(\mathbf{r})\right], \tag{2.27}$$

which is experienced by the thermal cloud. In typical situations the thermal density of the trapped gas can be neglected, owing to the fact that $n_{th}(\mathbf{r}) \ll n_c(\mathbf{r})$ [45].

One can now consider the in-trap density distribution of an interacting Bose gas at finite temperature using Equations (2.18) and (2.24). The thermal cloud density depends on the fugacity,

$$z_{HF}(\mathbf{r}) = \mathrm{e}^{-gn_c(\mathbf{r})/k_BT}, \tag{2.28}$$

that now includes the repulsive, positive-valued, TF chemical potential within $n_c(\mathbf{r})$, the zero-temperature condensate density from Equation (2.24). Figure 2.1 shows a plot of the thermal cloud density for various temperatures that exemplify the behavior of the finite-temperature, interacting gas. The three curves illustrate the stark contrast in behavior at $T > T_c$, $T = T_c$, and $T < T_c$. At temperatures above the critical temperature, the thermal cloud density has a Gaussian distribution. However, as the cloud is cooled to the critical temperature, Bose enhancement is noticeable as the ground state begins to acquire higher occupancy. Well below the critical temperature, where the chemical potential is positive, the mean field potential results in the repulsion of thermal atoms by the condensate and reveals

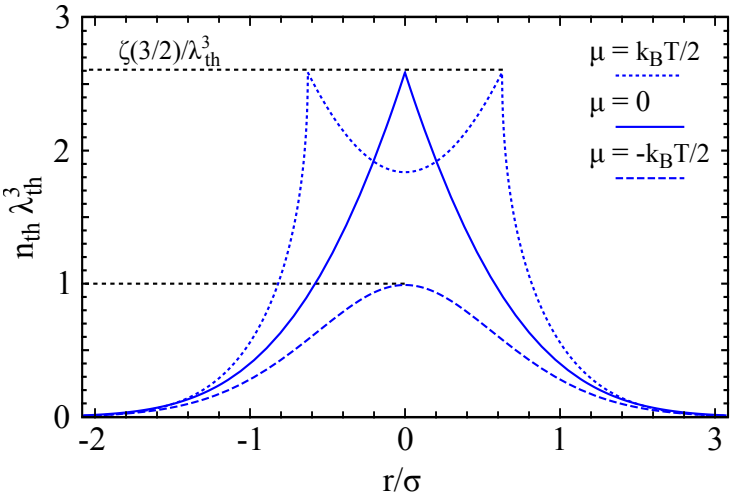

Figure 2.1: Thermal cloud density for clouds at temperatures $T > T_c$, $T = T_c$, and $T < T_c$. The density is determined from the fugacity with chemical potentials equal to $\mu = -k_B T/2$, 0, and $k_B T/2$, respectively. To compare the three cases, the thermal density is scaled by λ_{th}^3 and the position vector by the Gaussian thermal width, $\sigma = \sqrt{2k_B T/m\omega^2}$.

an inverted-parabola shaped void. Despite the repulsive interaction with the condensed atoms, the peak density of the thermal atoms remains well approximated by n_{th} evaluated at $\mathbf{r} = 0$, or $n_{th,0} = \zeta(3/2)/\lambda_{th}^3$; however, the position of the peak density is displaced by the condensate.

The presence of interactions and thermal excitations results in a depletion of the central density of the cloud. Subsequently, the critical density required for the cloud to begin to condense is achieved at a lower temperature. This reduction of the critical temperature is determined by expanding ϵ as $\epsilon - \epsilon_0$ in Equation (2.5), where $\epsilon_0 = 3\hbar\omega_m/2 + 2n_c g$ and $\omega_m = (\omega_x + \omega_y + \omega_z)/3$ is the arithmetic mean trap frequency. The leading first order corrections to T_c include terms for $\partial N/\partial T$, $\partial N/\partial\mu$, and $\partial n_c/\partial\mu$, yield the finite-temperature interacting gas expression for the critical temperature,

$$T_c = T_{c,0}\left[1 - 0.73\frac{\omega_m}{\bar{\omega}}\frac{1}{\sqrt[3]{N}} - 1.33\frac{a_s}{\bar{a}}\sqrt[6]{N}\right], \tag{2.29}$$

where $T_{c,0}$ is the non-interacting gas critical temperature from Equation (2.8). The first corrective term depends on the ratio of arithmetic and geometric mean trap frequencies and indicates that the reduction in the critical temperature is dependent on the anisotropy of the potential, with $\omega_m/\bar{\omega} = (2 + \lambda_T)/3\sqrt{\lambda_T}$ and $\lambda_T = \omega_\parallel/\omega_\perp$ [43]. Therefore, the first term is minimized by a homogeneous trap with large atom number. The second correction accounts for the strength of the repulsive interactions on the thermal atoms, which scale as $\sqrt[6]{N}a_s/\bar{a}$.

Next, the finite temperature corrections for the condensate fraction can be addressed. Expanding Equation (2.5) to first order in the chemical potential, one finds that, in response to the reduction of the critical temperature, N_{th} at finite-temperature is larger than the zero-temperature value. The corrected expression for N_{th} is

$$\begin{aligned} N_{th}(T,\mu) &\approx N_{th,0} + \mu\frac{\partial N_{th}}{\partial\mu}, \\ &= N\tilde{T}^3\left[1 + \frac{\zeta(2)}{\zeta(3)}\frac{\mu}{k_B T}\right], \end{aligned} \tag{2.30}$$

which shows that at a given temperature the number of thermal particles increases according

to the ratio of interaction and thermal energies. As before, the condensate fraction for an interacting, finite-temperature Bose gas is given by $N_c/N = (N - N_{th})/N$.

Finally, corrections to the energy and specific heat of the cloud can be addressed. The contribution to the total energy by the condensate in the TF approximation is given by $E_c = 5\mu(T)N_c(T)/7$ and includes the temperature dependence shown in Equation (2.30). The energy of the thermal cloud is again calculated from Equation (2.10), but now the effects due to interactions are considered by determining $\partial E/\partial\mu$ and including terms to first order in μ/k_BT. Therefore, the total energy of the cloud is given by

$$E = Nk_BT_c\left[3\frac{\zeta(4)}{\zeta(3)}\tilde{T}^4 + \frac{5+16\tilde{T}^3}{7}\frac{\mu(T)}{k_BT_c}\right]. \tag{2.31}$$

As before, the specific heat can then determined via the relation, $C = \partial E/\partial T$. Equations for N_{th}, E, and C can be made to depend solely upon N, T, and T_c by inserting the non-interacting gas expression for the condensed atom number $N_c = N(1-\tilde{T})$. The equations are as follows:

$$\begin{aligned}
N_{th} \approx & \left[\tilde{T}^3 + 2.15\left(\frac{N^{1/6}a_s}{\bar{a}}\right)^{2/5}\tilde{T}^2(1-\tilde{T}^3)^{2/5}\right]N, \\
E = & \left[2.7\tilde{T}^4 + 1.12\left(\frac{N^{1/6}a_s}{\bar{a}}\right)^{2/5}(1+3.2\tilde{T}^3)(1-\tilde{T}^3)^{2/5}\right]Nk_BT_c, \\
C = & \left[10.8\tilde{T}^3 + 10.752\left(\frac{N^{1/6}a_s}{\bar{a}}\right)^{2/5}\tilde{T}^2(1-\tilde{T}^3)^{2/5}\right. \\
& \left. - 1.344\left(\frac{N^{1/6}a_s}{\bar{a}}\right)^{2/5}\tilde{T}^2(1+3.2\tilde{T}^3)/(1-\tilde{T}^3)^{3/5}\right]Nk_B.
\end{aligned} \tag{2.32}$$

The set of Equations (2.32) is used extensively in the numerical calculations of the atomtronic battery and transistor described in chapter 5.

2.2 Theoretical study of a triple-well atomtronic transistor

We now look to apply the characteristics of interacting Bose gases at finite temperature to the field of atomtronics. In this section, concepts from analog electronics are drawn upon

to theoretically study the behavior of a trapped, ultracold atomic system in the context of a three terminal atomtronic device, namely a transistor.[2] A semiclassical analysis is presented that studies the flow of ultracold atoms having finite temperature, T, and chemical potential, μ, through a triple-well potential designed to mimic the behavior of an electronic transistor.

The theoretical triple-well system that we consider is sectioned by two repulsive potential barriers, each of which is analogous to the built-in potential in the space charge region of a semiconductor junction or the work function of the cathode in a vacuum tube [49, 50, 51]. Much like the thermionic emission of electrons across the energy barriers in these electronics examples, atom currents in our system flow due to those atoms that are energetic enough to traverse the repulsive barrier. Thus, atom currents can be described using a formalism common to evaporative cooling. Building upon the work of References [52] and [53], relations for atomic currents driven by thermal and chemical potentials are defined in Section 2.2.2. Similar non-equilibrium dynamics have been studied in double-well systems containing cold and ultracold atoms. These works exemplify the role of gradients in temperature and chemical potential in driving the system towards thermal equilibrium [54, 55, 56, 57, 58, 59]. By considering one of the three wells open to the surrounding environment, we introduce atom loss that prohibits the system from equilibrating. The resulting quasi-steady-state chemical potentials and temperatures of the wells are determined in Section 2.2.3 and analyzed in the context of an electronic circuit with potential biases between nodes.

Transistor-like functionality of the device is established in Sections 2.2.4 and 2.2.5, where current gain and maximum power output are calculated given an externally applied input current to the gate well. Here, transistor action arises due to the interplay between the input current and the steady-state thermodynamic properties of the gate. Depending on the Q-point, the current into the drain is either attenuated or amplified in response to the applied gate current, demonstrating a current gain greater than unity. Additionally, the transresistance is found to be negative indicating the active nature of the transistor in that

[2] The contents of this section are published in Reference [48].

it draws power from a reservoir to control power output to a load. The maximum power to an impedance matched load is then shown for a range of Q-points.

2.2.1 The theoretical system

Our semiclassical treatment of an atomtronic transistor begins by borrowing the nomenclature of the semiconductor field-effect transistor. The three regions of the triple-well potential, shown in Figure 2.2(a), are labeled the "Source," "Gate," and "Drain" wells. In labeling the regions of the triple-well potential, field-effect transistor nomenclature is used as it describes the role of each well in an atomtronic transistor: Atoms flow from the source, through a gate region, and into a drain well where they are removed from the system. This naming scheme is meant to convey an intuition for the role of each region, rather than imply the behavior of the triple-well system is more analogous to the behavior of a field-effect transistor than a bipolar junction transistor. Emulating the experimental system described in chapter 5 we take the trapping potential to be cigar shaped with corresponding harmonic trap frequencies $\omega_{\parallel} \ll \omega_{\perp}$. This potential is sectioned in the longitudinal direction by two repulsive Gaussian barriers having peak heights V_{GS} and V_{GD}, respectively, to form the source, gate, and drain wells. The longitudinal profile and separation of the barriers determines the longitudinal gate well trap frequency. Furthermore, the longitudinal trap axis of the source well is assumed to be half harmonic for simplicity. The degree of overlap of the two barriers contributes to a potential bias in the gate, $V_{\mathrm{G},0}$, with respect to the source and drain. Finally, the drain well is modeled as a reflectionless output port that would feed into a subsequent circuit element.

2.2.2 Current flow mechanism

Previous works have modeled the flow of atoms across a potential barrier in order to study both the selective removal of atoms involved in evaporative cooling as well as the reverse process in trap loading [52, 53, 60]. Here, the expressions in Ref. [60] are modified

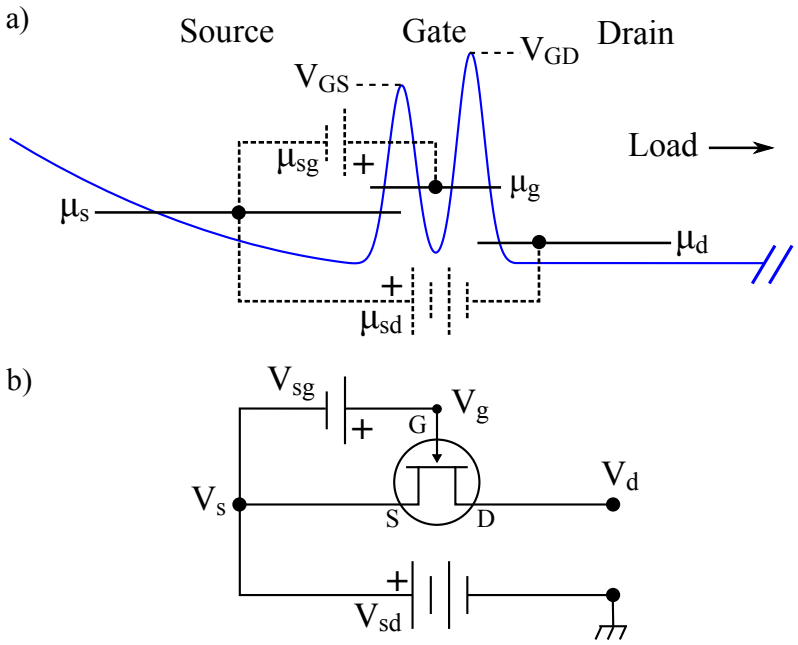

Figure 2.2: (a) Triple-well potential with source, gate, and drain wells. Chemical potential levels in each well are depicted in the context of potential biases. The current output into the drain can then be coupled to the desired 'load.' In the model presented here, the flow of atoms through the potential is controlled by adjusting the source-gate chemical potential difference via an external current input to the gate. (b) A simplified schematic of an electronic common-source amplifier circuit with analogous functionality to its atom based counterpart.

to include the chemical potential due to the presence of a BEC in the source and gate wells. Under the HF theory, the mean field of the condensate shifts the energies of the thermal atom distribution up by μ and is conceptually analogous to an applied bias voltage in an electronic circuit. In the absence of a BEC, the chemical potential can be calculated according to self-consistent mean field methods [61]. However, in this model the minimum single particle energy is $V_{i,0}$ and thus negative μ_i are set to zero. Therefore, the atom currents in the triple-well system are defined by the set of equations:

$$\begin{aligned} I_{\mathrm{sg}} &= \gamma_{\mathrm{s}} N_{\mathrm{th,s}} \exp[-(V_{\mathrm{GS}} - \mu_{\mathrm{s}})/k_B T_{\mathrm{s}}], \\ I_{\mathrm{gs}} &= \gamma_{\mathrm{g}} N_{\mathrm{th,g}} \exp[-(V_{\mathrm{GS}} - V_{\mathrm{G,0}} - \mu_{\mathrm{g}})/k_B T_{\mathrm{g}}], \\ I_{\mathrm{gd}} &= \gamma_{\mathrm{g}} N_{\mathrm{th,g}} \exp[-(V_{\mathrm{GD}} - V_{\mathrm{G,0}} - \mu_{\mathrm{g}})/k_B T_{\mathrm{g}}], \end{aligned} \tag{2.33}$$

where the product $\gamma_i N_{\mathrm{th},i}$ is the effective collision rate of thermally excited atoms in the i-th well, and the exponential factor reflects the thermodynamic probability that an atom possesses sufficient energy to traverse the barrier. Note that the subscript order indicates the direction of current flow, e.g. I_{sg} describes the atom flux from the source to the gate well, and capitalized subscripts indicate model parameters. Building upon the collision process described in Section 2.1.2, the equilibrium collision rate ($\gamma = \sqrt{2/\pi} n_{th} \sigma_0 \Delta \mathrm{v}$) then depends only on the peak density of the thermal component, $n_{th} = \zeta(3/2)/\lambda_{th}^3$, the s-wave collision cross-section σ_s, and the mean thermal velocity, Δv [43]. Thus, the collision rate for the i-th well is given by

$$\gamma_i = 32\pi^2 \zeta(3/2) m (a_s k_B T_i)^2 / h^3, \tag{2.34}$$

and the expression for $N_{th,i}$ is given by Equation (2.30).

As alluded to previously, the currents in Equation (2.33) are reminiscent of the current in thermionic devices, $J = AT^2 \exp[-(V_0 - V_b)/k_B T]$, where A is the Richardson constant, which depends on the density of states and other material properties [49]. Devices that derive their functionality from thermionic emission convert thermal energy into electric current between a heated filament and an adjacent, charged electrode [62]. The magnitude of the

bias voltage, V_b, applied to the electrode, relative to the built-in potential, V_0, then tunes the current flow. In both electronic and atomtronic systems, Bose-Einstein and Fermi-Dirac statistics are approximated by the Maxwell-Boltzmann distribution, given that the truncation parameter $\eta \equiv V/T$ is sufficiently large, i.e., $\eta \gtrsim 3$ [49, 52, 53]. Factors prior to the exponential term in Equations (2.33) as well as the expression for thermionic emission describe the abundance of particles which may contribute to the current.

2.2.3 Source and gate well ensembles in steady-state

Steady-state circuit operation is analyzed by enforcing particle number and energy conservation, expressed using analogues of Kirchhoff's current and voltage laws:

$$I_{\rm sg} = I_{\rm gs} + I_{\rm gd}, \tag{2.35}$$

$$I_{\rm sg}(V_{\rm GS} + \kappa_{\rm GS} k_B T_{\rm s}) = I_{\rm gs}(V_{\rm GS} + \kappa_{\rm GS} k_B T_{\rm g}) + I_{\rm gd}(V_{\rm GD} + \kappa_{\rm GD} k_B T_{\rm g}), \tag{2.36}$$

where the κ's, which indicate the average excess energy of atoms traversing the barriers, are of order unity [60]. It is supposed that some external reservoir supplies atoms to the source well, maintaining a fixed chemical potential, μ_s, and temperature, T_s. For barrier heights that are large compared to the chemical potential and thermal energies, the three wells are weakly coupled by thermal atoms that have sufficient energy to traverse the barriers. Thus, as current flows from source to gate and subsequently from the gate to the drain, we assume that the gate acquires a well-defined chemical potential, $\mu_{\rm g}$, and temperature, $T_{\rm g}$, once a steady-state is reached. Additionally, we impose that current into the drain is removed from the system such that no current flows from the drain back towards the gate. An illustration of the system is shown in Figure 2.3 that elucidates important model parameters.

With the source well ensemble held constant, we seek steady-state values of the gate chemical potential and temperature in terms of $\mu_{\rm s}$ and $T_{\rm s}$. It proves useful to define a tem-

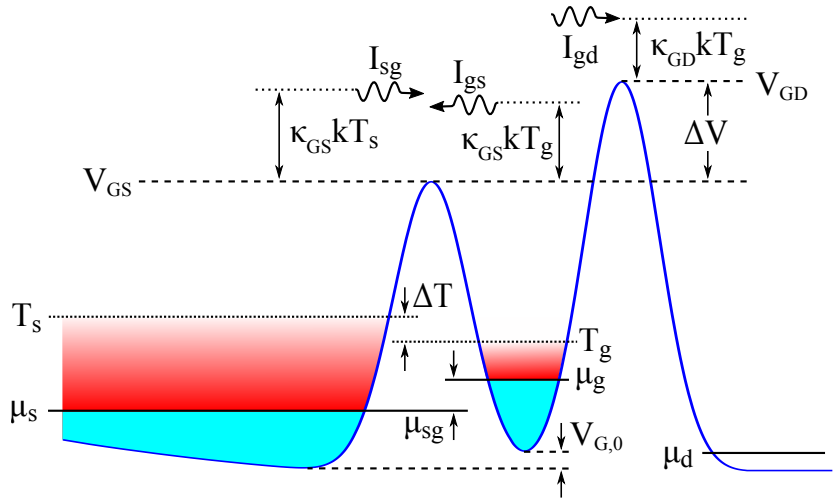

Figure 2.3: Schematic of atom and energy flow across the gate barriers. The atom current carries with it an energy in excess of the barrier height by the factor κkT relative to each barrier. Light blue shading indicates the offset in energy of the thermal component, shown in red, due to the condensate chemical potential. An example steady-state for source and gate ensembles is shown, in which the temperature drop, τ, is positive and the chemical potential drop, μ_{sg}, is negative.

perature drop τ and barrier height difference υ, both normalized to the source temperature:

$$\tau \equiv (T_{\rm s} - T_{\rm g})/T_{\rm s} \equiv \Delta T/T_{\rm s}, \tag{2.37}$$

$$\upsilon \equiv (V_{\rm GD} - V_{\rm GS})/k_B T_{\rm s} \equiv \Delta V/k_B T_{\rm s}. \tag{2.38}$$

Using the currents defined in Equation (2.33), along with Equations (2.35) and (2.36), it is possible to derive relations for both the temperature drop,

$$\tau = e^{-\upsilon/(1-\tau)} \frac{\upsilon + (\kappa_{\rm GD} - \kappa_{\rm GS})}{\kappa_{\rm GS} + \kappa_{\rm GD} e^{-\upsilon/(1-\tau)}}, \tag{2.39}$$

and the normalized chemical potential drop,

$$\begin{aligned} \hat{\mu}_{\rm sg} &= (1-\tau)\ln\left[(1-\tau)^4\left(1+e^{-\frac{\upsilon}{1-\tau}}\right)\right] - \tau\left(\hat{V}_{\rm GS} - \hat{\mu}_{\rm s}\right) \\ &+ (1-\tau)\ln\left[\frac{1-\tau+\frac{\zeta(2)}{\zeta(3)}\left(\hat{\mu}_{\rm s} - \hat{V}_{\rm G,0} - \hat{\mu}_{\rm sg}\right)}{1+\frac{\zeta(2)}{\zeta(3)}\hat{\mu}_{\rm s}}\right], \end{aligned} \tag{2.40}$$

where $\mu_{\rm sg} \equiv \mu_{\rm s} - \mu_{\rm g}$ and the hat ($\hat{}$) indicates quantities normalized to the source temperature. Within these equations, $e^{-\upsilon/(1-\tau)}$ represents the ratio of forward current into the drain relative to current fed back into the source, $I_{\rm gd}/I_{\rm gs}$. Given its effect on the balance of currents into and out of the gate well, the value υ is referred to as the feedback parameter. The impact of the feedback parameter on the gate-drain, normalized to the source-gate current, can be seen in Figure 2.4. The ratio of currents is independent of η, but the absolute magnitude of the $I_{\rm gd}$ depends strongly on μ_s, T_s, and η due to the exponential nature of the currents in Equations (2.33). In deriving Equation (2.40) we have used the fact that the thermal and chemical potential drops are zero at $\upsilon = \infty$ along with the relations introduced in Section 2.1.3 to determine the ratio of $\gamma_{\rm g} N_{\rm th,g}/\gamma_{\rm s} N_{\rm th,s}$ that satisfies Equation (2.35). Complete derivations of Equations (2.39) and (2.40) are provided in Appendix A. In the absence of an external gate input, Equation (2.40) shows that the source-gate junction is self-biased to some Q-point characterized by $\mu_{\rm sg}$. The magnitude of this bias is primarily dependent on the feedback parameter, both directly and through the temperature drop. This self-bias

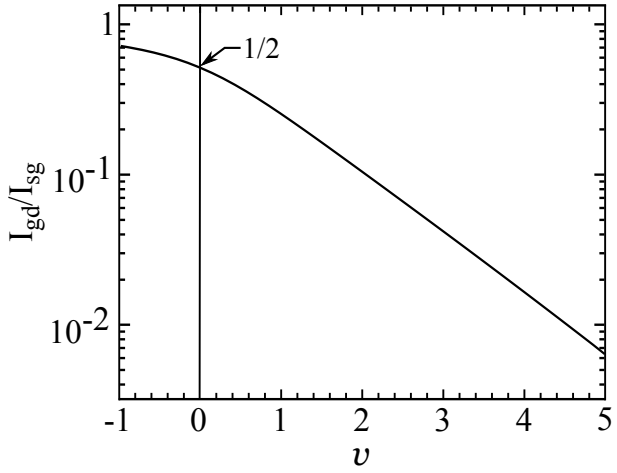

Figure 2.4: Log plot of the net drain current relative to the source-gate current, which reflects the role of the feedback parameter.

is illustrated in Figure 2.2(a) within the atomic system and Figure 2.2(b) for an equivalent, simplified electronic circuit. Equations (2.39) and (2.40) form the basis of our model and can be solved self-consistently in order to characterize the thermodynamic variables of the triple-well system in steady-state.

To calculate the values of τ and $\hat{\mu}_{\rm sg}$, the κ parameters of the trapping potential must be determined. Trap geometry has a strong effect on the average energy removed by an atom leaving via a controlled trajectory. For atoms escaping isotropically from a potential well, as in typical evaporative cooling schemes, $\kappa \simeq 1$ [52, 53]. However, limiting the escape trajectory to purely 1D, for instance along the loose axis of a cigar-shaped trap, $\kappa \simeq 2.9$ for truncation parameters $\eta \equiv V/k_BT = 4 - 7$ [60]. The difference in κ factors is a direct result of allowed escape trajectories. The direct simulation Monte-Carlo (DSMC) method is used to confirm $\kappa \simeq 2.9$ for the geometry and feedback parameters modeled here. More information regarding these simulations are given in Section 5.4.1.

The temperature and chemical potential drops are shown as functions of the feedback parameter in Figure 2.5, with $\kappa_{\rm GS} = \kappa_{\rm GD} = 2.9$. The behavior shown by the temperature drop is somewhat non-intuitive in that for values of positive feedback ($V_{\rm GD} > V_{\rm GS}$), the

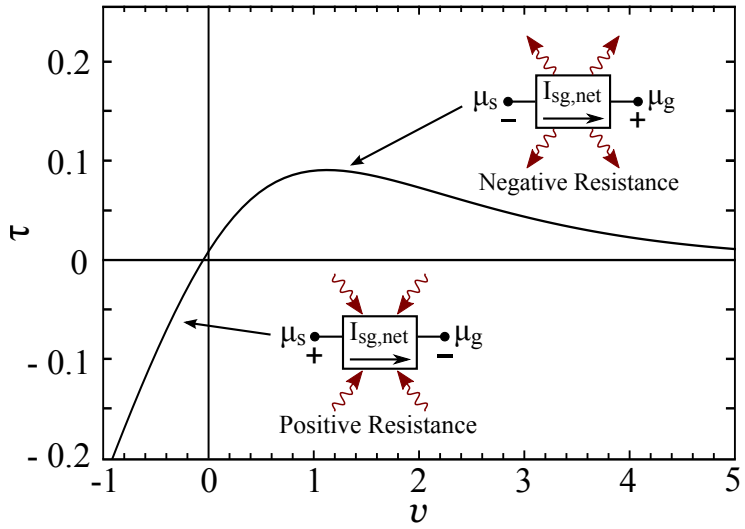

Figure 2.5: Plot of the temperature drop vs. feedback parameter. Insets illustrate power dissipation due to the static source-gate resistance. Negative υ results in a negative temperature drop in the direction of net current across the source-gate barrier, indicating heat transfer into the gate and $T_{\rm g} > T_{\rm s}$ in steady-state. Conversely, positive υ results in net cooling (negative power dissipated) and τ increases until $\mu_{\rm sg}$ peaks. As $\upsilon \to \infty$, $I_{\rm gd} \to 0$ and equilibrium between the gate and source wells is reached.

temperature of the gate is actually *lower* than the source, despite current from the source into the gate having an average energy $V_{\rm GS} + \kappa_{\rm GS} k_B T_{\rm s}$. Furthermore, Figure 2.6 shows that there will generally exist a range of feedback parameters for which the chemical potential drop is negative, meaning the source-gate junction is reverse-biased. Also shown in Figure 2.6 are two threshold feedback parameters. The first, $\upsilon_{\rm BEC}$, indicates the formation of a BEC in the gate well. For $\upsilon \geq \upsilon_{\rm BEC}$ the balance of particle and energy currents leads to a steady-state gate well ensemble with sufficiently high phase-space density to condense. The second threshold, $\upsilon_{\rm TC}$, indicates the feedback parameter above which negative transconductance occurs for the steady-state parameters. Section 2.2.5 provides an in-depth discussion of the $\upsilon_{\rm TC}$ threshold.

To better understand the steady-state results, one can consider the power dissipated within the gate well of the transistor, $P_{\rm sg} = I_{\rm sg,net}^2 R_{\rm sg}$. Here $I_{\rm sg,net} = I_{\rm sg} - I_{\rm gs} > 0$ is the total atom current flowing into the gate. Note that the power dissipated within the gate well does not include the gate to drain current, as power output to the drain is available to do work on a connected load. The static source-gate resistance in steady-state is

$$R_{\rm sg} \equiv \mu_{\rm sg}/I_{\rm sg,net}. \tag{2.41}$$

Given the sign of the chemical potential drop, $R_{\rm sg}$ can be negative indicating an ohmic cooling synonymous with the evaporative cooling process, which leads to positive τ. Negative power dissipation within the gate well peaks at $\upsilon \approx 1$, which is consistent with the maximum value of τ.

2.2.4 Current gain

Within the steady-state model presented, current gain is the most readily studied quantity since voltage and power gain require more explicit knowledge of the connected 'load.' To study gain, we use a method similar to determining the two-port admittance parameters of an electronic circuit, which is commonly used to describe transistor action in

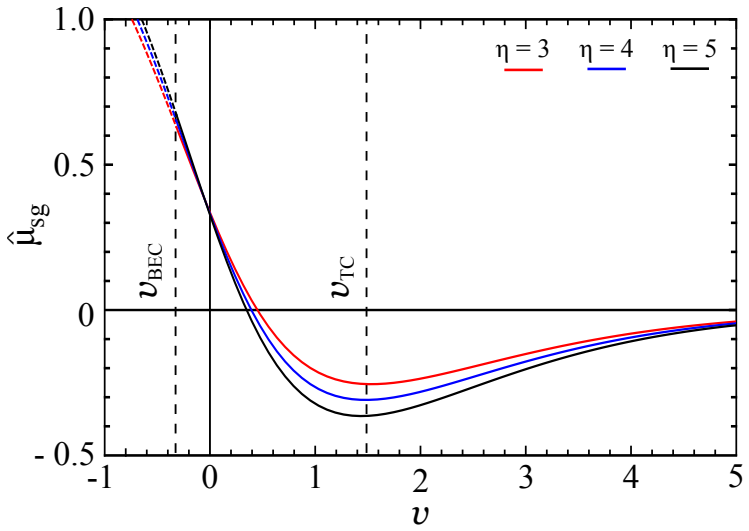

Figure 2.6: Chemical potential drop between the source and gate wells, normalized to the source temperature, versus the feedback parameter. Red, blue, and black curves show the steady-state value of $\hat{\mu}_{sg}$ for truncation parameters of 3, 4, and 5, respectively. Two vertical dashed lines indicate threshold behavior linked to the feedback parameter. The first, υ_{BEC}, above which a BEC is predicted to form in the gate well and a second, υ_{TC}, where the transconductance becomes negative.

electronic transistors [7]. The coupled system of equations for the triple-well atomic system is given by

$$\begin{pmatrix} \mathrm{d}I_{\mathrm{N,g}} \\ \mathrm{d}I_{\mathrm{Q,g}} \end{pmatrix} = \begin{pmatrix} a_{11} & a_{12} \\ a_{21} & a_{22} \end{pmatrix} \begin{pmatrix} \mathrm{d}\mu_{\mathrm{g}} \\ \mathrm{d}T_{\mathrm{g}} \end{pmatrix}, \tag{2.42}$$

where $I_{\mathrm{N,g}}$ and $I_{\mathrm{Q,g}}$ are the particle and heat currents into the gate well. The 'a' parameters relate the currents to either a change in chemical potential or temperature assuming the other is constant, e.g. $a_{11} = (\partial I_{\mathrm{N,g}}/\partial\mu_{\mathrm{g}})_{\mathrm{d}T_{\mathrm{g}}=0}$. Equation (2.42) is akin to the Onsager relations [29, 63] for particle and heat diffusion that have been utilized to describe non-equilibrium transport dynamics in atomic systems [56, 57]. Here, they are used to describe the particle and heat currents applied to the gate well in order to elicit the changes $\mu_{\mathrm{g}} \to \mu_{\mathrm{g}} + \mathrm{d}\mu_{\mathrm{g}}$ and $T_{\mathrm{g}} \to T_{\mathrm{g}} + \mathrm{d}T_{\mathrm{g}}$. The particle and heat currents on the left-hand side of Equation (2.42) are given by the differential of the sum of terms in Equations (2.35) and (2.36), respectively, with current flow into (out of) the gate taken to be positive (negative). In steady-state, $\mathrm{d}I_{\mathrm{Q,g}} = 0$; thus, the temperature response to a change in chemical potential is given by $\partial T_{\mathrm{g}}/\partial\mu_{\mathrm{g}} = -a_{21}/a_{22}$. It is not surprising that this quantity is negative, as the chemical potential varies inversely with temperature at constant atom number, as seen from Equations (2.9) and (2.26). For small deviations from the steady-state, this relation is used in conjunction with Equation (2.42) to determine the input current required to change the gate chemical potential by some $\mathrm{d}\mu_{\mathrm{g}}$:

$$\mathrm{d}I_{\mathrm{g}} = \mathrm{d}\mu_{\mathrm{g}} \left(a_{11} - a_{12}\frac{a_{21}}{a_{22}} \right), \tag{2.43}$$

where the quantity in the parentheses is equivalent to the gate well input admittance. The differential current gain about the Q-point is then defined as the ratio of the resulting change in gate-drain current and the external gate well input current:

$$A_{\mathrm{I}} \equiv \frac{\mathrm{d}I_{\mathrm{gd}}}{\mathrm{d}I_{\mathrm{g}}}, \tag{2.44}$$

where $\mathrm{d}I_{\mathrm{gd}} = I'_{\mathrm{gd}} - I_{\mathrm{gd}}$ and the primed current is evaluated at $\mu'_{\mathrm{g}} = \mu_{\mathrm{g}} + \mathrm{d}\mu_{\mathrm{g}}$ and $T'_{\mathrm{g}} = T_{\mathrm{g}} + (\partial T_{\mathrm{g}}/\partial\mu_{\mathrm{g}})\mathrm{d}\mu_{\mathrm{g}}$.

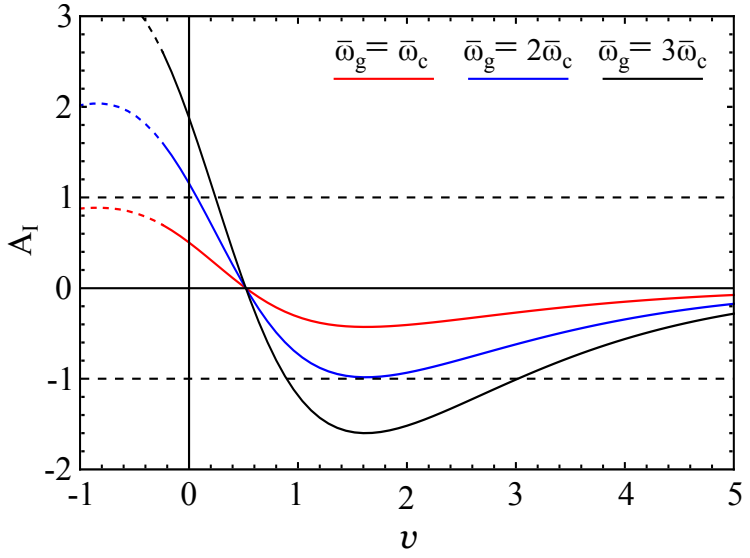

Figure 2.7: Plot of the differential current gain at the drain terminal of the atomtronic transistor. Three curves are shown that illustrate the increase in current gain magnitude with increasing mean trap frequency of the gate well. Horizontal dashed lines indicate unity gain.

Figure 2.7 shows the current gain for the range of feedback parameters shown in Figure 2.5, illustrating the current gain at various Q-points. Two complementary operating regimes arise in which the transistor provides either positive or negative differential current gain. For feedback parameters near zero, $A_{\rm I}$ is positive, indicating that a positive (negative) $\mathrm{d}I_{\rm g}$ leads to an increase (decrease) in $I_{\rm gd}$. For increasingly negative feedback parameters, i.e., $\upsilon < \upsilon_{\rm BEC}$, the current gain becomes nonphysical as $\mathrm{d}\mu_{\rm g}$ becomes ill-defined in the absence of a condensate in the gate well. At $\upsilon \sim 0.5$, the sign of $A_{\rm I}$ flips where the changes in $I_{\rm gd}$ due to $\mathrm{d}\mu_{\rm g}$ and $\mathrm{d}T_{\rm g}$ become equal. Finally, at $\upsilon \sim 1.6$, the gain reaches a maximum, negative amplitude.

Positive and negative differential current gain regimes arise due to the interplay between $\mu_{\rm g}$ and $T_{\rm g}$. To better understand each regime, consider the scaling of the chemical potential with respect to the number of condensed atoms in the Thomas-Fermi limit, $\mu \propto N_{\rm c}^{2/5}$. In the negative differential current gain regime, steady-state $\mu_{\rm g}$ is larger than in the positive gain regime. Therefore, a larger number of atoms at $T < T_{\rm g}$ must be injected into the gate

well to elicit a positive $\mathrm{d}\mu_{\mathrm{g}}$. The resulting decrease in T_{g} causes a reduction of I_{gd} that is more substantial than the increase of I_{gd} due to the additional chemical potential. Thus, $\mathrm{d}\mu_{\mathrm{g}}$ is positive, but the net change in the gate-drain current is negative. The opposite effect is responsible for positive differential current gain.

With the sign of the current gain understood, the magnitude of the output current is determined. Multiple traces are shown in Figure 2.7 that indicate the gain for different gate well geometric trap frequencies, $\bar{\omega}_{\mathrm{g}}$, relative to the trap frequencies of the external well that injects the control current, $\bar{\omega}_{\mathrm{c}}$, where $\bar{\omega} = (\omega_{\parallel}\omega_{\perp}^2)^{1/3}$. The enhancement in the magnitude of the current gain arises due to the scaling of the specific heat, $C \propto 1/\bar{\omega}^3$, and chemical potential, $\mu \propto \bar{\omega}$, of a tight well [43]. More specifically, as $\bar{\omega}$ increases, the scaling in μ and C reduce the number of atoms needed to alter the chemical potential and temperature of the steady-state gate well population. In the case that the trap frequencies are equal, one recovers the expected result that $A_{\mathrm{I}} = 1/2$ at $\upsilon = 0$, as there are two equally probable output channels from the gate. This behavior indicates that the ratio of trap frequencies is a key design parameter for achieving greater than unity gain.

2.2.5 Transistor power output and transconductance

Despite a lack of explicit knowledge regarding the load circuit connected to the drain well, it is possible to determine the maximum power delivered to an impedance matched load. Stated generally, impedance matching is the process of selecting the input impedance of the load circuit to be equal to the output impedance of the device such that reflection of the output signal is minimized. The reflection of particles with a given energy impinging upon a potential landscape can be calculated using a number of methods (e.g. [64, 65]) and has been experimentally studied using cold [66] and ultracold atoms [67]. For a matched load, we borrow the electronics definition for the maximum power at the transistor output [6],

$$P_{\mathrm{max}} = \frac{g_{\mathrm{m}}\mathrm{d}\mu_{\mathrm{g}}^2}{4}, \tag{2.45}$$

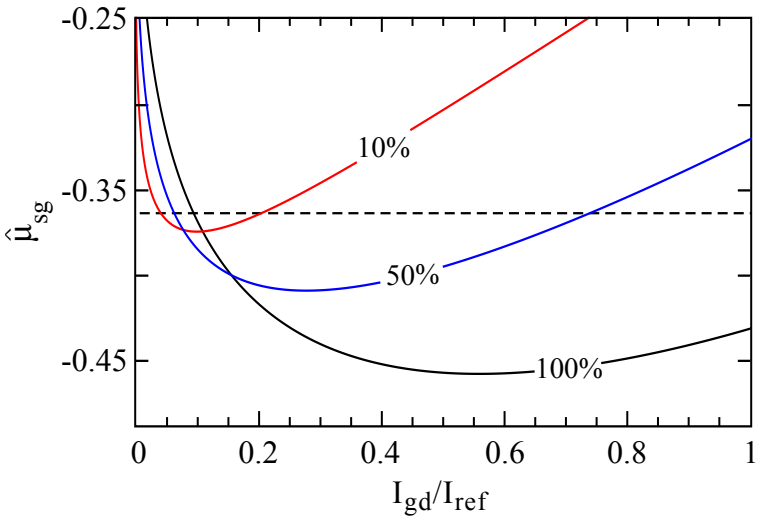

Figure 2.8: Plot of the transconductance of the atomtronic transistor for $\eta = 5$. Three curves are shown for feedback parameters 10%, 50%, and 100% above threshold. The horizontal dashed line indicates the chemical potential drop at threshold.

where $\mathrm{d}\mu_\mathrm{g}$ is the amplitude of the gate chemical potential modulation and g_m is the transconductance, given by

$$g_\mathrm{m} \equiv \frac{\mathrm{d}I_\mathrm{gd}}{\mathrm{d}\mu_\mathrm{sg}} = \left(\frac{\partial T_\mathrm{s}}{\partial \mu_\mathrm{sg}}\right)\left(\frac{\partial I_\mathrm{gd}}{\partial T_\mathrm{s}}\right), \tag{2.46}$$

where the partial derivatives are evaluated at constant μ_s. Transconductance is useful in describing operation of the devices as an active element, i.e., one that supplies power. From Equation (2.45), it can be seen that if g_m is negative, the power dissipated at the transistor output is negative. Effectively, the transistor converts power supplied by the source well into power output from the drain controlled by $\mathrm{d}\mu_\mathrm{g}$. As alluded to in Figure 2.6, there is a threshold feedback parameter, υ_TC, above which the system exhibits negative transconductance in steady-state. This threshold is determined from the inflection point of g_m. Both the sign and magnitude of g_m are determined from the derivative of the transfer characteristic curves. Examples of these curves are shown in Figure 2.8 for $\upsilon = 10\%$, 50%, and 100% above υ_TC.

The maximum power dissipated at the output of the transistor is shown in Figure 2.9 as a function of the fraction above threshold, $(\upsilon - \upsilon_\mathrm{TC})/\upsilon_\mathrm{TC}$. The values of P_max are calculated

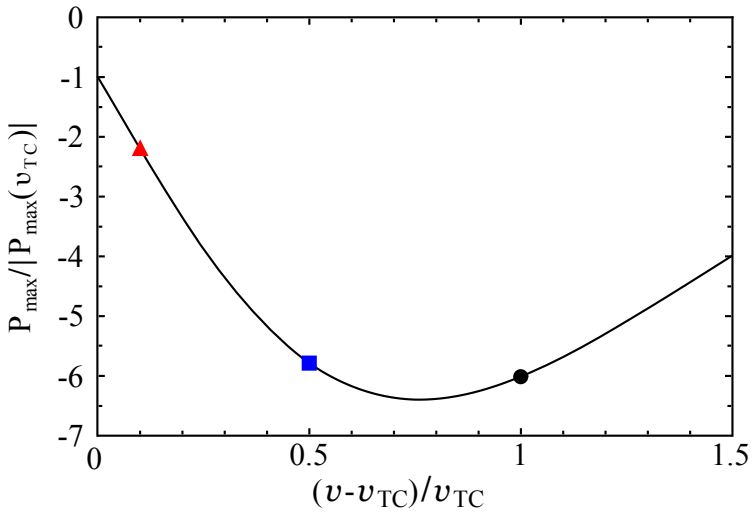

Figure 2.9: Maximum power dissipated when connected to an impedance matched load, normalized to the magnitude of the threshold value, $|P_{\max}(\upsilon_{\mathrm{TC}})|$, as a function of the feedback parameter. Above threshold, the transistor exhibits negative transconductance. The triangle, square, and circle represent the peak power for feedback parameters that are 10%, 50%, and 100% above the threshold value υ_{TC}, respectively. Negative dissipated power is synonymous with power supplied to the load circuit.

using the same fractional value of $\mathrm{d}\mu_\mathrm{g}$ with respect to the steady-state μ_g for all υ. The power output corresponding to the three transfer characteristic curves in Figure 2.8 are included in Figure 2.9.

The absolute magnitude of the power depends on the value of $\mathrm{d}\mu_\mathrm{g}$; therefore, to better illustrate the behavior of P_max it is scaled by $P_\mathrm{max}(\upsilon = \upsilon_\mathrm{TC})$ in Figure 2.9. The magnitude of the maximum power dissipated is seen to peak at $\upsilon \approx 1.75 \times \upsilon_\mathrm{TC} \approx 2.6$. As was the case for the current gain, the power delivered by the transistor is ultimately limited by the gate-drain current, which decreases exponentially with increasing υ. However, the power is delivered in the form of higher energy thermal atoms. As a result, the maximum power dissipation peaks at a higher value than the current gain.

Negative power dissipation, a familiar concept introduced early in the literature on electronic oscillators, originates due to the negative transconductance or transresistance of a device [36]. When coupled to a circuit containing frequency dependent elements, an active device that exhibits negative transresistance cancels the resistive power loss in the load, resulting in the buildup of a resonant, oscillatory signal [35, 36]. The oscillator concept is attractive in the field of atomtronics, given the historical impact of RF and higher frequency signal generation within the field of analog electronics.

2.2.6 Connection to electronic transistor functionality

Within the semiclassical approach presented in this section, atom currents driven by chemical potentials and thermal energy are used to describe the particle and energy transport throughout the system. By varying the height of the barriers that separate the three wells, it is shown that the steady-state chemical potential and temperature differences between the source and gate wells can be controlled. This process is analogous to biasing an electronic transistor to the desired quiescent point. Returning to the analogy with electronics, transistor functionality largely depends on the bias or quiescent operating point set by the voltages at each of its three terminals. This steady-state theory indicates that regimes of positive

and negative potential drops between the source and gate wells exist, which are analogous to forward and reverse-bias modes in electronic transistors, respectively.

Transistor-like behavior of the triple-well atomic system was investigated by calculating the current gain given an external current input to the gate well. The device exhibits regions of both negative and positive differential current gain, depending on the feedback parameter, that can exceed unity. The magnitude of the gain was shown to depend on the mean trap frequency of the gate well, a characteristic that arises due to the nonlinear dependence of the chemical potential and specific heat of the gas on the trap frequency. Therefore, the current gain is a widely tunable parameter, controlled by both υ and $\bar{\omega}_{\mathrm{g}}$.

In addition to transistor-like gain, the maximum power delivered to an impedance matched load was calculated. For feedback parameters above the threshold value, υ_{TC}, the transistor exhibits negative power dissipation at its output. In other words, the triple-well potential supplies power to the load circuit. As in analog electronics, active devices, i.e., those which exhibit negative transresistance behavior, can be coupled with frequency dependent loads to create an oscillatory output signal. Therefore, if coupled to the appropriate load, the transistor-like triple-well system described here could be used to generate oscillating atomic currents.

Chapter 3

Atom chip development

Applications for atom chips in AMO experiments are numerous, including rapid production of BEC [68, 69, 70, 71] as well as much of the work within the field of atom optics [72, 73, 74, 75, 76, 77]. In order to realize the atomtronic battery and transistor, pictured in Figure 1.3, one must first synthesize the multi-well trapping potential. This chapter begins with a brief theoretical discussion of magnetic trapping, followed by an overview of the various atom chip wire patterns that are utilized in the atomtronics experiment. Finally, other important issues such as heating of the atomic ensemble due to technical noise, and resistive heating in the atom chip wires due to current flow are analyzed.

3.1 Magnetic trapping of neutral atoms

Despite the charge neutral nature of ^{87}Rb atoms, they possess a finite magnetic dipole moment, μ_{mag}, generated by their total atomic angular momentum. As a result, in the presence of a magnetic field, $\mathbf{B}$, the atoms experience an interaction energy,

$$\mathbf{U}_{mag} = -\mu_{mag} \cdot \mathbf{B}. \tag{3.1}$$

If the magnetic field is inhomogeneous, the atom will experience a spatially dependent force,

$$\mathbf{F}_{mag} = -\nabla \mathbf{U}_{mag} = \nabla \left(\mu_{mag} \cdot \mathbf{B} \right). \tag{3.2}$$

Due to the behavior of magnetic fields in regions free of charges and currents, it is only practical to consider fields that force atoms towards a field minimum. More explicitly, local

maxima of a quasi-static magnetic field occur only at the source of the field, e.g. a current carrying wire, (see Reference [78] for a rigorous proof). While it is possible to confine atoms to a Kepler-like orbiting trajectory around a current carrying wire, as was shown in Reference [73], the resulting trap is not localized and is impractical for many atom trapping applications, including atomtronics. Therefore, neutral atoms are typically trapped in a weak-field-seeking atomic state, i.e., $\mu_{mag} > 0$, and the magnetic trap is designed about a minima of the magnetic field.

In the context of magnetic trapping the state of ^{87}Rb atoms is defined by the hyperfine structure quantum number F, the sum of the nuclear spin angular momentum, I, and total electron angular momentum, J. The $5S_{1/2}$ ground state of ^{87}Rb has $I = 3/2$ and $J = 1/2$, which result in either $F = 1$ or 2. In the $F = 1$ ground state manifold, Zeeman split sub-levels range from $m_F = -1, 0, 1$ with Landé g-factor $g_F = -1/2$. Similarly, the $F = 2$ ground state manifold has sub-levels $m_F = -2,\ -1,\ 0,\ 1,\ 2$ and $g_F = 1/2$. Therefore, the magnetic dipole moment of these atoms is given by $\mu = m_F g_F \mu_B$, where μ_B is the Bohr magneton. In order to maximize the magnetic trapping force experienced by the atoms, they should be prepared in the $F = 2$ ground state manifold, in the $m_F = 2$ Zeeman sub-level, which has twice the dipole moment of other trappable states.

3.2 Designing an atom chip for atomtronic devices

This section covers the basics of magnetic trapping on an atom chip along with the chip conductor patterns used for atomtronics experiments. Supplemental derivations of the magnetic fields generated by these chip patterns can be found elsewhere [10, 11, 12, 72, 76, 79]. Special considerations for high-resolution, through-chip, *in situ* imaging are described along with two atom chip design iterations used to complete the work in this dissertation are discussed.

3.2.1 Side-guide trap

To begin, consider the most simple configuration used to trap atoms on a chip, the side-guide. While it does not form a complete, three dimensional trapping potential the side guide addresses the basic concepts used in all static chip trap designs. A waveguide potential is formed by the combination of an infinitely long and thin wire carrying a current I_x and a uniform magnetic bias field oriented perpendicular to the flow of current, B_y. The magnetic field generated by the line current is given by

$$B_{wire} = \frac{\mu_0 I_x}{2\pi r}, \tag{3.3}$$

where μ_0 is the vacuum permeability, $r^2 = y^2 + z^2$, and the field circulates according to the right-hand rule. When combined with the external bias field, a minimum in the magnetic field forms a distance d_z away from the wire, where the magnitudes of B_{wire} and B_y are equal. In order to determine the properties of the trap, one must consider the total magnetic field:

$$B_{\hat{y},side} = \frac{\mu_0 I_x}{2\pi}\frac{z}{(y^2+z^2)}, \tag{3.4}$$

$$B_{\hat{z},side} = \frac{\mu_0 I_x}{2\pi}\frac{-y}{(y^2+z^2)} + B_y, \tag{3.5}$$

where field components are decomposed along the $\hat{y}$ and $\hat{z}$ directions. Figure 3.1 illustrates magnitude and direction of the magnetic field around the waveguide and current carrying wire. The distance d_z is determined by solving Equations (3.4) and (3.5) for z where the total field magnitude is zero,

$$d_z = \frac{\mu_0}{2\pi}\frac{I_x}{B_y}. \tag{3.6}$$

At the position $y = 0, z = d_z$ the potential is a linear quadrupole field with a gradient determined by

$$B'|_{d_z} = \frac{2\pi}{\mu_0}\frac{B_y^2}{I_x} = \frac{B_y}{d_z}, \tag{3.7}$$

where the relation for d_z from Equation (3.6) has been used. The dotted lines in Figure 3.2(a) and (b) show the magnetic field magnitude along both the $\hat{y}-$ and $\hat{z}-$directions, respectfully.

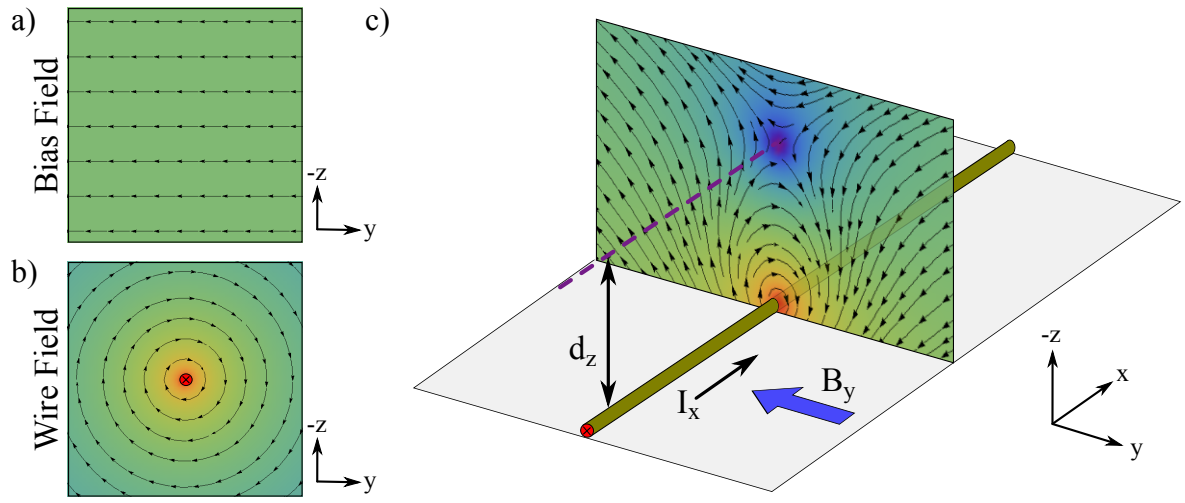

Figure 3.1: Illustration of the magnetic field lines in the side-guide configuration, which is formed by the superposition of a uniform bias field along $-\hat{y}$, shown in (a), and the magnetic field generated by a current carrying wire, shown in (b). c) The resulting waveguide is located a distance d_z below the conductor. Colors indicate the magnetic field strength in the y-z plane, increasing from a local minimum (purple) to the maximum field at the conductor (red).

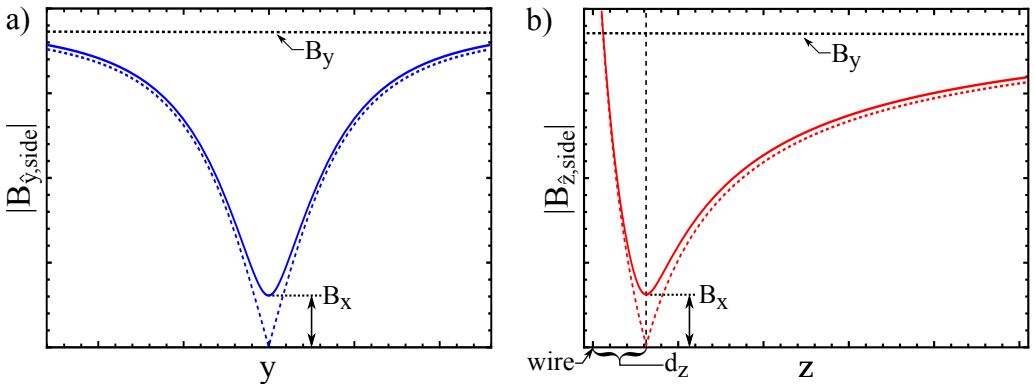

Figure 3.2: Addition of a bias field along the wire current in the side-guide trap converts the field gradient near the minimum from quadrupole (dotted) to harmonic (solid). (a) and (b) show the magnetic field magnitude along the $\hat{y}-$ and $\hat{z}-$directions, respectively.

Equation (3.7) reveals one of the attractive characteristics of atom chips. By enabling atoms to be trapped in close proximity to a current carrying wire (typically tens to hundreds of microns) magnetic traps with large field gradients ($> 10^3$ G/cm) can be realized with currents of only a few amperes.

The quadrupole side-guide is an acceptable trap configuration for cold atoms ($T \gtrsim 1\mu$K); however, as the temperature of the trapped atoms reaches lower temperatures (e.g. near the BEC phase transition) they become more susceptible to Majorana spin flips. At the zero of the magnetic field, where the Larmor precession frequency of the atoms is lowest, the atoms are no longer able to adiabatically follow the change in the field gradient and are likely to undergo a spin-flip transition to an untrapped, strong-field seeking state [80]. However, this problem can be ameliorated by adding a second bias field, B_x, along the direction of current flow in the wire. In doing so, the magnetic field minimum is lifted from zero and the field gradient near the minimum becomes approximately harmonic, forming a Ioffe-Pritchard (IP) trap [81]. So long as the Larmor frequency, $\omega_{Larmor} = \mu B_y/\hbar$, is much larger than the harmonic IP trap frequency, ω_{IP}, losses due to Majorana transitions can be considered to be negligible [76]. Solid lines in Figure 3.2 show the magnetic field of a side-guide IP trap relative to the same field where B_x is absent.

Two key figures of merit for IP traps are the trap frequency and depth. The trap depth is determined by the field magnitude infinitely far away from the wire, which is set by the bias field perpendicular to the current carrying wire, B_y. In order to determine the trap frequency we again look at the field near the trap minimum, this time taking the second spatial derivative,

$$B''|_{d_z} = \left(\frac{2\pi}{\mu_0}\right)^2 \frac{B_y^4}{B_x I_x^2} = \frac{B_y^2}{B_x d_z^2}. \tag{3.8}$$

Assuming the potential to be harmonic (i.e., $U_{z,mag} = m\omega^2 z^2/2$), Equation (3.8) in conjunction with Equation (3.1) to yield the side-guide IP trap frequency,

$$\begin{aligned} \omega_{IP,side} &= \sqrt{\frac{\mu_{mag}}{m} B''|_{d_z}} = \frac{B_y}{d_z}\sqrt{\frac{\mu_{mag}}{m}\frac{1}{B_x}}, \\ &\propto \frac{B_y^2}{I_x\sqrt{B_x}}. \end{aligned} \tag{3.9}$$

When designing an atom chip trap, Equations (3.6) and (3.9) are instrumental in understanding the interplay between the trap position with respect to the chip surface and the trap frequency, given control parameters I_x, B_x, and B_y.

3.2.2 Split-guide trap

The side-guide IP trap is sufficient for many atom-chip-based experiments. However, the atomtronics experiments described in Chapter 5 require unobstructed optical access to the atoms in order to project optical potentials down onto the trapped atoms and also image them *in situ*. Thanks to the atom chips discussed in Section 3.3, which are constructed from compound substrates that incorporate co-planar regions of silicon and glass, through-chip optical access is not an issue. Instead, one is restricted by the fact that the side-guide IP trap confines the atoms directly beneath one of the chip wires. While the wire is an excellent conductor, this also means it is completely opaque at the optical wavelengths relevant to our experiment. To side step this issue, the chip design is modified as follows: a second chip wire is added that runs parallel to the original side-guide wire and carries the same magnitude

current but in the opposite direction. Additionally, the external bias field is rotated to point perpendicular to the plane of the two wires. The resulting magnetic field minimum is shifted out from under the single wire to a position half-way between the two wires. The total magnetic field is now described by

$$B_{\hat{y},split} = \frac{\mu_0 I_x}{2\pi}\left(\frac{z}{(y-d_w/2)^2+z^2} - \frac{z}{(y+d_w/2)^2+z^2}\right), \tag{3.10}$$

$$B_{\hat{z},split} = \frac{\mu_0 I_x}{2\pi}\left(\frac{y+d_w/2}{(x+d_w/2)^2+z^2} - \frac{y-d_w/2}{(y-d_w/2)^2+z^2}\right) - B_z, \tag{3.11}$$

where d_w is the distance between the two wires. The total split-guide trap configuration is shown in Figure 3.3.

To determine the distance between the trap and the plane of the two wires, we follow the same procedure used for the side-guide and solve $d_z = z$ where the total field magnitude is zero. With currents of equal magnitude in both wires this is simplified further, as the trap is centered along the plane $y = 0$. The distance d_z for the split-guide trap is then given by

$$d_z = \sqrt{\frac{\mu_0}{2\pi}\frac{I_x d_w}{B_z} - \frac{d_w^2}{4}}. \tag{3.12}$$

Upon examination, the expression for d_z reveals a subtle issue. If the magnitude of the current flowing in the wires is not sufficiently large ($I_x < \pi d_w B_z/2\mu_0$), the solution becomes imaginary. This occurs when the field from the wires is no longer large enough to cancel the bias field at $d_z > 0$. Therefore, the trap is located in plane of the two wires, and the single trap minimum splits, creating two side-guide traps between the wires.

Assuming the chip wire current is large enough to form a single, split-guide trap, the gradient of the magnetic field at $z = d_z$ is then given by the first spatial derivative,

$$B'|_{d_z} = \frac{4\pi}{\mu_0}\frac{B_z^2}{I_x}\frac{d_z}{d_w}. \tag{3.13}$$

As with the side-guide, the split-guide trap can be made harmonic, i.e., suitable for trapping ultracold atoms, by adding B_x, and the trap depth is now determined by the magnitude of B_z. Following the procedure from Section 3.2.1, the trap frequency is calculated using the

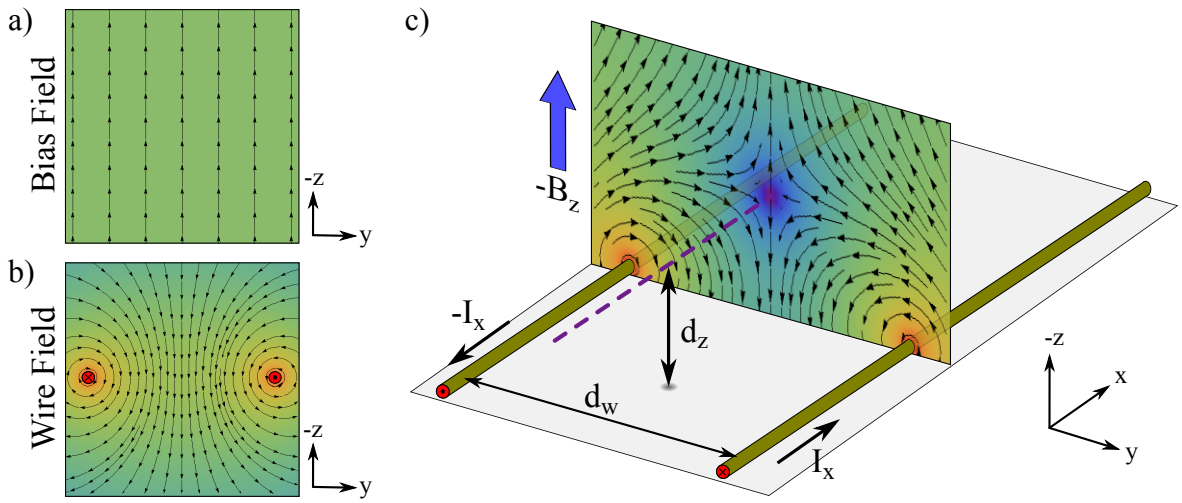

Figure 3.3: Illustration of the magnetic field lines in the split-guide configuration, which consists of a uniform bias field along $\hat{z}$, shown in (a), and the magnetic field generated by counter-propagating currents in a pair of parallel wires separated by a distance d_w, shown in (b). c) The resulting waveguide is located a distance d_z from the plane of the conductors. Colors indicate the magnetic field strength in the y-z plane, increasing from a local minimum (purple) to the maximum field at the two conductors (red).

second spatial derivative of the total magnetic field, given by

$$B''|_{d_z} = \left(\frac{4\pi}{\mu_0}\right)^2 \frac{B_z^4}{B_x I_x^2}\frac{d_z^2}{d_w^2}, \tag{3.14}$$

to yield

$$\begin{aligned} \omega_{IP,split} &= \sqrt{\frac{\mu}{m}B''|_{d_z}} = \left(\frac{4\pi}{\mu_0}\right)\frac{B_z^2}{I_x}\frac{d_z}{d_w}\sqrt{\frac{\mu}{m}\frac{1}{B_x}}, \\ &\propto \frac{B_z^{3/2}}{\sqrt{I_x B_x}}. \end{aligned} \tag{3.15}$$

Interestingly, $\omega_{IP,split} = \omega_{IP,side}$ for $d_w = 2d_z$, which is satisfied when $I_x = 2\pi d_z B_z/\mu_0$.

The design process for a split-guide atom chip trap is the same as for the side-guide, except one must consider the distance between the wires. Since the purpose of the split-guide trap is to gain unobstructed optical access to the trapped atoms, d_w and d_z must accommodate a solid angle larger than that of the primary objective in the optical system. Assuming the window in the chip substrate has a large enough clear aperture, the chip wire limited numerical aperture is given by

$$\begin{aligned} \mathrm{NA}_{wire} &= \sin\left(\arctan\left(\frac{d_w}{2d_z}\right)\right), \\ &= \frac{1/\tilde{d}_z}{\sqrt{4 + 1/\tilde{d}_z^2}}, \end{aligned} \tag{3.16}$$

where $\tilde{d}_z = d_z/d_w$. A schematic illustrating the through-chip optical access is shown in Figure 3.4(a). To provide context to the optical system described in Chapter 5, Figure 3.4(b) shows NA_{wire} versus $\tilde{d}_z$, which indicates that the maximum ratio of d_z to d_w for a 0.6 NA primary objective is $\sim 2/3$.

3.2.3 H-wire trap

Thus far, only waveguides that confine atoms along two dimensions have been considered. Both the side- and split-guide potentials can be modified to form full, three-dimensional trapping potentials by superimposing another magnetic field with spatially varying magnitude along the $\hat{x}$-direction. This is accomplished by running current through a pair of parallel

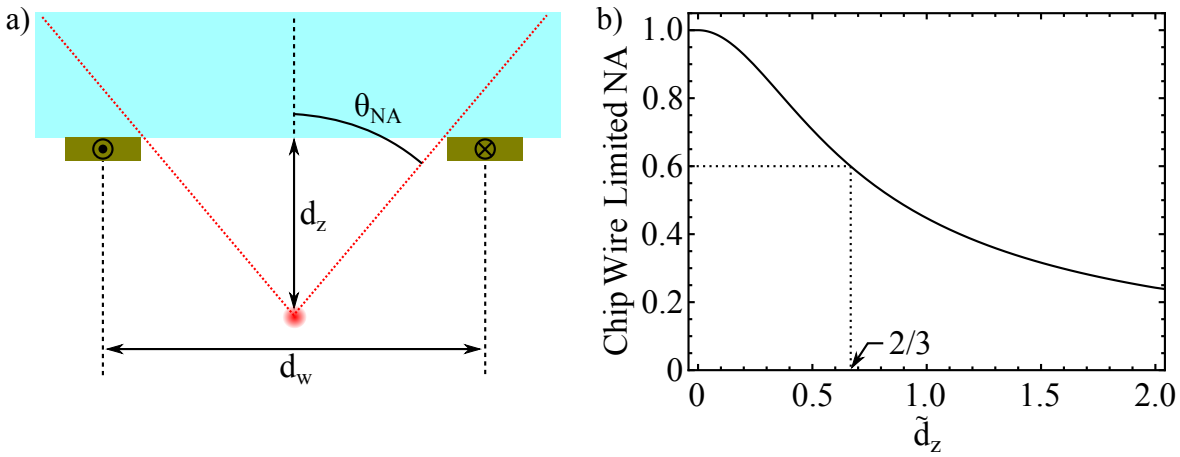

Figure 3.4: a) Illustration of the maximum thru-chip numerical aperture: The maximum ray angle depends on the chip wire separation, d_w, and trap-to-chip distance, d_z. b) Plot of the chip wire limited NA versus $\tilde{d}_z$. Dotted lines indicate the maximum $\tilde{d}_z = 2/3$ that still accommodates the imaging and projection system described in Chapter 4, which has an NA of 0.6.

conductors oriented perpendicular to the main guide wire(s) to form an 'H'-shape that gives the H-wire trap configuration its name. The contribution to the total magnetic field along $\hat{x}$ is treated in the same manner as a side-guide. Figure 3.5 shows an example potential generated by the H-wire configuration with a single side-guide wire. Here, the H-wires are separated by a distance $d_H = 2.2$ mm, both the H- and guide-wire currents are $I_{H,G} = 2$ A, and bias fields along $(x, y, z) = (1, -30, 0)$ G. The resulting trap is ~ 130 μm below the chip with trap frequencies $\omega(x, y, z) \simeq (25,\ 2100,\ 2100)$ Hz and a depth of $\sim$30 G.

Design parameters for the H-wire trap are dictated primarily by the ratio of currents, I_H/I_G, and the ratio of distances, d_z/d_H. The potential along the $\hat{x}-$direction is seen to be quite anharmonic; however, through careful selection of $I_{H,G}$ and $d_{H,z}$ the anharmonic contributions can be reduced [11]. Additionally, there is a noticeable twist to the potential in which the longitudinal trap axis is rotated away from the $\hat{x}$-axis by θ_H. This twist arises due to the perpendicular contribution of the H-wire field and is accentuated at higher field magnitudes. Near the trap minimum, the twist $\theta_H \propto (d_z/d_H)^2$, which indicates that the twist is minimized by increasing the distance between the H-wires or moving the trap closer to the chip.

3.2.4 T-wire trap

The primary utility of the H-wire trap is to provide loose confinement along the untapped axis of the guide traps. If instead a potential with tight confinement along $\hat{x}$ is desired, as is required for rapid rethermalization during the RF evaporation process used to form a BEC, a single conductor oriented perpendicular to the guide wire(s) can be added to the chip wire pattern. By flowing current in the opposite direction of the H-wire current, a dimple is produced in the longitudinal potential profile. The wire pattern can form either a '+' or '$\top$' relative to the horizontal guide wire, where the former is referred to as a dimple trap and the latter as a T-wire trap. This section considers the T-wire trap, as the vertical dimple wire would obscure optical access to the atoms. More information on dimple traps

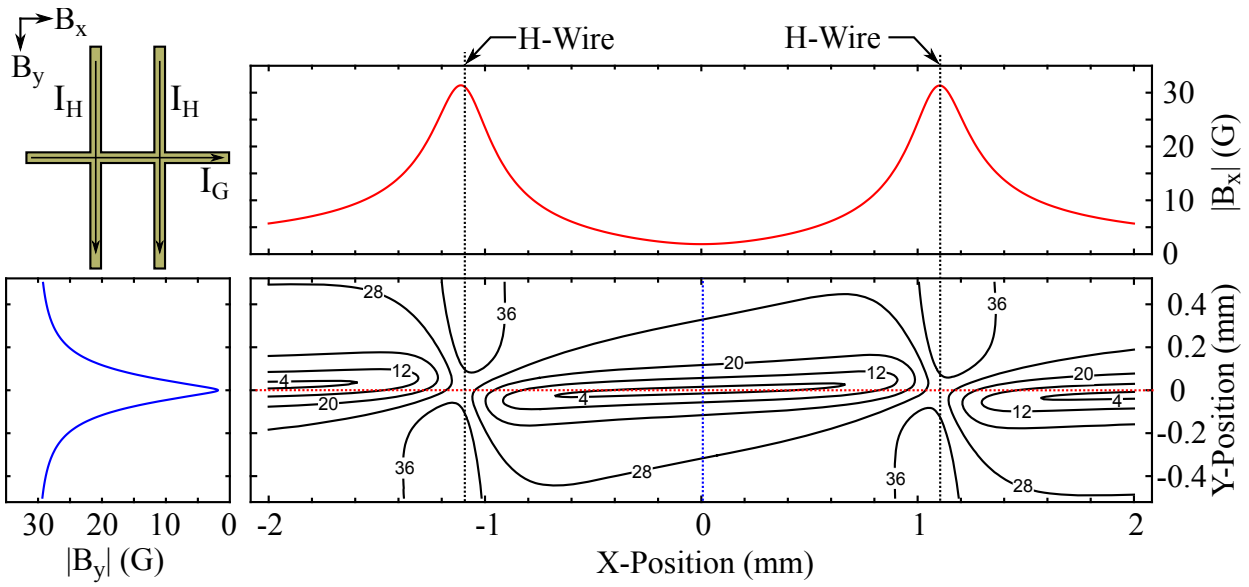

Figure 3.5: H-wire trap configuration: The inset at the upper left illustrates the conductor scheme along with the wire current and bias field directions. The central energy contour plot shows the highly elongated trap shape. Each contour line is labeled with the field magnitude in Gauss (G). The dotted red and blue lines through the center of the trap indicate the position of slices through the trap along the $\hat{x}-$ and $\hat{y}-$directions that are shown above and to the left, respectively.

can be found in the theses of Salim and Hudek [82, 13]. Figure 3.6 illustrates the T-wire potential, again with H-wires separated by a distance $d_H = 2.2$ mm, but with wire currents $I_H = 1.75$ A, $I_G = 2.5$ A, $I_T = 0.75$ A, and bias fields along $(x, y, z) = (6.7, -30, 0)$ G. The resulting trap is also located ~ 130 μm below the chip with a depth of $\sim$30 G, but now has trap frequencies $\omega(x, y, z) \simeq 2\pi \times (350,\ 2100,\ 2100)$ Hz.

Design parameters for the T-wire trap are almost identical to those of the H-wire trap and are conceptually quite similar. The T-wire current can be setup to either run parallel or antiparallel with respect to I_G in the main guide wire, resulting in increased or decreased total current through the shared section of the guide wire, respectively. Both configurations can be used to generate T-traps, and the radial trap parameters can be tuned to match the H-wire trap by decreasing or increasing the magnitude of I_G, leaving B_y unchanged. To account for the magnetic field contribution from the T-wire current that runs antiparallel to the H-wires, the magnitude of B_x is increased, allowing I_H to be decreased. In doing so, the trap bottom and depth can be tuned to match that of the H-wire trap. Typical T-wire trap parameters do not require a large current in the T-wire. As Figure 3.6 shows, less than 1 A in the T-wire generates a dimple in the longitudinal trapping potential that is ~ 5 Gauss (350 μK) deep and increases the mean trap frequency to $\sim 2.5\times$ that of the H-wire trap.

3.3 Atom chip designs

The previous section covered the basic concepts for both side- and split-guide traps along with H- and T-wire traps. Each of these trap geometries is used at different stages of the atomtronics experimental cycle, described further in Section 5.1. The sections that follow give an overview of the conductor patterns that were designed for and implemented in the experimental work of this dissertation.

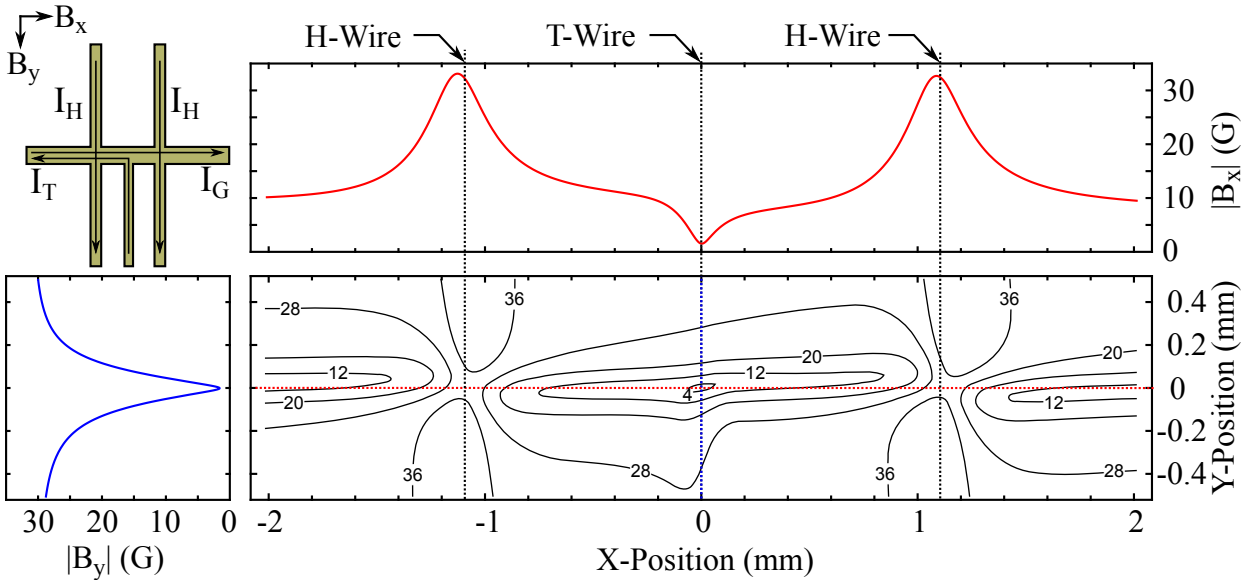

Figure 3.6: T-wire trap configuration: The inset at the upper left illustrates the conductor scheme along with the wire current and bias field directions. The central energy contour plot shows the elongated trap shape similar to the H-wire trap with an additional dimple generated by the T-wire at trap center. Each contour line is labeled with the field magnitude in Gauss (G). The dashed red and blue lines through the center of the trap indicate the position of slices through the trap along the $\hat{x}-$ and $\hat{y}-$directions that are shown above and to the left, respectively.

3.3.1 Atom chip standardization

Atom chip fabrication in the Anderson lab is largely standardized. The historical evolution of our atom chip construction can be found in the theses of Du [83], Squires [10], Segal [11], Salim [82], and Hudek [13]. At the heart of our chip technology is the compound substrate on which the chip conductors are lithographically patterned. Constructed of co-planar regions of high conductivity silicon and optically transparent Pyrex, the substrate provides hermetically sealed electrical and optical feedthrough [82, 84]. This co-planar design enables conductors to be patterned directly atop transparent regions of the chip, and in turn allows atoms to be trapped below an optical surface. When bonded to one of our double-MOT cells, the chip then serves as one of the walls of the vacuum chamber, allowing high-numerical aperture optics to be placed $\lesssim 1$ mm from the atoms.

3.3.2 The V2 window chip for in-trap imaging

The V2 window chip is the second generation of window chip used to produce BECs and image them through the chip window (the first being the V1 window chip described in the thesis of Evan Salim [82]). This chip design, shown in Figure 3.7, incorporates the previously discussed split-guide design patterned directly over the central, 2 mm diameter chip window. The chip design includes wires for both H- and T-wire trap configurations. As a design constraint, the infinite wire approximation only remains valid so long as the width of the wires, w_w, is much less than the distance from the wire to the atoms. To combat the high resistance of thin wires, the width of individual conductors on the vacuum side of the atom chip is $w_w = 100$ μm.

One caveat to this conductor pattern is the inevitable junction between the guide, T-, and the H-wires, if all conductors are on the same side of the chip. Multiple intersecting (i.e., shorting) wires require independent, floating current drivers for each separate current path. This is feasible but becomes cumbersome and undesirable for more than two intersecting

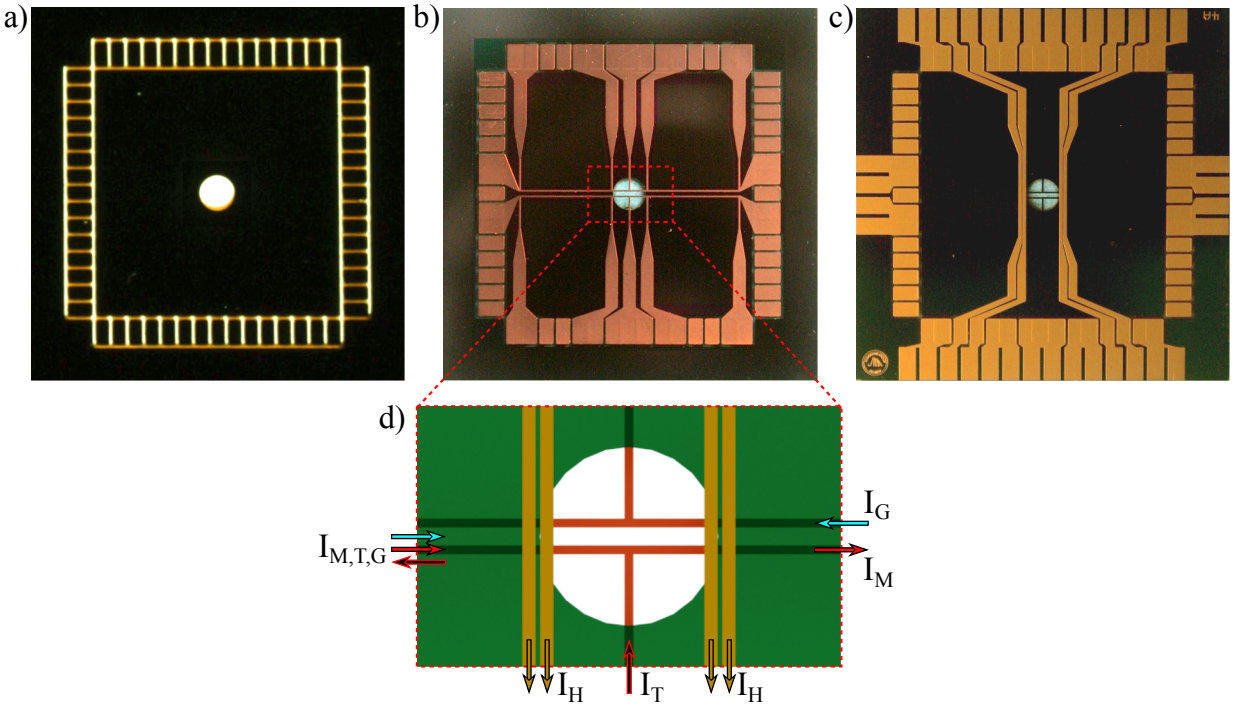

Figure 3.7: a) Bare compound substrate prior to metallization process. b) Vacuum side of the V2 window chip with copper conductors. c) Ambient side of V2 window chip with gold conductors. d) X-ray schematic view of the central region of the chip with the chip current paths used in the V2 window chip. As shown, the lower T-wire is used in the side-guide, T-wire, and split-guide traps. The current direction in the lower of the two horizontal wires are labeled I_M, I_T, and I_G, respectively.

current paths. By running multiple floating current supplies, one runs the risk of developing high voltages between supplies and therefore across the chip, which can cause breakdown in the dielectric layer. Therefore, the V2 window chip conductor design places the H-wires on the ambient side of the chip substrate while the T- and guide-wires are on the vacuum side. The dielectric coating on the chip provides electrical isolation between the vacuum and ambient sides of the substrate, so the H- and guide-wires are driven by current supplies with a common ground reference and the T-wire driver floats. The downside to this configuration is that the H-wires are now displaced by 420 μm (the thickness of the chip) from the guide wires. This results in a decrease in the longitudinal confinement that goes as $\sim 1/r$. To account for this decrease, the H-wire width is increased to 150 μm to accommodate larger currents and doubled up, with two conductors running immediately parallel to one another.

By moving the H-wires to the ambient side of the chip, the overall trapping potential generated by both the H-and T-wire traps discussed in Sections 3.2.3 and 3.2.4 are modified. Figure 3.8 illustrates these changes. Here, the conditions are identical except the H-wire current is doubled and a second pair of H-wires separated by 2.4 mm is added, reproducing the V2 window chip design. The increased distance between the H-wires and the trap location, due to the wires being on the ambient side of the chip, causes the magnetic field generated by the H-wires to appear more like an additional x-bias field, which smooths out the longitudinal trapping potential and reduces both the trap depth and mean trap frequency. The trap profiles indicated by the solid lines in Figure 3.8 show the trap in which the majority of the evaporation is completed during typical experimental cycles.

Once a BEC is created in the T-wire trap, the atoms must be transferred out from under the wire and into a split-guide potential to gain optical access to the atoms. The vacuum side conductor pattern is mirrored across the center of the chip, which also provides a redundant T-wire. This can be seen in Figure 3.7(b), in which the top and bottom halves of the vacuum side metallization are mirror images separated by $d_w = 340$ μm. Given this separation and $w_w = 100$ μm, the split-guide wires satisfy the condition that the $NA_{wire} > 0.6$ for values of

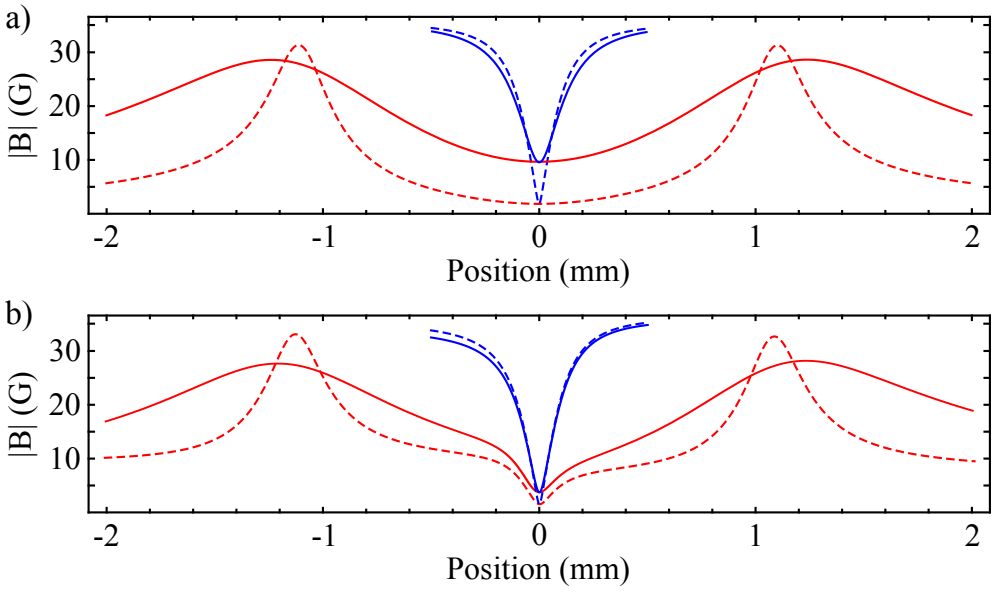

Figure 3.8: a) Comparison of H-wire traps in which the H-wires are on the same side (dashed) and opposing sides (solid) of the chip substrate as the guide wire. b) Comparison of T-wire traps in which the H-wires are on the same side (dashed) and opposing sides (solid) of the chip substrate as the guide and T-wires. In both (a) and (b) the longitudinal and radial trap profiles are shown in red and blue, respectively.

$d_z \lesssim 160$ μm.

The imaging trap is generated by running equal currents, I_G, antiparallel through the two guide wires and a vertical bias field, as described in Section 3.2.2. By this point in the experimental cycle, the atomic ensemble is ultracold and the trap depth, even at low wire currents, is much greater than the energy scales of the ensemble. Typical experimental parameters are $I_G = 2$ A, $I_H = 1$ A, and bias fields along $(x, y, z) = (1, 0, -30)$ G. Fine tuning of the radial and longitudinal trap frequencies is accomplished through small changes to B_x and I_H. These two parameters vary the magnitude of the magnetic field at the trap bottom, which changes the field curvature without adjusting the position of the trap. In this way, the trap frequencies are widely tunable from hundreds of Hz to a few kHz radially and from tens of Hz to hundreds of Hz longitudinally. This chip design is utilized for the majority of the experimental work described in this dissertation.

3.3.3 The V3 window chip, a double split-guide and other design upgrades

Despite the great success of the V2 window chip, several aspects of the design required minor adjustments. Modifications include the addition of a second set of H-wires with increased spacing along with a second pair of guide wires for the split guide trap. The central window in the chip substrate is also anti-reflection (AR) coated to improve optical performance. These changes look to improve the utility of the chip without drastic changes to its overall functionality. The V3 chip design, including the current path schematic, is shown in Figure 3.9.

Thus far, chip design has been discussed under the approximation of infinitely thin chip wires. As mentioned previously, this assumption holds when the trap is far from the conductor $d_z \gg w_w$. Even then, a trap located $d_z \lesssim w_w$ from a straight conductor will only suffer from a reduced gradient due to the finite spatial extent of the current density in the conductor, which can be accounted for analytically [13]. However, this issue is accentuated in the case that atoms are in close proximity to a wire that bends, widens, or intersects

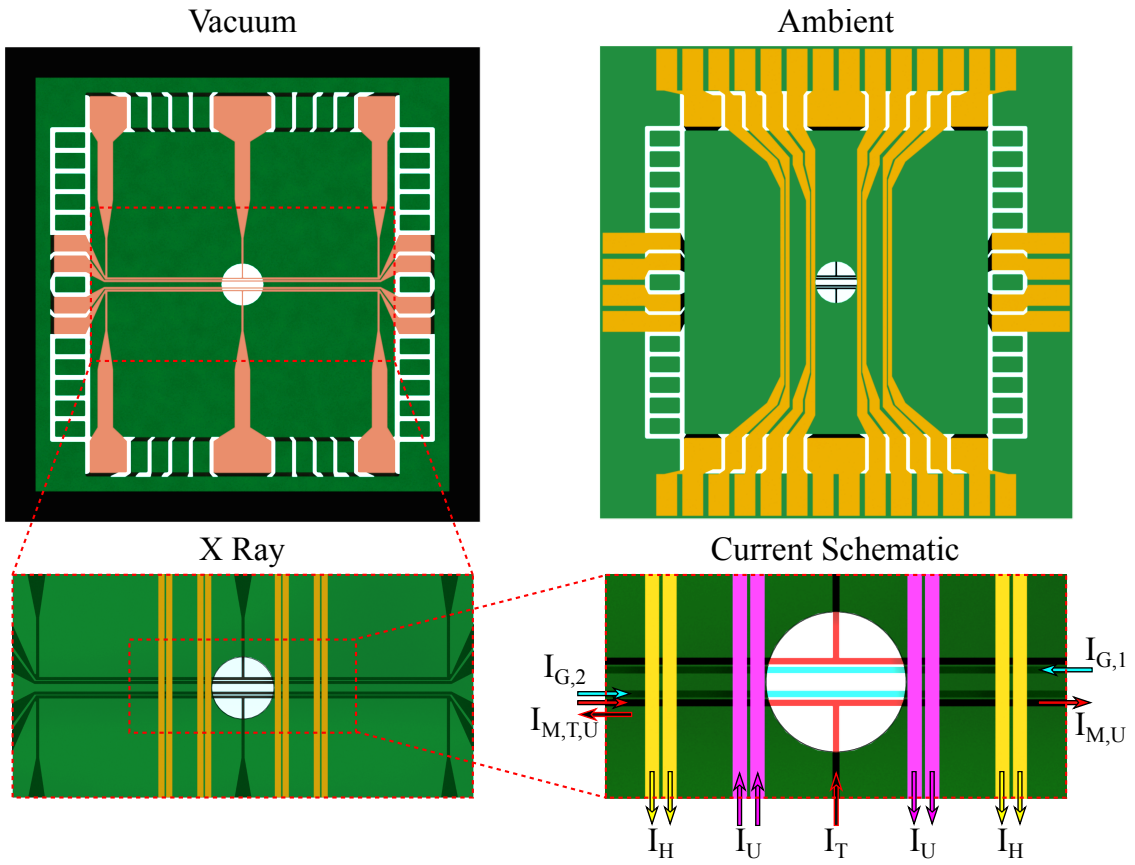

Figure 3.9: View of the ambient and vacuum sides of the V3 window chip that incorporates a second pair of guide wires. An X-ray view of the chip is also shown along with the current direction for various chip trap configurations including H- and T- traps, the split-guide trap, and the U-trap.

another wire. The current density within wires at locations such as these is non-trivial and in order to model the trap correctly, finite element analysis (FEA) is necessary. Modeling the traps generated by our atom chips is done using FEA software that was developed in conjunction with Boulder Labs Inc. [85].

The first addition to the V3 window chip ameliorates unwanted kinks in the magnetic field that occur at the T-wire junctions of the split guide wires. As current flows through each guide wire, two issues arise. First, a region of reduced current density manifests within the guide wire as electrons pass through a region of increased cross-section at the wire junction. Figure 3.10 shows an example of the current density in the central region of the mirrored T-wires. Second, as a result of the modified current density, a non-zero projection of the magnetic field is generated perpendicular to the intended direction. These factors result in a distortion of the magnetic field near the trap minimum. The longitudinal profile of the split-guide trap, shown in Figure 3.11 as the solid line, is impacted the most and exhibits a 'kink' in the potential energy with magnetic field artifacts on the order of $\sim 1/4$ G (~ 20 μK). The typical temperature of the atomic ensemble in the split-guide trap is $\lesssim 1$ μK. Therefore, the atoms become trapped in the new minima and the longitudinal trap frequency is no longer dictated by the H-wires. Instead, the longitudinal trap curvature is determined by the distance between the atoms and the T-wire junction as well as the relative decrease in current density within the conductor. The simple solution to this problem is the addition of a second pair of parallel guide wires that serve as the new split-guide trap. These wires are colored light blue in the current schematic shown in Figure 3.9. By removing the T-wire junction from the split-guide wires the longitudinal profile, shown as the dashed line in Figure 3.11, is once again harmonic and tunable by I_H.

The second addition to the V3 window chip is an additional set of H-wires, with twice the original spacing and a width of $w_w = 200$ μm. The addition of more H-wires provides flexibility to chip loading schemes as well as the longitudinal confinement of the chip traps. Use of the wider spaced H-wires enables lower longitudinal trap frequencies (~ 10

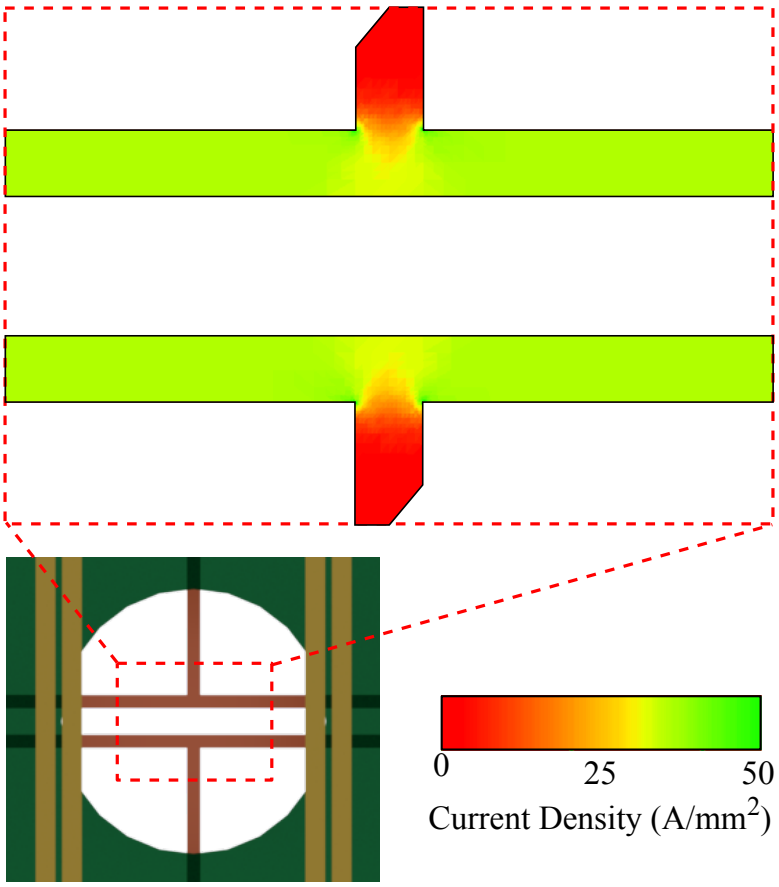

Figure 3.10: FEA of the current density at the intersection of the chip T-wires. Current density increases from red to green. The brief excursion of the guide wire current into the junction leads to a depletion in the current density of $\sim 20\%$.

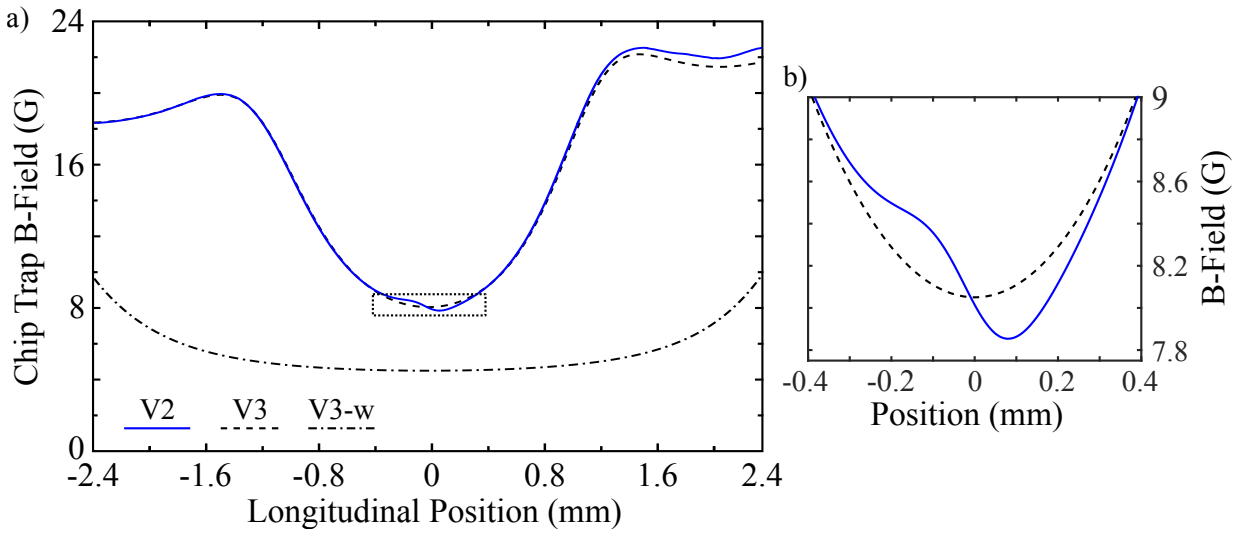

Figure 3.11: a) Comparison of the split guide trap fields for V2 (solid) and V3 (dashed) window chips. Elimination of the T-wire intersection in the V3 chip enables looser longitudinal confinement controlled by the H-wire current. Furthermore, the V3 chip includes a second, wider spaced set of H-wires. The longitudinal profile with this new set of H-wires (V3-w) is shown by the dot-dashed line for the same chip current and bias field conditions. b) Close up around the field minimum of the V2 and V3 traps indicated in (a) by the dotted rectangle. The kink in the longitudinal profile is eliminated when guide wires without a T-wire junction are used for the split-guide.

Hz) without also greatly reducing the trap depth. Figure 3.11 includes a comparison of the longitudinal confinement in the split-guide trap using the inner or outer pairs of H-wires, with equal I_H.

Another important consideration for chip design is the method of initially loading atoms from the previous, external magnetic trap into the chip trap. To achieve optimal chip loading efficiency, it is necessary to mode match the quadrupole trap created by external coils to the magnetic field generated by the chip [71]. The chip trap configurations discussed thus far do not provide optimal mode matching; however, by running current in a U-shape on the chip with a single bias field it is possible to generate a trap that mimics the external quadrupole. This current path is shown in Figure 3.9, labeled I_U, and utilizes the inner H-wires along with one of the main guide wires in conjunction with a bias field oriented along the same direction as in the side-guide. Systems that load the chip trap directly from a mirror-MOT commonly use this loading scheme [83, 86].

Lastly, in addition to the updated conductor pattern, the chip window is coated for several wavelengths ($< 0.6\%$ reflectivity from $760 - 790$ nm and 99.92% reflectivity at 1064 nm at normal incidence). The high-R coating was utilized in conjunction with steering optics anodically bonded to the chip to demonstrate an on-chip optical lattice by Straatsma and colleagues at ColdQuanta [87]. In that work, optics were bonded to the atom chip in regions where the dielectric coating was stripped during chip fabrication.

3.4 Technical considerations for atom chip traps

Once the atom chip design is determined to adequately meet the requirements of the experimental goals, one must consider other, more technical aspects. These include the power dissipation within the chip during the experiment cycle and the effect of technical noise in the wire currents on the atoms trapped in the magnetic potential. While they impact different parts of the system, both heating related issues require careful attention when designing and conducting experiments in an atom-chip-based apparatus. The analysis

provided in the following sections is useful in understanding both topics.

3.4.1 Ensemble heating in the split-guide trap

When implementing any magnetic trap design to produce and study ultracold atomic systems, one must consider the heating rate of the trapped ensemble due to various mechanisms. Heating in magnetic traps can be caused by fluctuating currents in the chip wires, due to either technical noise or thermal currents, as well as collisional processes such as dipolar relaxation [76, 88]. This section addresses the role of technical noise in the heating rate of atoms confined in the split-guide potential and follows the analysis reported on in References [76, 89, 90].

Under the harmonic oscillator approximation of the atom chip magnetic trap, the rate at which atoms are excited is given by

$$\Gamma_{ex} = \frac{a^2}{4\hbar^2} S_F(\omega_t), \tag{3.17}$$

where a is the harmonic oscillator length and $S_F(\omega_t)$ is the noise spectrum of the trapping force at the oscillator frequency, ω_t. From this, the rate of energy transfer to the excited atom is given by $dE = \hbar\omega_t\Gamma_{ex}$. A more accessible parameter than the force exerted by the magnetic trap is the position of the trap minimum, which are related by $F = m\omega_t^2 z$ where z is the position of the trap relative to the chip. The rate of energy transfer due to fluctuations in the trap position is

$$dE = \frac{m\omega_t^4}{4} S_z(\omega_t), \tag{3.18}$$

and depends strongly on the trap frequency, scaling as $dE \propto \omega_t^4$.

These equations can be applied to the split-guide trap by looking at the trap position fluctuation spectrum caused by noisy current supplies. The position fluctuation spectrum is determined from Equation (3.12) for $z = d_z$, in conjunction with measurements of the

current driver noise spectra. Recalling the form of the trap position in $\hat{z}$ relative to the chip,

$$d_z = \sqrt{\frac{\mu_0}{2\pi}\frac{I_x d_w}{B_z} - \frac{d_w^2}{4}}, \tag{3.19}$$

one sees that fluctuations in d_z depend on both the chip currents as well as the external bias field. The magnetic field generated by the square z-bias Helmholtz coil pair is given by

$$B_z = \frac{8\mu_0 N_t I_b}{\sqrt{125}W}, \tag{3.20}$$

where N_t is the number of turns in each coil, I_b is the current in the coil, W is the half-width of the coil, and the coil pair is separated by $2W$. Combining the current noise spectra of both the coil and chip currents yields the total position fluctuation spectrum, $S_z(\omega_t) = (\partial d_z/\partial I_x)S_{I_x}(\omega_t) + (\partial d_z/\partial I_b)S_{I_b}(\omega_t)$. The current noise spectra for the chip and coil current drivers, both of which are designed and built in our lab, were measured using a Stanford Research Systems SR780 spectrum analyzer in a frequency band from $1-2$ kHz. Across these frequencies, the noise spectra are fairly flat with $S_{I_x} \approx 35$ nA$/\sqrt{\text{Hz}}$ and $S_{I_b} \approx 120$ nA$/\sqrt{\text{Hz}}$.

The heating rate in the split-guide trap was determined by measuring the temperature of the atomic ensemble after hold times of various duration, using the temperature fitting method described in Section 4.2.1. Measurements were made for radial trap frequencies ranging from $\sim 200-3400$ Hz, with an ensemble of $\sim 10^4$ atoms at a temperature $T \approx 1.5T_c$. Results of this measurement are compared to the theoretical heating rate in Figure 3.12. Disagreement in the measured and calculated heating rates at low trap frequencies is in part due to the excitation of a slosh mode while loosening the trap and higher values of $1/f$ noise of the current drivers. Unfortunately, technical noise limits the trap frequencies used in the atomtronics experiments to below ~ 2 kHz. At higher trap frequencies, the resulting decrease in condensate lifetime is too severe, dropping below ~ 100 ms for $\omega_t/2\pi > 2$ kHz. In order to reach higher trap frequencies without sacrificing the condensate lifetime, the current noise of the coil driver must be decreased, as it contributes more significantly to the observed heating than the chip current driver.

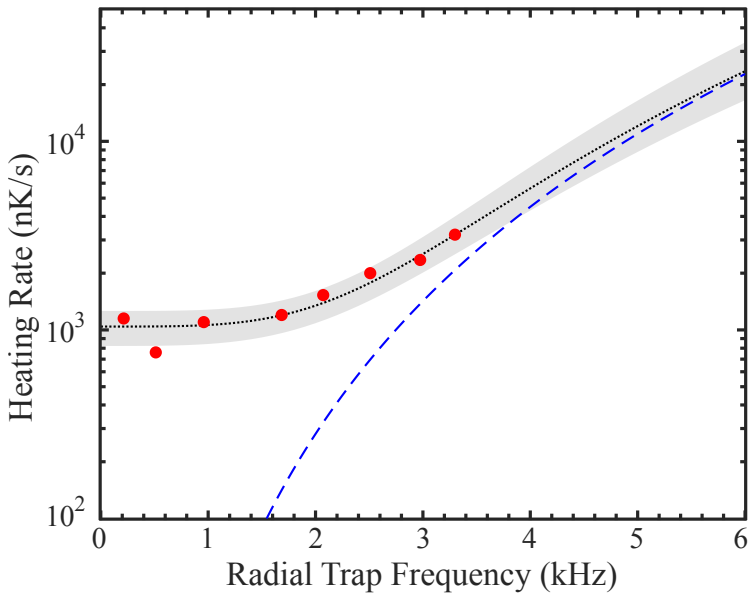

Figure 3.12: Comparison of the theoretical and measured heating rate in the split-guide trap. Red points indicate the measured heating rate. The fit to the data as well as the 95% confidence interval for the measured heating rate are shown by the black dotted line and gray band, respectively. At low radial trap frequencies the fit to the heating rate is higher than the theoretical rate, which is calculated using the measured current driver noise spectra and shown by the blue dashed line, but the two agree at higher frequencies.

3.4.2 Wire heating comparison in window and non-window chips

The previous sections have discussed chip conductor pattern designs that achieve the desired magnetic trap functionality in our atomtronics experiments. However, one of the primary concerns in chip design is heat management. Compared to other atom chip groups, whose chips are mounted to large copper blocks [91] and sometimes temperature stabilized [92, 93] to facilitate heat transfer out of the chip substrate, our atom chips have limited thermal mass and rely on convective cooling. In the event that thermal conduction to the chip substrate is inadequate, the results can be catastrophic, often resulting in the evaporation (burn-out) of the chip wire [94]. Yet, with proper consideration for the thermal conductivity of the chip substrate, conductor properties, and insulating dielectric layers, even complex, multilayered chips can be implemented successfully [95]. In this section the thermal performance of our two-layer, compound substrate atom chip is assessed using models for fast and slow heating. Chip designs with both 20 μm and 100 μm wide conductors are compared along with designs that include conductors patterned over the transparent chip window. Additional measurements provide information relevant to safe operating limits.

Wire heating test setup

Two atom chip designs were tested: A direct evaporation chip used in the thesis of K. Hudek [13] was chosen to represent the non-window, silicon substrate chips (labeled S), and the V1 window chip used in the thesis of E. Salim [82] represented the window chip substrate (labeled W). Each chip was bonded to a standard 3D MOT glass chamber and pumped down to $\sim 10^{-6}$ torr in order to reduce vacuum side convective cooling and emulate conditions in typical experiments. Electrical connection to the chip was made using pogo pins rated to 6A continuous current in air. Electrical properties of the chip were monitored by measuring the resistance of the chip wire in a 4-point probe configuration. Voltage and current data were recorded by a LabVIEW script and analog input card (NI cRIO-9215).

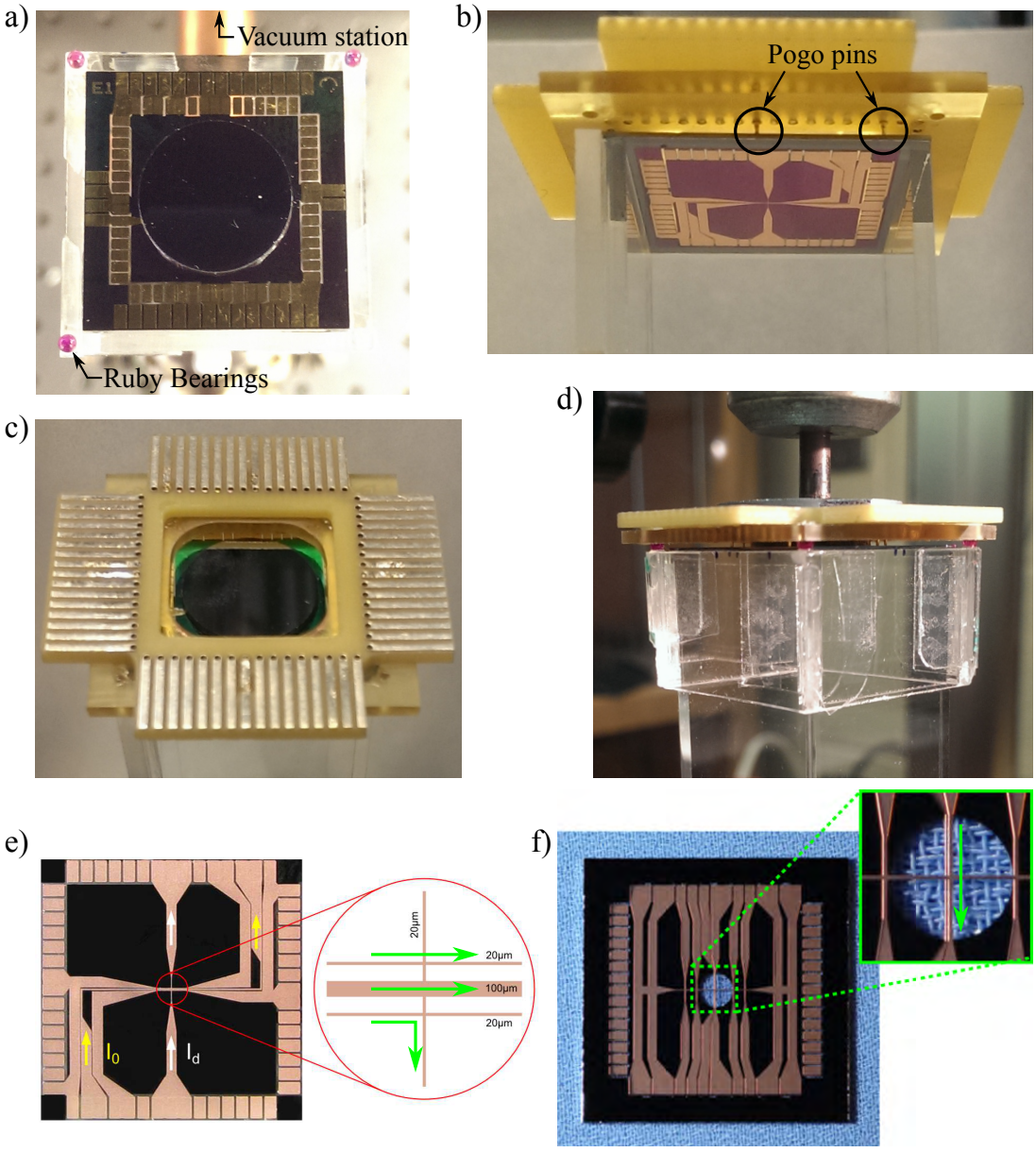

Figure 3.13: Pictures of the test setup used to determine the thermal properties of atom chips during current flow. a) Top side of direct evaporation chip bonded to a 3D MOT chamber and connected to the vacuum station. Ruby ball bearings epoxied to the cell walls serve to locate the prototype pogo pin chip connector. b) Underside of chip connector shows two pogo pins lined up with the gold pads on the top of the chip. c) Electrical breakout board for the chip connector. d) Complete prototype pogo pin chip connector attached to the cell and secured with a tap stand. e) Direct evaporation chip used to test non-window chip properties. Image credit [13]. f) V1 window chip used to test wires over Pyrex substrate. Image credit [82]. Insets of (e) and (f) show the wires used in the heating tests. Green arrows indicate current directions in the tests.

Models for fast and slow chip heating

Heating of the atom chip wires and substrate is modeled following the work of Groth et al [96]. Both fast and slow time scales are considered. Fast heating is determined primarily by the resistivity of the wire and the surface conductance, k, of the chip substrate. During the fabrication process, prior to metallization, a thin dielectric layer (SiO_2) is grown on the wafer in order to electrically insulate the high conductivity silicon of the chip substrate from the wires. Therefore, the surface conductance is determined by properties of the Cu-SiO_2-Si or Cu-SiO_2-Pyrex interface. The relative thermal conductivity of the substrate materials are $k_{SiO_2} \approx k_{\text{Pyrex}} \approx k_{\text{Si}}/100$ [97]. The change in conductor temperature just after a current, I, begins to flow is given by

$$\Delta T_{fast}(t) = \frac{h\rho j^2}{k - hj^2\alpha\rho}\left(1 - \mathrm{e}^{-t/\tau_{fast}}\right), \tag{3.21}$$

where $j = I/(hw)$ is the current density, h and w are the height and width of the conductor, respectively, and ρ is resistivity of the copper, which has a linearly approximated temperature coefficient α. The time constant associated with the heating is determined by the heat capacity of the wire, C_w, and is given by $\tau_{fast} = C_w h/(k - hj^2\alpha\rho)$. The slow heating process depends more strongly on the bulk thermal conductivity, λ, of the substrate, which determines how quickly the heat disperses through the substrate. After the initial fast temperature increase, the change in temperature is approximated by

$$\Delta T_{slow}(t) \approx \frac{\rho I j}{2\pi\lambda}\ln\left(\frac{4\pi^2\lambda t}{C_s w^2}\right), \tag{3.22}$$

where C_s is the substrate heat capacity. Since the substrate material varies across the length of the conductor, C_s is left as a fit parameter when analyzing the chip heating data.

Chip heating comparison

Chip heating in 100 μm wide wires on both the window and non-window chips is compared for current densities ranging from $j = 1 - 2 \times 10^3$ A/cm^2. The increase in the

chip wire temperature is determined from the relative change in the conductor resistance, $R/R_0 = 1+\alpha(T-T_0)$, where R_0 and T_0 are the initial chip wire resistance and temperature, respectively. Figure 3.14 shows four representative data sets in which the calculated temperature is shown as the black solid line and fits to the data using Equations (3.21) and (3.22) are shown as dashed lines. Since the fast heating time constant is dominated by the physical properties of the conductor rather than the substrate, the initial heating behavior of both the direct evaporation and window chips are similar, with $\tau_{fast} = 41.0(2.6)$ μs. Fits to the data also enable extraction of the effective values of k and λ for the two chips. Fits to the fast temperature increase yield the ratio $k_S/k_W = 8.71(0.73)$, indicating that heat transport from the wire, across the SiO_2 insulating layer, and into the substrate is nearly an order of magnitude lower for the window chip. This results in a much more substantial initial increase in the measured wire temperature within the first few milliseconds. While the ratio of surface conductivity is nearly flat across the range of current density, the ratio of bulk heat conductivity shows a strong dependance on the current density, j. For low j, $\lambda_U/\lambda_W \approx 3.75$, but the ratio increases exponentially as a function of the current density. Doubling j leads to $\lambda_U/\lambda_W \approx 14$, as λ_W decreases and λ_U remains nearly constant. Such a pronounced decrease in the window chip substrate conductivity reflects saturation of the heat capacity of the chip substrate. Ultimately, the reduction of the heat capacity sets the upper limit on the duration for which current can be run through the wire.

An array of additional heating measurements were performed, encompassing the typical operating parameters of our atom chips during normal operation in experiments. While neither of the chips failed under typical experimental conditions, it is valuable to determine the maximum current supported by the chip wires. Measurements of the relative change in the wire resistance were performed for increasing currents, each run for 3 seconds, i.e., the typical length of an BEC production cycle, until the conductor failed. The results are shown in Figure 3.15. In the case of the window chip, 4 A flowing in the 100 μm trace lead to failure after only 1.39 s, at which point the wire temperature reached 240°C followed by a

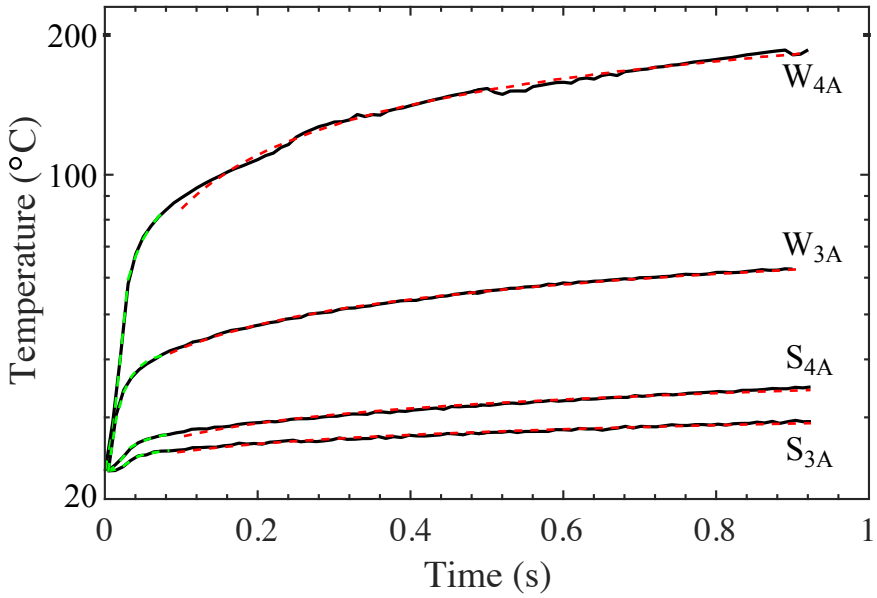

Figure 3.14: Comparison of the rate at which 100 μm wide chip traces heat up under current flow for two chips: one with wires patterned only across silicon (S) and the other where part of the wire is patterned over a 3 mm diameter Pyrex window (W). Green and red dashed traces indicate fits to the data using the fast and slow heating model equations, respectively, which are used to extract the surface heat conductance, k, and bulk heat conductivity, λ of the two chips. It is clear that the presence of the pyrex window reduces the rate at which heat is removed from the conductor.

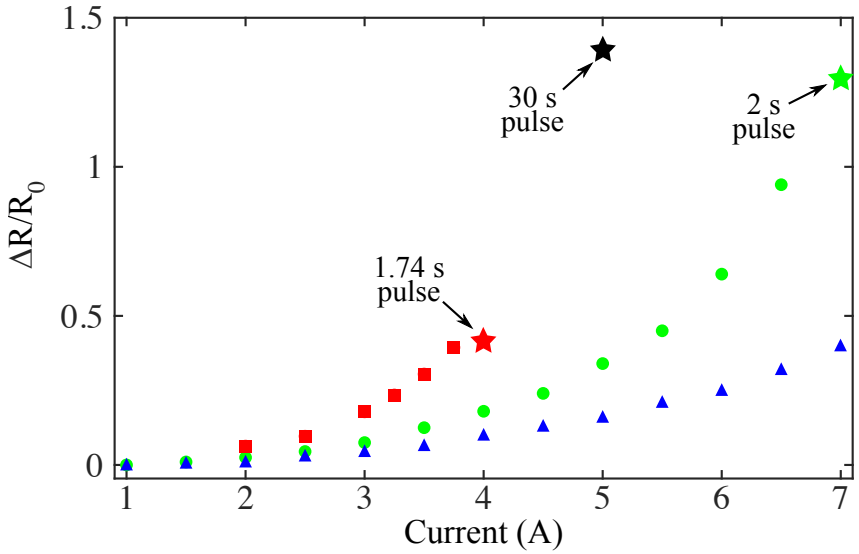

Figure 3.15: Relative increase in the chip wire resistance during a 3 second current pulse. Data sets for a 100 μm wide wire on the window chip (red square), along with 100 μm (blue triangle) and 20 μm (green circle) wide wires on the non-window chip are shown. Chip wire burn-outs for each data set are indicated by stars along with the respective time until failure.

rapid increase to $> 500°$C. As expected, the wire burned out directly over the chip window (see Figure 3.16(a)). By comparison, the heat conductivity of the 100 μm trace on the non-window test chip is sufficient to survive 4 A for > 30 seconds and 7A for > 3 seconds. Additional tests show that smaller, 20 μm traces on the non-window test chip fail after 30 seconds at 5 A and 2 seconds at 7 A, both near $\Delta R/R_0 \approx 1.25 - 1.4$. The failure locations in these tests are shown in Figure 3.16(b).

Knowledge of the chip wire resistance under repetitive use is of equal importance to the single shot maximum current. Given insufficient time to cool after an experimental cycle, the chip wire will reach higher peak temperatures during successive current pulses. The change in chip wire resistance at various duty cycles was measured for the non-window chip, and the results are shown in Figure 3.17. During a typical experimental run in the atomtronics apparatus an average of $2.5 - 3$ A is run through the main wire for a duration of $2 - 3$ seconds. Given the lower heat conductivity of the window chip and accounting for the currents in the second guide wire along with the H- and T-wires, the experimental cycle is conservatively limited to a duty cycle of 0.05, or once per minute.

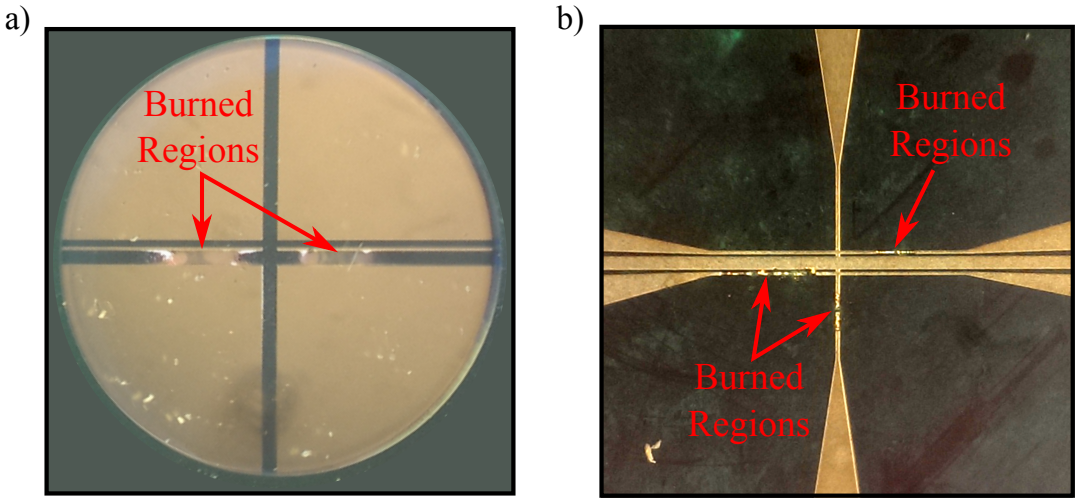

Figure 3.16: a) Picture of the burned out 100 μm wire that runs across the Pyrex window on the V1 window chip after 4 A of current was run through the wire for 1.39 s. The wire is partially lifted away from the window with dislocations in the wire at the points indicated. b) Picture of the central region of the direct evaporation chip showing two regions of the burned out 20 μm wire. The two traces failed after 7 A of current run for 2 s in the right-angle wire, and 5 A of current for 30 s in the straight wire. Note that the failures occurred in the center of the narrowest region.

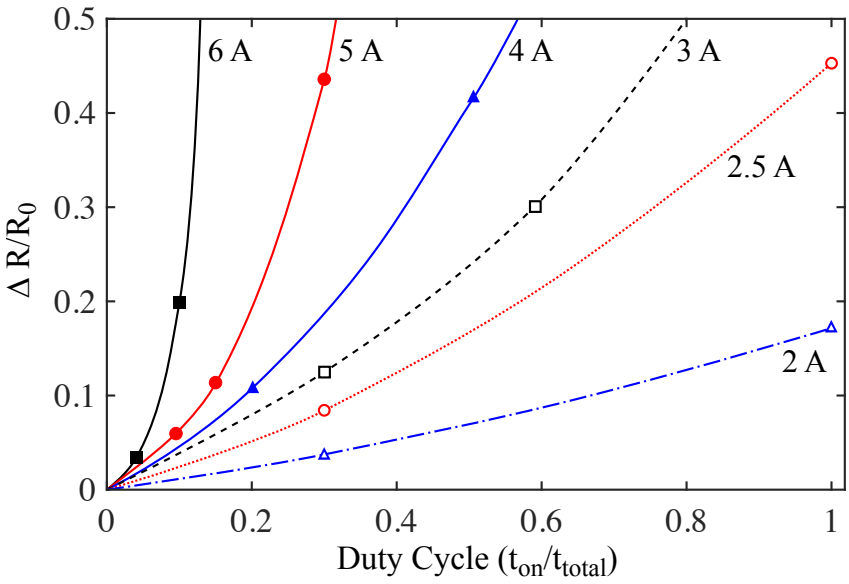

Figure 3.17: Increase in the 100 μm chip wire resistance on non-window chip under various current loads and a range of duty cycles. Points indicate measured values, while the lines are guides to the eye. Low currents can safely be run at a near unity duty cycle, as seen for 2A and 2.5 A. In conjunction with the data from Figure 3.15, the maximum safe duty cycle for a fixed chip current is given by the region to the left of each line.

Chapter 4

High-resolution imaging & optical control of ultracold atoms

Research over the past two decades has ushered in a new paradigm of quantum simulation that utilizes trapped, ultracold gases to study the behavior of complex condensed matter systems [98]. This research thrust has led to the development of high-resolution imaging systems to study both collective and microscopic phenomena in ultracold quantum gases. Such systems include both bosonic [99, 100] and fermionic [101, 102] quantum gas microscopes that exhibit single atom sensitivity and enable studies of quantum magnetism [103], atomic correlations [104], and other exotic states [105]. In this chapter, a similar high-resolution system is presented that enables the study of atomtronic circuit elements.

The organization of this chapter is as follows: First, the atom-light interaction that enables one to image and optically manipulate atoms is derived in Section 4.1. Building upon these results, Section 4.2 discusses absorption imaging, the primary technique for observing our atomtronic systems. Optical trapping and its application to the atomtronic transistor system are then described in Section 4.3. Finally, Section 4.4 introduces the high-resolution microscope system, and the remaining sections characterize the microscope system's ability to simultaneous project optical patterns onto and image the trapped atoms.

4.1 Atom-light interactions in neutral atoms

The interaction between atoms, e.g. ^{87}Rb, and an applied light field can be understood according to the classical treatment of a two level atom with a single resonant frequency, ω_0.

In the presence of a light field, the electron distribution of the atom is driven harmonically about its nucleus leading to a charge displacement governed by the equation of motion,

$$m_e\ddot{x} + m_e\gamma\dot{x} + m_e\omega_0^2 x = -e\mathcal{E}, \tag{4.1}$$

where $\mathcal{E}$ is the electric field of the light wave, γ is the classical damping rate, and m_e and e are the mass and charge of the electron, respectively [106]. For an electric field of the form $\mathcal{E}(t) = \mathcal{E}_0\mathrm{Re}\{\exp(i\omega_l t - \phi_l)\}$, solutions to Equation (4.1) are given by

$$x(t) = X\mathrm{Re}\{\exp(i\omega_l t - \phi_e)\}. \tag{4.2}$$

Here, X and ϕ_e are the amplitude and phase of the charge displacement, whereas $\mathcal{E}$ and ϕ_l are the amplitude and phase of the light field, with frequency ω_l. Solving for X, one finds

$$X = -\frac{e\mathcal{E}}{m_e}\frac{1}{\omega_0^2 - \omega_l^2 - i\gamma\omega_l}, \tag{4.3}$$

which can then be used to determine the induced polarization of the atom, $p = -eX$. The polarization can also be expressed as $p = \alpha\mathcal{E}$, where α is the complex atomic polarizability,

$$\alpha = \frac{e^2}{m_e}\frac{1}{\omega_0^2 - \omega_l^2 - i\gamma\omega_l}. \tag{4.4}$$

Within X and α, the classical damping rate describes the radiative energy loss as the charge distribution oscillates,

$$\gamma = \frac{e^2\omega^2}{6\pi\epsilon_0 m_e c^3}, \tag{4.5}$$

where ϵ_0 is the permittivity of free space and c is the speed of light in vacuum [107]. Replacing $6\pi\epsilon_0 c^3\gamma/\omega_l^2 = e^2/m_e$ and inserting the on-resonance damping rate $\Gamma = (\omega_0/\omega_l)^2\gamma$, the complex atomic polarizability becomes

$$\alpha = \frac{6\pi\epsilon_0 c^3}{\omega_0^2}\frac{\Gamma}{\omega_0^2 - \omega_l^2 - i(\omega_l^3/\omega_0^3)\Gamma}. \tag{4.6}$$

In the case of the two-level atom, Γ is equivalent to the natural linewidth of the transition and is inversely related to the lifetime of the excited state. The following sections show

that the complex polarizability dictates both the refractive index and absorption coefficient of a cloud of atoms. These two properties of the atom cloud are integral to experimental techniques such as imaging and optical trapping.

4.1.1 Refractive index, absorption, and scattering rate of atoms in a light field

Building upon the classical treatment for the response of a two level atom to an optical field, the refractive index of an atomic ensemble with density n is determined by $n_{ref} = \sqrt{1 + 4\pi n\alpha}$ [108]. By re-expressing the complex polarizability as

$$\alpha = \frac{3\epsilon_0\lambda_l^2}{(2\pi)^2}\left(\frac{i}{1+\delta^2+s_0} - \frac{\delta}{1+\delta^2+s_0}\right), \tag{4.7}$$

it is possible to separate the real and imaginary parts of α corresponding to the phase shift and absorption of light by the atom, respectively [109]. Here, $\lambda_l = 2\pi c/\omega_l$ is the wavelength of the optical field. The polarizability is seen to depend on two parameters of the field: the saturation parameter, $s_0 = I/I_{sat}$, where $I_{sat} = \hbar\omega_0^3\Gamma/12\pi c^2$, is the saturation intensity, and the normalized detuning, $\delta = \Delta/(\Gamma/2)$, where the detuning, $\Delta = \omega_l - \omega_0$, is a measure of the frequency difference between the light field and the resonant frequency of the two level atom [108]. Therefore, both δ and s_0 dictate the strength of the atom-light interaction. It follows that the refractive index of the atoms is

$$n_{ref} = 1 + \frac{\sigma_0 n\lambda_l}{4\pi}\left(\frac{i}{1+\delta^2+s_0} - \frac{\delta}{1+\delta^2+s_0}\right), \tag{4.8}$$

so long as $n_{ref} - 1 \ll 1$ [108]. As the light field propagates through the cloud of atoms, the real and imaginary parts of the refractive index cause the field to accumulate additional optical phase and lose amplitude due to photon absorption, respectively. The resulting phase shift is calculated by integrating the contribution to the spatially varying refractive index

due to the atoms along the propagation direction of the optical field ($\hat{z}$),

$$\begin{aligned} \phi(x,y) &= \frac{2\pi}{\lambda_l}\int_{-\infty}^{\infty} dz\ (n_{ref}(x,y,z)-1), \\ &= -\frac{\sigma_0\tilde{n}}{2}\frac{\delta}{1+\delta^2+s_0}, \end{aligned} \tag{4.9}$$

where $\sigma_0 = 3\lambda_l^2/(2\pi)$ is the on-resonance scattering cross-section and $\tilde{n}$ is the column density along the path of the optical beam [108]. The transmission of the light field through the cloud is calculated in a similar manner, by considering the attenuation of the beam as it propagates through the cloud, under the modified Beer-Lambert law,

$$dI/dz = -\frac{n\sigma_0}{1+\delta^2+s_0}I_i, \tag{4.10}$$

where I_i is the intensity of the incident optical field. The transmission coefficient,

$$\begin{aligned} t(x,y) &= \sqrt{I_f/I_i} = \exp\left[-\sigma_0\int_{-\infty}^{\infty} dz\ \frac{nI_i}{1+\delta^2+s_0}\right], \\ &= \exp\left[-\frac{\sigma_0\tilde{n}}{2}\frac{1}{1+\delta^2+s_0}\right], \end{aligned} \tag{4.11}$$

then relates the transmitted intensity, I_f, to the intensity incident on the cloud. Therefore, the phase shift scales linearly with the column density, while the transmission decays exponentially [108].

The modifications to the light field described by Equations (4.9) and (4.11) treat only the transmitted field. However, as alluded to previously, atoms absorb photons from the light field and subsequently re-emit them. These photons are emitted isotropically into 4π steradians. The rate of emission, or scattering rate,

$$\Gamma_{sc} = \frac{\Gamma}{2}\frac{s_0}{1+\delta^2+s_0}, \tag{4.12}$$

has a Lorentzian line shape and depends on both the intensity and detuning of the light field as well as the natural line width of the atomic transition [110].

4.2 Imaging methods in the atomtronics experiment

Perhaps one of the most important aspects of cold and ultracold atom experimentation is the extraction of information regarding the state of the atomic system. Common optical imaging techniques include phase-contrast, absorption, and fluorescence imaging. The governing relations of these methods were derived in the previous section (Equations (4.9), (4.11), and (4.12), respectively). The goal of this section is to provide an in-depth treatment of the absorption imaging technique used throughout the atomtronics experiments. Within this treatment, the use and utility of weak and strongly saturating probe beams are discussed.

Absorption imaging of ^{87}Rb atoms is performed by illuminating the atomic ensemble of interest with light resonant to the $5S_{1/2} \rightarrow 5P_{3/2}$ cycling transition, between the $|F = 2\rangle \rightarrow |F' = 3\rangle$ hyperfine states. Typically, a resonant probe beam with $I_p \ll I_{sat}$ is used to maximize the atom's sensitivity to the probe light. The transmitted light is then recorded using a lens system that images the shadow of the atoms onto the sensor of a camera. However, if sufficiently optically thick, the cloud may reduce the light transmission to levels below the dynamic range of the camera's sensor, resulting in the loss of information. Inspection of Equation (4.11) reveals two avenues to side-step this issue, without the use of more exotic, non-optical imaging techniques, such as scanning electron microscopy [111]. The solution lies in either detuning the probe field from resonance, thus increasing δ, or saturating the optical transition with an intense probe field to increase s_0.

By detuning the beam from resonance, the atoms behave like a spatially varying refractive index, see Equation (4.9), which results in lensing of the probe field. The effective refraction angle is $\sim 2\lambda_l\phi_0/\pi d$ for a cloud with diameter d and peak phase shift ϕ_0 [108]. If the refractive angle is greater than the NA of the imaging system, the refracted portion of the probe field is lost, resulting in a false absorption signal [112, 113]. In order to avoid false signals, one can instead saturate the optical transition with an intense probe field. This

method is discussed further in Section 4.2.2 and was used to image trapped atoms in the experimental work presented in Chapter 5.

4.2.1 Weak absorption imaging of atomic ensembles in free expansion

Absorption imaging techniques are widely used throughout the AMO community to image and extract quantitative information regarding atomic ensembles. As a result, the absorption imaging methods are well documented [42, 108, 114, 115, 116]. When imaging with a weak probe, $I_p \ll I_{sat}$, it is necessary to release the atoms from the trap and allow them to expand freely for a period of time, t_{TOF}, a method often referred to as time-of-flight (TOF) imaging. The typical absorption imaging sequence consists of three images: the first captures the probe beam and shadow due to the atoms ($I_{p,a}$), the second contains only the probe beam (I_p), and a final background shot (I_d) after the probe beam has been extinguished. While this last 'dark' image is not strictly necessary, it captures dark counts inherent to the camera sensor and residual scattered light in the absence of the probe beam. Since the beam propagates along the $\hat{z}$-direction, the intensity patterns are 2D images, e.g. $I_p(x, y)$. The optical depth is then calculated according to

$$OD(x, y) = \ln\left(\frac{I_p - I_d}{I_{p,a} - I_d}\right), \tag{4.13}$$

which reflects the exponential relationship between the transmission of the probe beam and the column density ($\tilde{n}\sigma_0 = OD$). From the measured OD, the atom number can then be calculated using

$$N = \frac{A_{pix}}{\sigma_0} \sum_x \sum_y OD(x, y), \tag{4.14}$$

where A_{pix} is the area per pixel and σ_0 the on-resonance scattering cross section. The on-resonance scattering cross section depends on the polarization of the probe field and is given by $\sigma_{0,\pi} = 1.938 \times 10^{-9}$ cm^2 or $\sigma_{0,\sigma} = 2.907 \times 10^{-9}$ cm^2 for π- and σ-polarized light, respectively [110].

The beauty of imaging after a period of free expansion is that the momentum distribution of the cloud is translated into the spatial degrees of freedom similar to a far-field Fourier transform, assuming t_{TOF} is sufficiently long. In fact, one of the most stark signatures of the BEC phase transition in TOF images, the emergence of a bimodal spatial distribution in which the narrow momentum spread of the condensate sprouts from the surrounding thermal distribution of the non-condensate atoms. Once the two components are distinguishable, it is possible to extract the thermodynamic variables of the atomic ensemble from the spatial variation in $OD(x, y)$.

Using knowledge of the harmonic trap frequencies of the final confining potential, ω_i, the corresponding temperature along trap axis i is given by

$$T_i = \frac{m}{2k_B}\left(\frac{\sigma_i^2\omega_i^2}{1+\omega_i^2 t_{TOF}^2}\right), \tag{4.15}$$

and can be extracted from the spatial distribution of thermal atoms by fitting to the Gaussian distribution given by Equation (2.15) [108]. If a BEC is present, the thermal atoms only occupy the 'wings' of the distribution, and it becomes necessary to only fit the part of the atomic distribution in which the condensate is absent [108, 115]. When imaging atoms that were released from a highly asymmetric trap ($\omega_\perp \gg \omega_\parallel$), it is not uncommon for temperature measurements along the two axes to disagree. In this case, the corrected temperature can be calculated according to $T \approx 2\tau_x^2/(1+3\tau_x^2)T_y + (1+\tau_x^2)/(1+3\tau_x^2)T_x$, where $\tau_i = \omega_i t_{TOF}$ [117].

At temperatures below T_c, under the TF approximation the chemical potential

$$\mu_i = \frac{m}{2}\left(\frac{R_i^2\omega_i^2}{1+\omega_i^2 t_{TOF}^2}\right), \tag{4.16}$$

is extracted by fitting an inverted parabola, given by Equation (2.24) with half width R_i, to the portion of the OD profile that contains the condensate [108]. Fits to the cloud can be improved by using a Bose-enhanced Gaussian fit that accounts for effects due to the Bosonic nature of the atoms [118]. These methods were used extensively to analyze the evolution of the atomic ensemble trapped in both the battery reservoir and transistor source well, which are discussed in Chapter 5.

4.2.2 Strongly saturated absorption imaging of trapped atomic ensembles

Whereas imaging after a sufficiently long t_{TOF} ensures the density of the cloud is within the dynamic range of the sensor, the density of trapped atoms can be $\sim 10 - 100\times$ greater. At such large densities it is necessary to operate with probe powers $I_p \gg I_s$, in order to reduce the absorption enough to completely probe the trapped ensemble,. When the probe transition is saturated, Equation (4.13) is no longer accurate. Following the work of G. Reinaudi *et al.* in Reference [114], the corrected OD profile is given by

$$OD(x,y)_{sat} = \ln\left(\frac{\tilde{I}_p}{\tilde{I}_{p,a}}\right) + \frac{\tilde{I}_p - \tilde{I}_{p,a}}{I_{sat}}, \tag{4.17}$$

and the ($\tilde{}$) indicates that I_d has been subtracted from a respective image. Equation (4.17) accounts for the saturating of the atomic transition and the reduction in the on-resonance scattering cross section. The effective scattering cross section,

$$\sigma_{eff} = \frac{\sigma_0}{1 + s_0}, \tag{4.18}$$

indicates that the saturated absorption imaging technique enables one to probe clouds with densities that are a factor of $(1 + s_0)$ larger than with a weak probe field.

The method for extracting thermodynamic quantities from in-trap atomic distributions is similar to that of the weak probe. Given knowledge of the trapping potential, both the temperature and chemical potential can be extracted using the relations for the spatial density profiles of the thermal and condensed components, respectively, that were derived in Chapter 2. In the instance that the in-trap spatial profile allows the differentiation of n_c and n_{th}, the chemical potential is determined by fitting to Equation (2.24), and subsequently the temperature is extracted by fitting to Equation (2.18) using the fugacity calculated with the fit value for the TF chemical potential. Data extraction from images of trapped atoms in atomtronic systems is discussed further in Chapter 5.

4.3 Optical trapping

The treatment of the atom-light interaction from Section 4.1 can also be applied towards optical trapping techniques. This section presents the optical dipole potential experienced by an atom within a light beam that is detuned from resonance. In conjunction with the magnetic potential generated by the atom chip, optical potentials are implemented in the atomtronics experiments to realize repulsive barriers according to the transistor system studied in Section 2.2

Like magnetic trapping, optical trapping techniques have been studied extensively and are well understood [107]. Whereas the magnetic potential originates from the magnetic dipole moment, the optical potential is the result of the induced polarization, $p = \alpha\mathcal{E}$, that was derived in Section 4.1. Therefore, the atom can be treated as a polarized medium in an electric field and is subject to the interaction potential $\propto \langle p\mathcal{E}\rangle$,

$$U_{dip} = \frac{-\mathrm{Re}(\alpha)}{2\epsilon_0 c} I. \tag{4.19}$$

Here, the intensity $I = 2\epsilon_0 c|\mathcal{E}|^2$ is obtained by time averaging the electric field, and α is the familiar value from Equation (4.6). As discussed previously, the imaginary part of the polarizability is responsible for the absorption of photons. In the context of optical trapping, $\mathrm{Im}(\alpha)$ results in heating of the atoms and is discussed in the next section. By re-expressing the real part of the polarizability as

$$\mathrm{Re}(\alpha) = \frac{3\pi\epsilon_0 c^3}{\omega_0^3}\left(\frac{\Gamma}{\omega_0 - \omega_l} + \frac{\Gamma}{\omega_0 + \omega_l}\right), \tag{4.20}$$

and assuming that the detuning of the drive field is small compared to ω_0, the second term in the parenthesis can be eliminated by taking the rotating wave approximation [119]. In doing so, the optical dipole potential experienced by ground state atoms simplifies to

$$U_{dip} = \frac{3\pi c^2}{2\omega_0^3}\frac{\Gamma}{\Delta} I, \tag{4.21}$$

and has spatial dependence dictated by the intensity pattern, $I = I(x, y, z)$. In the semi-classical treatment of the optical dipole potential, the energy shift is referred to as the AC

Stark shift, and atoms in the ground and excited states experience shifts of the opposite magnitude [107].

In the case of multi-level atoms, the two-state approximation is no longer accurate. Due to the fine-structure splitting of the electronic p-orbital, one must account for both the D1 and D2 transitions of ^{87}Rb atoms between $5S_{1/2} \rightarrow 5P_{1/2}$ and $5P_{3/2}$ states at $\omega_1 = 2\pi c/(795\text{ nm})$ and $\omega_2 = 2\pi c/(780\text{ nm})$, respectively. In the case that the detuning is comparable to the difference in D1 and D2 transition frequencies, the relative detunings from both transitions must be considered, and the dipole potential becomes

$$U_{dip} = \frac{\pi c^2}{2\omega_0^3}\Gamma\left(\frac{2}{\Delta_2} + \frac{1}{\Delta_1}\right) I, \tag{4.22}$$

where $\Delta_{1,2}$ are the respective detunings. Within the limit $\Delta \gg \Delta_{1,2}$, Equation (4.21) becomes a valid approximation.

From the relation for the dipole potential, one can see that the sign of the detuning determines whether the potential is attractive or repulsive, i.e., blue-detuned light is repulsive while red-detuned is attractive. Therefore, when designing an optical potential, Δ is a crucial parameter. Section 4.3.2 provides further discussion regarding the application of the optical dipole potential towards the generation of repulsive barriers.

4.3.1 Heating in optical dipole traps

Whereas the magnetic potential from Section 3.1 is strictly conservative, the atom-light interaction includes an imaginary component that results in a finite scattering rate (see Equation (4.12)). Due to the inherent momentum transfer in this scattering process, the atom gains an energy proportional to the recoil temperature, $T_{rec.} = (\hbar k_l)^2/2m$, where $k_l = 2\pi/\lambda_l$ is the wavenumber of the laser light. In the context of optical trapping in a detuned light field, the scattering rate is determined in a similar fashion to the dipole

potential in Equation (4.22), yielding

$$\begin{aligned}\Gamma_{sc} &= \frac{-\mathrm{Im}(\alpha)}{\hbar\epsilon_0 c} I, \\ &= \frac{\pi c^2}{2\hbar\omega_0^3}\Gamma^2\left(\frac{2}{\Delta_2^2}+\frac{1}{\Delta_1^2}\right) I. \end{aligned} \tag{4.23}$$

In terms of scaling, it is useful to note that the scattering rate is related to the dipole potential by $\Gamma_{sc} = U_{dip} \times \Gamma/\hbar\Delta$ [107].

In order to determine the heating rate of a trapped atomic ensemble, first consider the total mean energy of the atoms, which can be expressed as $\bar{E} = (3/2)k_B T(1+\beta)$. Here, the factor $\beta \equiv \bar{E}_{pot}/\bar{E}_{kin}$ dictates the penetration of the atomic wavefunction into the optical field. For example, a slowly varying harmonic potential has $\beta = 1$, while a steep walled box potential has $\beta = 0$. Using the relations for $\bar{E}$, T_{rec}, and Γ_{sc}, the heating rate is given by [107]

$$\dot{T} = \frac{2/3}{1+\beta} T_{rec} \bar{\Gamma}_{sc}. \tag{4.24}$$

Here, $\bar{\Gamma}_{sc}$ is the mean scattering rate experienced by the atoms,

$$\bar{\Gamma}_{sc} = \frac{\Gamma}{\hbar\Delta}\left(|U_{dip,0}| + \frac{3\beta}{2}k_B T\right), \tag{4.25}$$

and depends on the maximum potential (height or depth), $U_{dip,0}$, as well as the temperature of the ensemble. Equations (4.24) and (4.25) can then be used to determine the heating rate in both red- and blue-detuned traps:

$$\dot{T}_{red} = \frac{2/3}{1+\beta} T_{rec} \frac{\Gamma}{\hbar}\left|\frac{U_{dip,0}}{\Delta}\right|, \tag{4.26}$$

$$\dot{T}_{blue} = \frac{\beta}{1+\beta} T_{rec} \frac{\Gamma}{\hbar\Delta} k_B T. \tag{4.27}$$

From this set of equations, it is clear that steep, box-like potentials result in larger (smaller) heating rates for red- (blue-)detuned traps.

4.3.2 Blue-detuned optical barriers

The semiclassical treatment of the atomtronic transistor presented in Section 2.2 does not specify or depend on the shape of the repulsive barriers, so long as they provide a potential

barrier with heights V_{GS} or V_{GD} and impede atom currents due to quantum tunneling. The most straight forward barriers to realize experimentally are anisotropic Gaussian beams with a spatially dependent intensity,

$$I = I(x, y, z) = \frac{2P}{\pi \mathrm{w}_x(z)\mathrm{w}_y(z)} \mathrm{e}^{-2(x/\mathrm{w}_x(z))^2 - 2(y/\mathrm{w}_y(z))^2}, \tag{4.28}$$

where $\mathrm{w}_{x,y}(z)$ are the beam waists along the $\hat{x}$- and $\hat{y}$-directions, and the beam propagates along the $\hat{z}$-direction. Highly asymmetric optical fields that are thin along the loose, longitudinal magnetic trap axis and wide along the tight, radial trap axis are used to generate the barriers for the triple-well transistor structure. This ensures that atoms cannot skirt around the barriers, and that atom currents obey Equations (2.33). The waist defines how quickly the beam diverges as a function of the distance along z from the focus, given by

$$\mathrm{w}_i(z) = \mathrm{w}_{0,i} \sqrt{1 + \left(\frac{z}{z_{R,i}} \right)^2}, \tag{4.29}$$

where $\mathrm{w}_{0,i}$ are the barrier waists at the focus, and $z_{R,i} = \pi \mathrm{w}_{0,i}^2 / \lambda_l$ is the Rayleigh range along the i-th direction [120]. Therefore, the tighter the focus, the faster the beam diverges as it propagates away from the focal plane. For the beam to serve as a constant height potential across the radial width of the magnetic trap, the decrease in beam intensity due to its divergence must occur over longer length scales than the increase in the magnetic trap magnitude. One final point of interest relates back to the heating rate given by Equation (4.27). If the optical barrier waist along the longitudinal trap axis is sufficiently small, i.e., the intensity increases rapidly compared to the thermal width of the atoms in the magnetic trap, then the barrier appears to be a step function and the heating due to light scattering becomes negligible, as $\beta \to 0$.

4.4 A high-resolution microscope system for imaging trapped atoms and projecting optical potentials

The microscope system used for all atomtronics experiments, is schematically illustrated in Figure 4.1.[1] Consisting entirely of commercially available components, due to the transparent regions of the atom chip, the imaging and projection system achieves high numerical aperture performance without the need for custom *in vacuo* optics. The use of an infinity-corrected objective lens and a beam splitter allow for simultaneous in-trap absorption imaging and the projection of optical potentials. Detailed descriptions of individual components are provided in sections 4.4.1 and 4.4.2. The entire microscope system, including the camera and optics, are mounted on a precision XYZ translation state (Z Stage: Newport MVN80, XY Stage: Optosigma 123-0400) that is used to position the microscope relative to the atoms in the vacuum chamber.

At the heart of the microscope system is the primary objective. The NA of the primary objective dictates the feature sizes resolved by both imaging and projection beam paths. Throughout the experimental work contained in this dissertation, a 0.6 NA Zeiss LD Plan Neofluar 40× objective was used. This off-the-shelf biological microscope objective was selected for its high-resolution performance and integrated adjustment collar that corrects for variable thickness coverslips. This second feature is crucial, as it allows for the compensation of spherical aberration introduced by the finite thickness and refractive index of the chip window.

4.4.1 Through-chip imaging

Atoms confined in the magnetic potential generated by the atom chip are imaged using either fluorescence or absorption imaging techniques. The probe beam path for these two methods are illustrated in Figure 4.2. The fluorescence imaging probe is incident on

[1] The work presented in the following sections is partially published in Reference [84] and represents the first demonstration of through-chip imaging and projection of optical potentials.

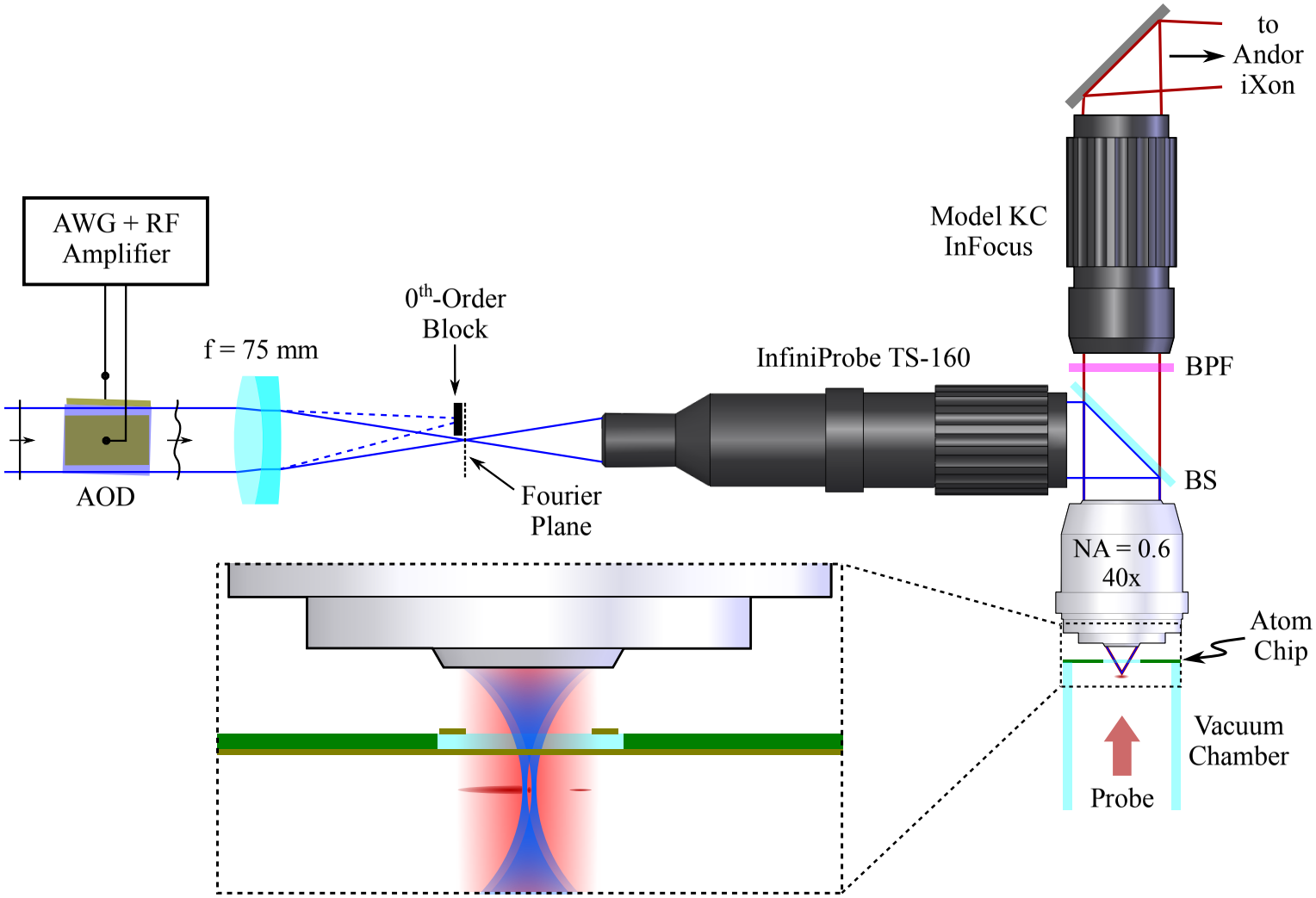

Figure 4.1: Simplified schematic of the optical system used to conduct atomtronics experiments. Imaging and projection beam paths are distinguished by red and blue marginal rays, respectively. The expanded region around the atom chip shows the projected optical potential and in-trap absorption imaging probe light as they pass through the plane of the atoms (dark red spatial distribution). System components and their respective functionality are described in the text.

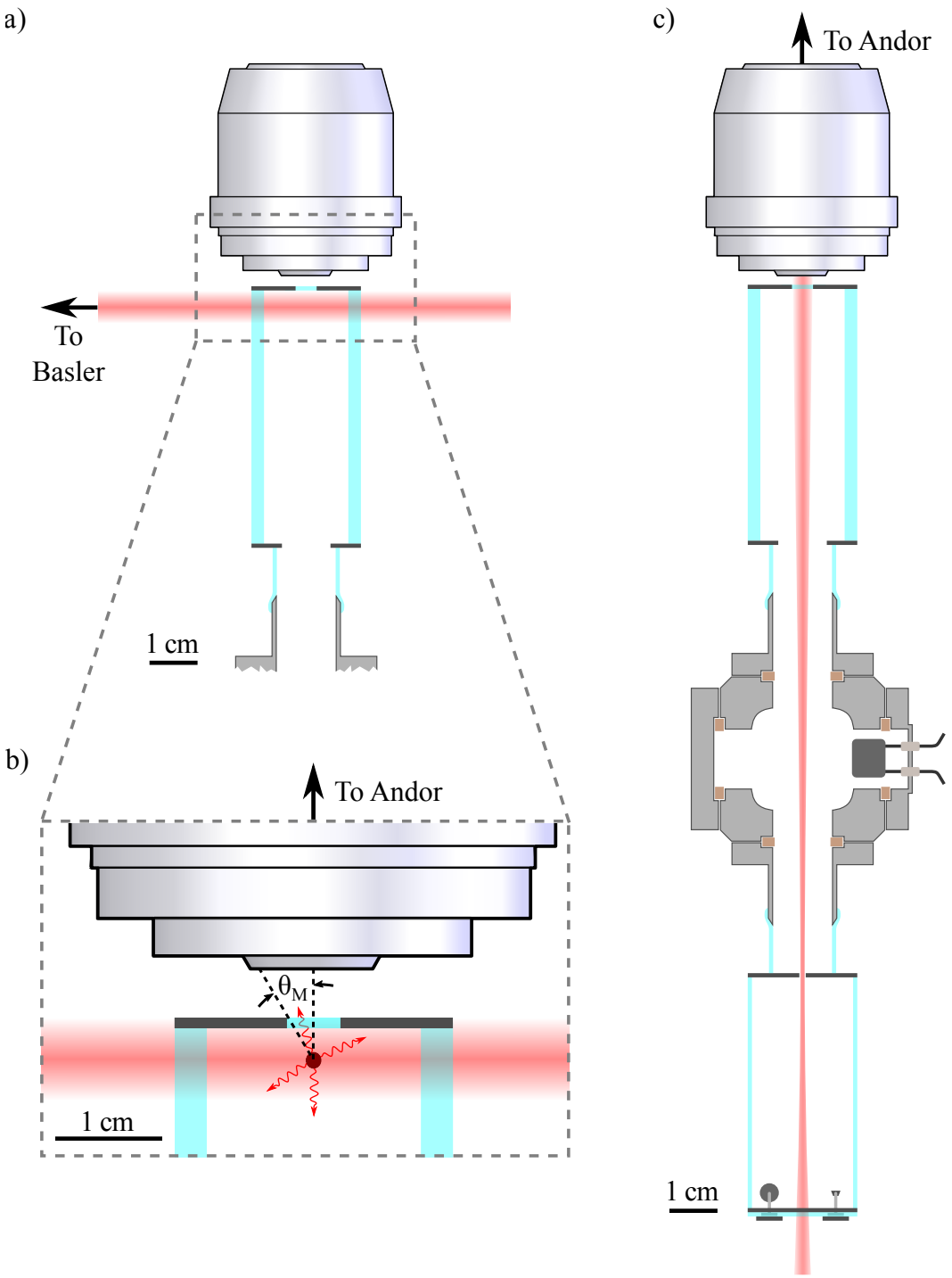

Figure 4.2: a) Schematic of the fluorescence imaging probe beam path (also used for TOF absorption imaging, with a Basler scA1400 - 17fm CCD camera). b) An expanded view of the cell, chip, and microscope objective during the fluorescence imaging process that illustrates the collection of scattered photons. Assuming proper atom chip design, discussed in Section 3.2.2, the marginal ray half-angle (θ_M) of the imaging system is dictated by the NA of the primary objective. c) Schematic of the in-trap absorption imaging probe beam path in the double MOT cell. The beam is focused through the pinhole separating the 2D and 3D MOT chambers.

the atoms from the side, parallel to the surface of the atom chip, such that the scattered photons are imaged by the microscope system rather than the probe light. By contrast, the absorption probe beam is oriented vertically in order to image the shadow of the atoms. In both configurations, light is collected by the Zeiss objective and passes through one port of an AR coated, 50:50 plate beam splitter (Edmund Optics; 45-853) that connects the imaging and projection beam paths. The transmitted light is then imaged onto an Andor iXon 897E-#BV electron multiplying charge-coupled device (EMCCD) by an Infinity Photo-Optical Model KC InFocus lens system. The resolution limit is given by the Rayleigh criterion,

$$d_{min} = \frac{0.61\lambda_l}{\mathrm{NA}}, \tag{4.30}$$

where λ is the probe light wavelength. Therefore, the 0.6 NA lens has a minimum resolvable distance between features of 793 nm. Through-chip optical resolution was tested using a 1951 USAF hi-resolution target (Edmund Optics; 58-198) that includes features as small as 780 nm. With the correction collar set to 0.42 μm, i.e., the thickness of the chip, diffraction limited optical performance is achieved. Coupled with the Andor, which has square pixels, 16 μm on a side, the 40$\times$ magnification Zeiss objective followed by the unity magnification Model KC InFocus lens system results in an object-space pixel size of 0.4 μm.

Fluorescence collection efficiency

Early in the development of the microscope system, fluorescence imaging was used to image atoms in the chip trap. To acquire a fluorescence image, a resonant probe beam is flashed on at a set intensity for a time τ_p, during which photons are scattered isotropically at a rate according to Equation (4.12). The ratio of the solid angle subtended by the primary objective, Ω, to the photon emission solid angle, $\Omega_{max} = 4\pi$ steradian, is

$$\Omega_R \equiv \frac{\Omega}{\Omega_{max}} = \frac{1 - \cos(\theta_M)}{2}, \tag{4.31}$$

where θ_M is the marginal ray angle of the primary objective. For the 0.6 NA objective, $\theta_M = \arcsin(0.6)$, and $\Omega_R = 0.1$; thus, the Zeiss objective collects only 10% of the total

scattered light. The collected light is then subject to losses in the imaging system itself. These include 85% transmission through the Zeiss objective at 780 nm, 50% transmission through the beam splitter, the 99% transmission of the Model KC lens tube, and 80% quantum efficiency of the Andor. Overall, the fluorescence imaging process is $\sim 3.4\%$ efficient. To improve the signal to noise of the images, the Andor EMCCD is cooled to $-70°$C to reduce dark counts, and the electron multiplying gain setting is set such that several photoelectrons are generated per photon incident on the sensor [121].

Assuming the net efficiency of the optical system is fixed, the next best way to increase the signal is to scatter more photons by increasing the probe pulse duration. However, despite the tight radial confinement of the magnetic chip trap, the recoil imparted to the atoms by each photon results in a random walk and a root-mean-square (RMS) displacement,

$$r_{rms} = \sqrt{\frac{N_P}{3}} v_{rec} \Delta t, \tag{4.32}$$

where N_P is the number of photons scattered, $v_{rec} \approx 5.88$ mm/s is the recoil velocity, and Δt is the probe duration [108, 110]. This effect is referred to as recoil blurring and poses a problem when the spatial position of atoms within the magnetic trap is of interest.

Fluorescence imaging resolution tests using trapped atoms

In order to determine the minimum resolvable feature size in the trapped atom cloud, fluorescence imaging was performed by exposing the atoms to an interfering probe beam. Two s-polarized beams were overlapped at the location of the atoms with an included half-angle of θ_I. This configuration creates a probe field with a standing wave pattern with sinusoidally varying intensity with a spatial period of of $\Lambda_I = \lambda_l / 2\sin(\theta_I)$ along the loose axis of the magnetic trap. Due to the high in-trap atomic density, the probe field was detuned by several linewidths of the optical transition, $\Gamma \approx 6$ MHz, in order to probe the entire spatial extent of the trapped ensemble. Since fluorescence imaging detects only the scattered photons, lensing of the probe beam is not a concern.

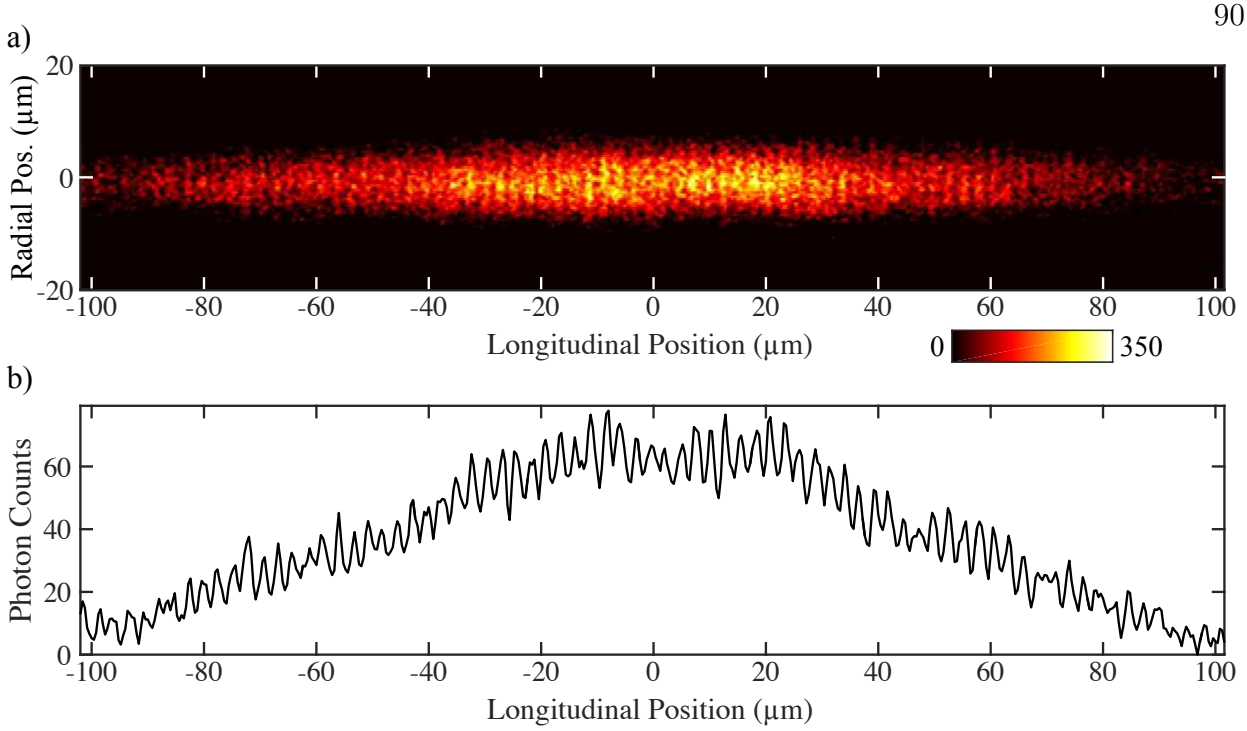

Figure 4.3: a) Superposition of 10 *in situ* fluorescence images exposed by a standing wave probe field with $\Lambda_I \approx 2.5$ μm. b) An averaged longitudinal slice of the image shown in (a) illustrates the fringe contrast.

Figure 4.3(a) shows an accumulation of 10 fluorescence images taken with a detuning of $\Delta = 4\Gamma$ and $\theta_I \approx 18°$, resulting in a fringe spacing of ≈ 2.5 μm. The fringes are clearly evident, as seen in Figure 4.3(b), which shows the longitudinal profile of the cloud obtained by averaging the 2D image along the radial axis. Fourier analysis of the spatial frequency content in Figure 4.3(a) reveals the periodicity of the probe beam imprinted on the atoms and the resulting spatial variation in the number of scattered photons. Figure 4.4 shows both 1D and 2D Fourier transforms of the accumulated image. The 1D Fourier transform along the longitudinal trap axis reveals spatial frequency content at $\pm 0.38(1)$ μm^{-1}, corresponding to a spatial period of $\Lambda = 2.63(9)$ μm. Repeating the measurement using interfering probe fields with a standing wave period nearer the resolution limit of the imaging system did not provide measurable spatial frequency content.

When imaging an extended object, the limiting factor is not the transverse, but the

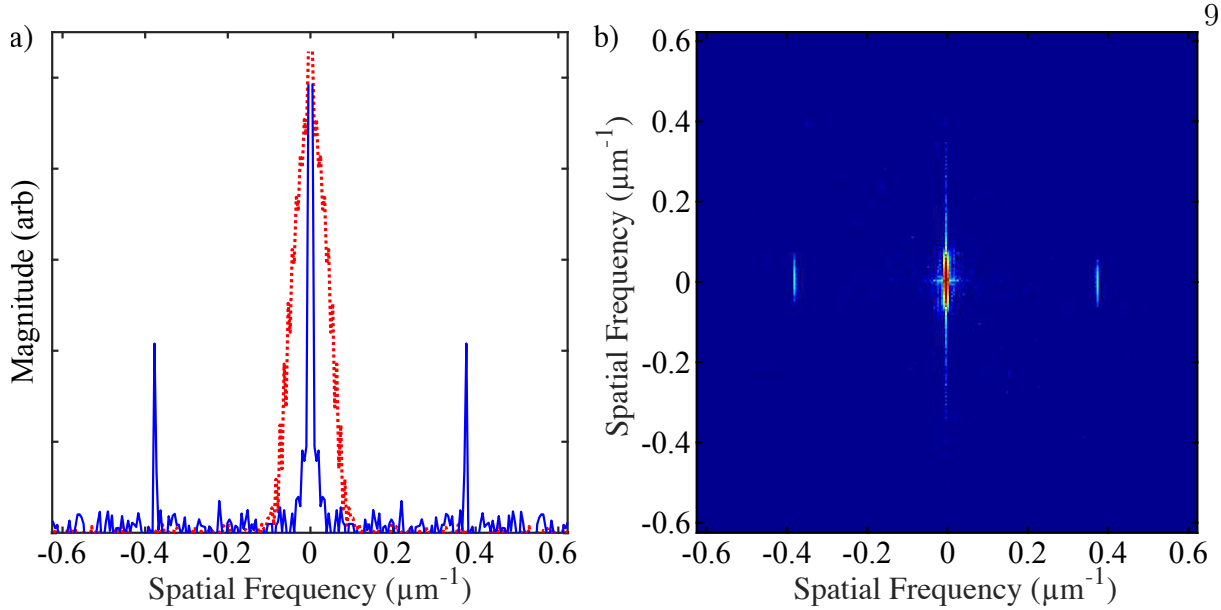

Figure 4.4: Fourier spectra of the image in Figure 4.3(a). a) Averaged 1D Fourier transforms along the longitudinal (solid, blue) and radial (dotted, red) trap dimensions. Peaks centered at ± 0.38 μm^{-1} indicate a fringe spacing of $\sim 2.63(9)$ μm. b) Corresponding 2D Fourier transform of the average image.

longitudinal resolution, i.e., the depth of field. An objective operating at a given NA has a depth of field,

$$d_{DOF} = \frac{\lambda_l}{\text{NA}^2}. \tag{4.33}$$

For the 0.6 NA Zeiss objective, $d_{DOF} = 2.17$ μm. The effect of finite depth of field is shown in Figure 4.3(b), where the fringe pattern contrast is lowest in the region where the radial extent of the cloud is largest (~ 15 μm). In this region, the contrast is $\lesssim 15\%$, which is approximately the ratio of the depth of field to the cloud thickness.

In order to improve the resolving power in the cloud using fluorescence imaging techniques, it is necessary to either lower the NA of the primary objective or reduce the cloud thickness along the imaging direction. Lowering the NA of the objective is unfavorable, as both the collection efficiency and transverse resolving power suffer. The finite extent of the cloud in the image is the product of two factors: trap frequency, which determines the initial radial extent of the cloud, and recoil blurring. The first factor can be improved by increasing

the radial frequency of the magnetic trap; however, this leads to increased trap heating. The second factor can be improved by reducing the average distance an atom is displaced as a result of scattering multiple photons. Ultimately, fluorescence imaging was abandoned in favor of absorption imaging. The two methods are compared in the following section.

Comparison of *in situ* absorption and fluorescence imaging techniques

Absorption imaging is attractive due to the large number of photons collected by the detector relative to fluorescence imaging since the probe beam is imaged directly, as shown in Figure 4.2(c). In conjunction with a saturating probe intensity, τ_p can be made significantly shorter, without suffering a loss of signal. By comparison to the fluorescence imaging sequence, absorption imaging is more complex. In order to ensure I_p and $I_{p,a}$ contain the same probe beam, i.e., displacement in structure on the probe beam is minimized, the Andor is operated in fast kinetics mode and only a portion of the EMCCD exposed to the probe light. Andor iXon 897 cameras come stock with an EMCCD array that is 512×1024 pixels, with an opaque mask shielding half of the array for storage purposes. The camera reads out pixels from the active array at 10 MHz with 0.9 μs shift time per row. Therefore, in order to readout the entire 512×512 active array into the storage array, the minimum time between exposures is ~ 27 ms. This is far too long of a time between exposures and results in unwanted fringing across the absorption image due to shifting interference patterns caused by vibrations within the system. To reduce the time between shots, two thirds of the active detector region are masked off and the Andor is run in fast kinetics mode. The minimum time between shots is ultimately limited by the vertical shift speed, which for 170 rows is ~ 170 μs. With this time delay, interference effects are reduced below the level of other noise sources. As in fluorescence imaging, the Andor EMCCD is cooled to -70°C to reduce dark counts, but the electron multiplying gain is reduced such that a single photon generates a single photoelectron, where the sensor has the highest signal to noise, as the probe beam contains many more photons.

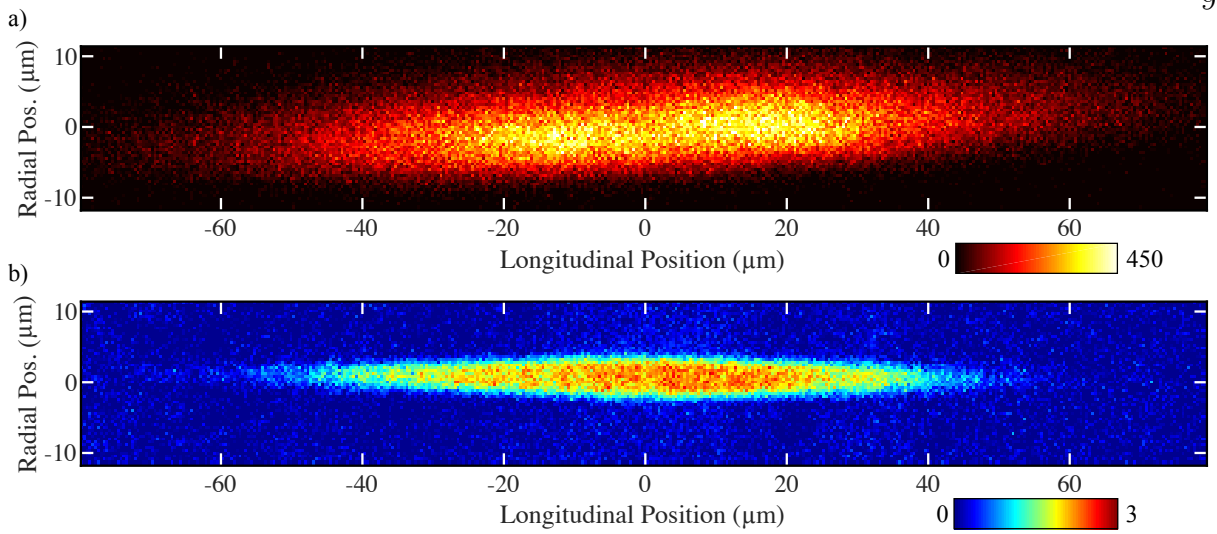

Figure 4.5: a) Accumulation of 20 fluorescence images acquired using a 20 μs pulse of 4Γ detuned probe light. b) Accumulation of three absorption images with 6 μs pulses and resonant probe light. Atomic ensembles were prepared under identical circumstances in both (a) and (b), and were imaged with probe light below the saturation intensity.

To combat the issue of recoil blur, the AOM that is used to quickly shutter the probe beam is triggered using a circuit that generates a train of TTL pulses. This enables probe pulses shorter than the minimum TTL pulse of 20 μs of the control system DAC. Pulses as short as 1.4 μs are possible, but little cloud size variation is detected below the typical probe pulse time of $4-6$ μs. Figure 4.5 illustrates the substantial difference in the recorded atomic distribution between fluorescence and absorption imaging techniques. The ability to image the in-trap spatial distribution of atoms is an integral part of data collection in the atomtronics experiments described in Chapter 5.

4.4.2 Optical potential projection system

The projection system can be broken into two decoupled sub systems, one that generates the desired optical pattern and another that images the optical pattern and projects the optical field onto the atoms with a given magnification. Figure 4.6 illustrates the two systems used to generate repulsive optical potentials. The InfiniProbe TS-160 lens system, also

from Infinity Photo-Optical, is integrated into the microscope system. The remaining optics are mounted on a precision XYZ translation stage identical to the one that positions the microscope system. Optical systems used to generate static and dynamic optical potentials are discussed in the sections that follow.

Initial alignment of the optical potential is straightforward, owing to the integration of the imaging and projection optical system. First, the microscope is positioned to image one of the wires on the vacuum side of the atom chip near the center of the window. With the wire in focus, the projection system XYZ stage is used to center and focus the projected optical potential in the field of view, using the video mode of the Andor. The magnification of the projected optical pattern is controlled via the adjustment collar on the InfiniProbe TS-160 and its working distance, which is set by the position of the 75 mm achromat. Information regarding the magnification of the InfiniProbe is available in its data sheet. Finally, the projection and microscope system translation stages are both displaced the necessary distance to move the microscope system to the plane of the trapped atoms.

Static optical potential generation

The first projection experiments conducted in the apparatus consisted of the generation of an array of asymmetric beams, like those described in Section 4.3.2, to split a trapped BEC into multiple wells. Upwards of 100 mW of blue detuned, 760 nm light is derived from a Topical DLX110 external cavity diode laser. The light is spatially filtered by an optical fiber and coupled into the optical system shown in Figure 4.6(a), which was used to generate five repulsive optical barriers spaced evenly along the longitudinal axis of the atom chip trap. A 5× cylindrical telescope elongates the initial 1.5 mm diameter beam along the radial extent of the atoms, while a transmission grating creates multiple diffracted orders. The diffraction pattern is shown in the inset of Figure 4.6(a).

A 75 mm achromatic doublet lens Fourier transforms the output of the transmission grating to generate the desired optical potential pattern at the front focal plane of an Infinity

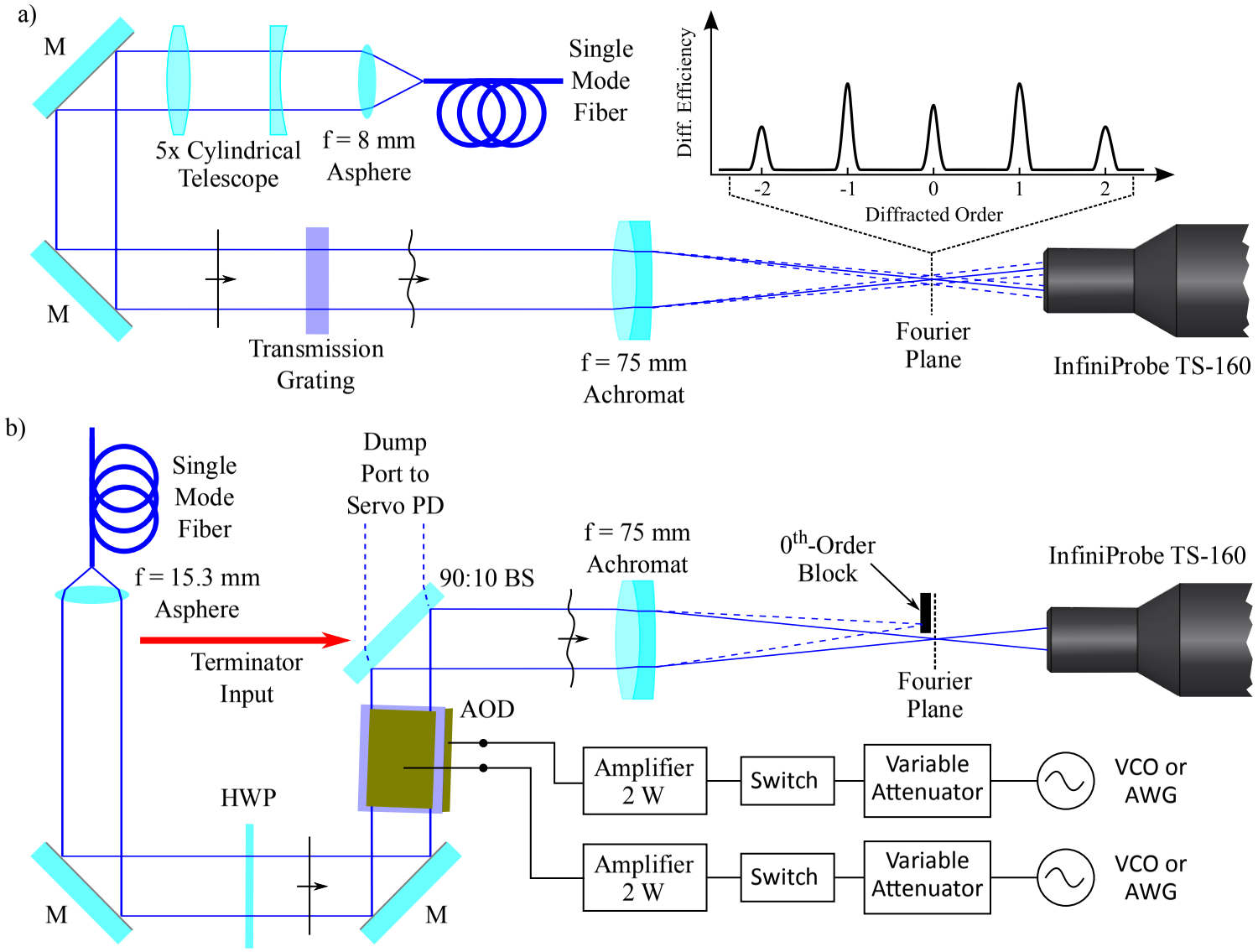

Figure 4.6: a) Diagram of the optical system used to create multiple static potential barriers. b) Optical system used in atomtronic experiments that enables dynamic control of multiple optical barriers. Mirror (M), half wave plate (HWP), photo-diode (PD).

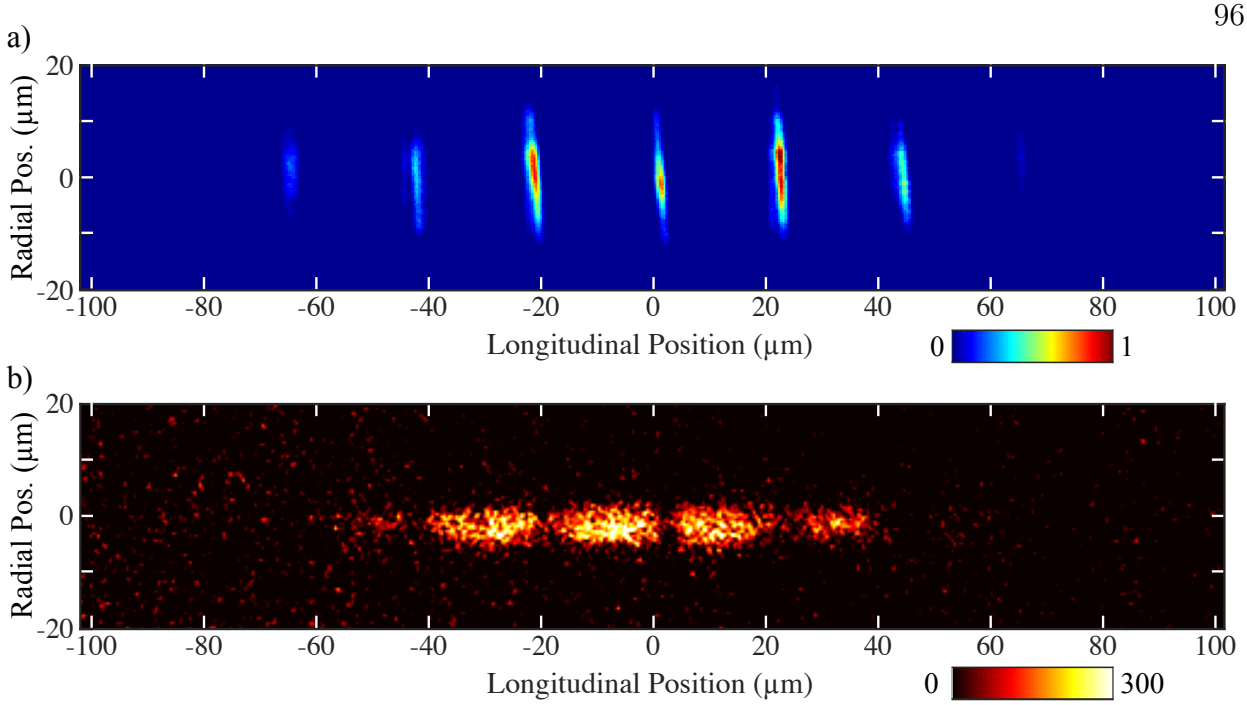

Figure 4.7: a) An array of repulsive barriers generated by a highly asymmetric Gaussian beam and a 1D transmission grating. The intensity pattern is recorded by imaging the partial reflection from the vacuum side of the atom chip window. The false color scale is normalized to the maximum intensity. b) Fluorescence image of a BEC containing $\sim 30 \times 10^3$ atoms trapped in the atom chip trap and exposed to the projected optical pattern in (1). Areas of reduced atomic density indicate the position of the repulsive barriers.

Photo-Optical InfiniProbe TS-160 lens system. The InfiniProbe images the optical pattern of the barriers through the reflected port of the 50:50 beam splitter and subsequently the barriers are projected onto the atoms by the Zeiss objective. This setup was used to demonstrate the first optical control of atoms through an atom chip [84]. Figure 4.7 shows the resulting optical potential and a fluorescence image of a BEC split into multiple clouds.

Dynamic optical potential generation

Our atomtronics experiments described in the next chapter require dynamic control of the optical potential in order to prepare the initial state of the system. Figure 4.6(b) shows a diagram of the optical system used in said experiments. As in the static potential, 760 nm light from the Topic DLX110 is spatially filtered and coupled into the optical system by

a single mode optical fiber. The shape and position of the optical barriers is controlled by the RF waveforms that drive a 2D acousto-optic deflector (AOD) from IntraAction Corp. (DTD-6010RH29). This AOD has a center frequency of 60 MHz and deflection bandwidth of 32 MHz. With an input beam diameter of 3.6 mm, the time bandwidth product of the deflector yields $\approx$ 170 resolvable spots with an access time of 5.4 μs, i.e., pattern update frequency of $\approx$ 185 kHz. Power diffracted into the +1, +1 order of the AOD forms the desired optical potential. The RF drive signals are generated by either a voltage controlled oscillator (VCO) or a two-channel arbitrary waveform generator (AWG), (Lecroy ArbStudio: 125 MHz maximum frequency, 16 bit resolution, 1 GS/sec sample rate). To generate the radial extent of the optical barrier, the AWG RF frequency is rastered about the center frequency of the AOD. The raster frequency is set to 20 kHz, which is considerably larger than the radial magnetic trap frequency such that the atoms experience the time averaged intensity of the rastered field. The longitudinal position of each barrier is then set by the frequency of two VCO outputs combined using a resistive splitter-combiner.

Chapter 5

Experimental demonstration of atomtronic devices

This chapter presents the results of two experiments that explore the behavior of atomtronic analogues to electronic circuit elements. The first is a power supply that sources an atom current to a connected load and is driven by the thermodynamic potentials of a finite-temperature BEC, namely a battery. The second experiment utilizes the battery to drive an atom current through a triple-well potential to study the steady-state behavior of the atomtronic transistor described in Section 2.2. To begin, an overview of the experimental procedure used to prepare the finite-temperature BEC that powers these atomtronic devices is provided. Section 5.2 provides a detailed description of the atomtronic battery, which is realized in a double-well potential and analyzed according to an electronic Thévenin equivalent circuit. Important experimental and numerical techniques relevant to both the battery and transistor are also introduced. Finally, experimental results are presented that validate the steady-state behavior of the triple-well atomtronic transistor system presented in Section 2.2.3.

5.1 BEC production and preparation for atomtronics experiments

Due to the standardization of vacuum chamber and atom chip technologies, BEC production is also standardized throughout the experiments in our lab and described thoroughly in the theses of previous students [10, 12, 13]. A detailed description of the early stages of the BEC production cycle that lead up to capturing atoms in the chip trap, along with

schematics for the optical, electrical, and control systems of the atomtronics apparatus can be found in the thesis of E. A. Salim [12]. The final stages including the initial process of capturing atoms on the chip, trap compression, and forced RF evaporation in the V2 window chip (see Figure 3.7) are described here.

After laser cooling the atoms to ~ 10 μK, they are optically pumped into the $|F = 2,\ m_F = 2\rangle$ state, and captured in a magnetic quadrupole trap generated by external coils. The atoms are then transferred to a location just below the atom chip window using a quadrupole ladder scheme. The initial side-guide IP trap is loaded directly from the coil generated quadrupole field by quickly shutting off the current in the external coils ($\lesssim 600$ μs) and subsequently ramping on the chip wire currents to $I_M = 3$ A and $I_H = 4.75$ A along with the necessary bias fields, $B(x, y, z) = (14, -24, 0)$ G, over 10 ms. The initial chip trap is located 230 μm below the chip and has frequencies $\omega_{load}(x, y, z) \simeq 2\pi \times (80,\ 270,\ 270)$ Hz. This method captures $\sim 20 - 30 \times 10^6$ atoms in the initial chip trap at a temperature of ~ 50 μK.

The chip trap is then compressed in order to increase the collision rate of atoms in the trap and improve the efficiency of forced RF evaporation. After a short, 50 ms RF sweep from $40 \rightarrow 28$ MHz in the initial chip trap, the wire currents are ramped to $I_M = 2.5$ A, $I_T = 0.6$ A and $I_H = 2.5$ A while simultaneously ramping the bias fields to $B(x, y, z) = (3.6, -31, 0)$ G. The resulting trap is located 130 μm below the chip and has frequencies $\omega_{evap}(x, y, z) \simeq 2\pi \times (280,\ 1500,\ 1500)$ Hz. This compression stage occurs over 400 ms, during which the RF knife is ramped from $28 \rightarrow 19$ MHz. The remainder of the evaporation cycle is completed in four stages that are ~ 300 ms long by linearly decreasing the RF knife frequency as follows: $19 \rightarrow 11 \rightarrow 7 \rightarrow 5 \rightarrow 3.8$ MHz. This scheme results in a nearly exponential decay of the RF knife frequency that allows for optimal rethermalization [122, 123]. Prior to the final RF evaporation sweep, the T-wire current is ramped to zero in order to match the longitudinal confinement of the split-guide trap (described below) and avoid excitations of the cloud. At this point in the sequence, a finite-temperature BEC has been produced with a temperature

and chemical potential that are controlled via the final RF frequency.

The procedure for loading the finite-temperature BEC into the final split-guide chip trap is much more efficient than the initial chip trap loading stage, since the side- and split-guides are well mode matched. By linearly ramping the chip wire and bias coil currents from the final evaporation trap parameters to those that generate the split-guide trap, the magnetic field is smoothly deformed into the configuration desired for the atomtronics experiments. Parameters for the split-guide trap include chip wire currents $I_G = 2$ A and $I_H = 0.5$ A along with bias fields $B(x, y, z) = (3.2, 0, -21)$ G. The resulting cigar shaped magnetic trap is located 130 μm below the chip and has trap frequencies $\omega_{expt}(x, y, z) \simeq 2\pi \times (67,\ 1500,\ 1500)$ Hz.[1] Transfer to the split-guide trap is accomplished with near-unity efficiency and little to no heating of the atoms. An image of an initial ultracold atomic ensemble was shown in Figure 4.5(b). This point in the experimental cycle serves as the initial condition for the experiments described in the remainder of this chapter.

5.2 The atomtronic battery system

Circuits, both electronic and atomtronic alike, fundamentally require a source of power to operate. Atomtronic batteries have been proposed in both open quantum systems constructed of reservoirs with different chemical potentials connected by a lattice potential [21, 24], as well as mesoscopic systems containing a finite-temperature Bose-Einstein condensate (BEC) that sources condensate atoms to the connected load [124]. The work presented in this section describes the realization and characterization of an atomtronic battery that stores energy in the form of a finite-temperature BEC and sources an atom current to a simulated load element. A schematic of the experimental system is shown in Figure 5.1.

[1] The trap frequencies of the split-guide trap used during the atomtronics experiment were measured by exciting the center of mass mode along the longitudinal or radial trap axes. The radial slosh mode is excited by modulating the z-bias coil current with a low amplitude sinusoid and measuring the temperature of atoms in the trap. The induced heating near resonance can be understood under the discussion of chip heating in Section 3.4.1. The longitudinal mode is excited by displacing the atoms with an optical barrier and measuring the harmonic center of mass motion after the barrier is removed.

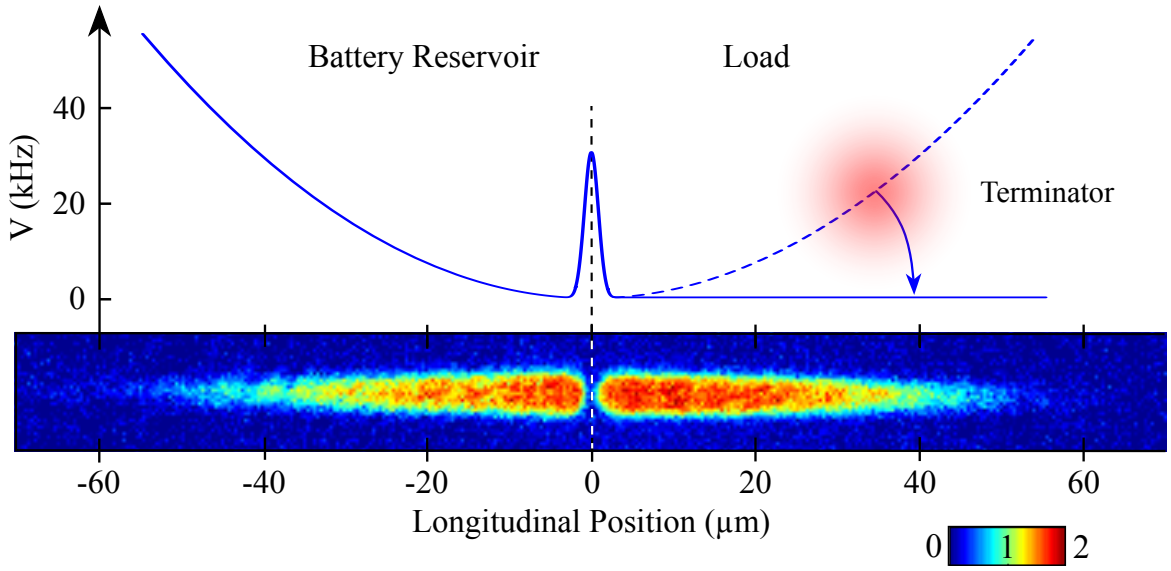

Figure 5.1: Schematic of the double-well atomtronic battery potential: The top panel shows the longitudinal potential energy landscape of the hybrid magnetic and optical potential. A resonant "terminator" beam removes atoms that flow into the load well from the system. The bottom panel shows a false color, *in situ* absorption image of atoms occupying both wells of the potential.

5.2.1 Charging the battery

The first step in realizing an atomtronic battery is loading the atomic ensemble into the reservoir well, i.e., charging the battery. To do so, the cigar shaped magnetic trap is transformed into a double-well potential. In the process, the finite-temperature BEC is compressed into one of the two wells, labeled "Battery Reservoir" in Figure 5.1. This is accomplished by ramping on a repulsive barrier, with a height $V_S = 100$ kHz $\gg k_B T$, at the edge of the longitudinal spatial extent of the cloud and sweeping it adiabatically to the center of the magnetic trap, as shown in Figure 5.2(a)-(c). When converting from temperature units to Hz, note that 1 kHz $\approx$ 50 nK. Dynamic control over the position and height of the barrier are achieved by adjusting the power and frequency of the RF signal driving the AOD described in Section 4.4.2. In this way all of the atoms are loaded into the reservoir well and the battery is considered charged. The stored energy of the battery is then characterized by the thermal and chemical potentials of the trapped atomic ensemble.

With the barrier present the reservoir well is approximated as a half-harmonic well with $\omega_{x,batt} \approx 2 \times \omega_{x,expt} = 2\pi \times 134$ Hz and a density of states that is reduced by half relative to the harmonic magnetic potential. The half-harmonic well approximation is used to determine the chemical potential in the TF limit. Under this approximation, the reservoir well chemical potential differs by $< 5\%$ from the corresponding values determined from 3D simulations of the Gross-Pitaevskii equation for a BEC in the ground state of the hybrid magnetic and optical potential. A plot of the relative error in the chemical potential versus the number of condensed atoms in the reservoir well is shown in Figure 5.3.

5.3 Impedance matching in atomtronic systems

Impedance matching is a fundamental concept in electrical system design, especially in power transmission applications. The same can be said for atomtronic systems that supply an atom current to a connected load. Some fraction of the current will be reflected

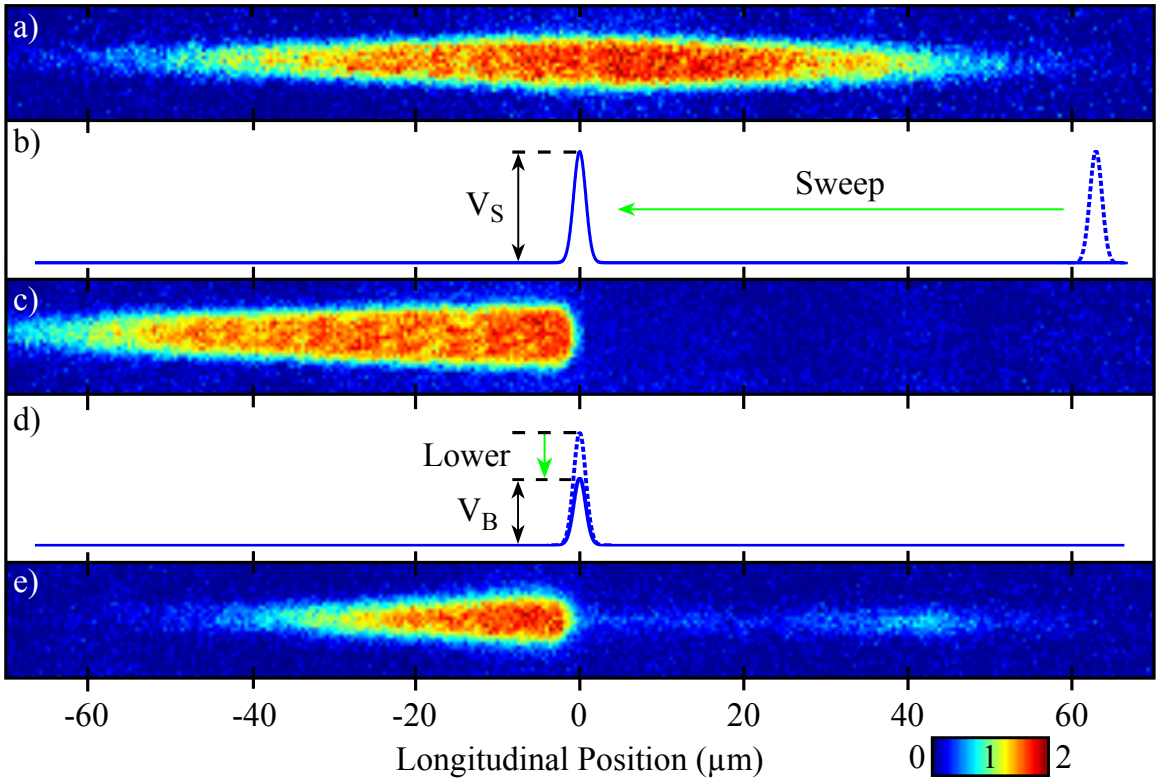

Figure 5.2: Battery charging procedure: a) Atoms begin in the split-guide magnetic trap. b) An optical barrier is turned on at the far-right extent of the atoms and swept towards the center of the magnetic trap. c) Atoms trapped in one half of the magnetic trap after the barrier is swept. d) The barrier height is the reduced to connect the battery to the load. e) Battery output after 30 ms of discharge with $V_B = 30$ kHz.

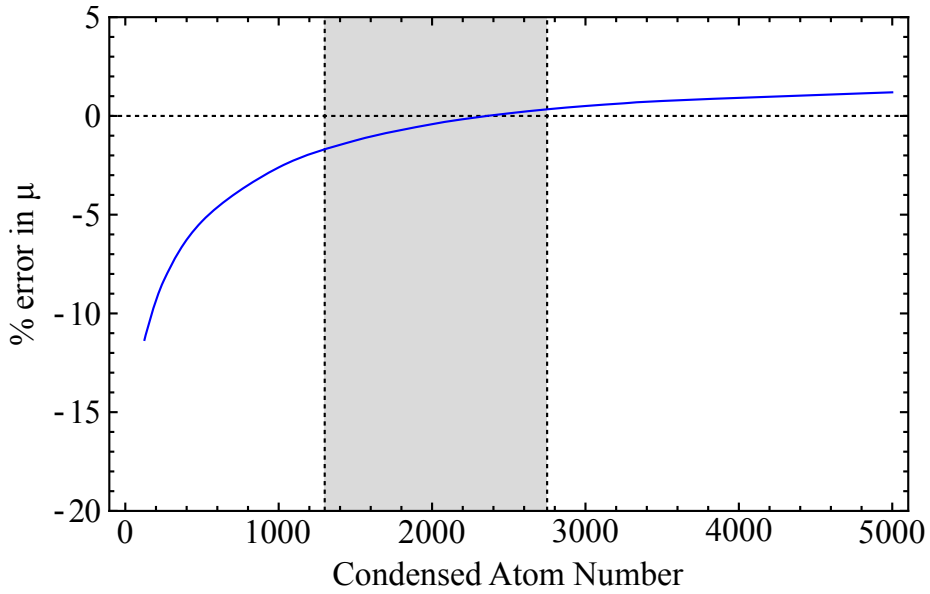

Figure 5.3: Error in the TF chemical potential in a half-harmonic well, relative to results from GPE simulations. Here the % error in μ is defined as $(1 - \mu_{TF}/\mu_{GPE}) \times 100$. The gray shaded region indicates the range of condensed atoms in the battery reservoir under typical experimental conditions.

back towards the current supply, depending on the characteristics of the load. Therefore, the input impedance of the load circuit must be matched to the output impedance of the circuit element supplying the current in order to achieve maximum power transfer. Whereas electrical impedance, $Z(\omega)$, depends on the signal frequency, the transmission spectrum of massive particles through a given potential is energy dependent, i.e., $Z(E)$ [65, 125]. Examples of Bragg-matching to a periodic potential have been experimentally studied [66, 67]. The impedance of non-trivial potentials such as the Gaussian barriers used in the battery and transistor experiments can be calculated numerically using the method of generalized impedances [65, 126].

5.3.1 An atomtronic terminator

In order to study the behavior of the atomtronic battery rather than the reflection properties of the connected potential, it is necessary to simulate an impedance matched load. Therefore, during the evolution of the atomtronic battery, the load well is illuminated with laser light (labeled "terminator" in Figure 5.1) that is tuned to atomic resonance such that any atoms reaching the load well are removed from the trap. This is accomplished by optically pumping atoms from the magnetically trapped $|F = 2,\ m_{\mathrm{F}} = 2\rangle$ state to any of the untrapped $|F = 2,\ m_{\mathrm{F}} \leq 0\rangle$ states, as shown in Figure 5.4. To illustrate the effect of the terminator beam, the harmonic potential in the load well has been flattened out in Figure 5.1, indicating that atoms entering the load region are effectively coupled to vacuum modes and escape the system. Therefore, the terminator beam serves an analogous purpose to termination in RF electronics, where proper termination impedance matches the device output to the load circuit in order to eliminate signal reflection and possible interference. Furthermore, the terminator beam introduces localized dissipation that enables the study of non-equilibrium dynamics in atomtronic systems as they evolve.

In the experimental apparatus, the terminator beam is projected along the same beam path as the optical barriers, as shown in Figure 4.6, and has a typical power of $\sim 10^{-12}$

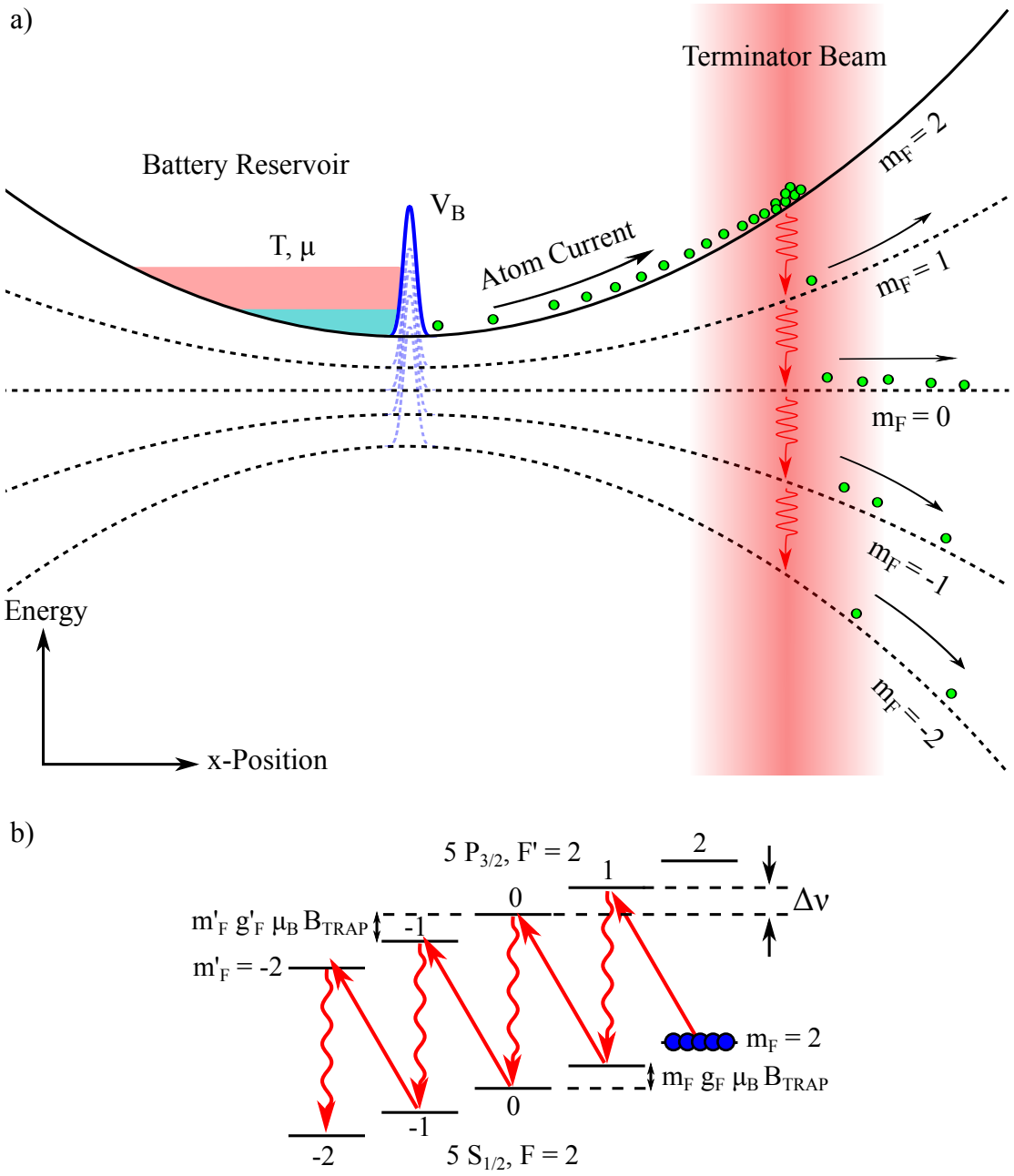

Figure 5.4: a) Schematic illustrating the role of the terminator beam. Atoms that flow into the right-hand load well of the battery system are optically pumped by the terminator beam into states that experience zero or repulsive magnetic forces and subsequently escape the trap. b) Energy level diagram illustrating the optical pumping scheme. The terminator beam is red-detuned from the $|F = 2\rangle \rightarrow |F' = 2\rangle$ optical transition by $\Delta\nu$, the average Zeeman splitting of m_F states.

W. The quantization axis for the optical transition is determined by the bias field along the $\hat{x}$-direction; therefore, the terminator beam must be aligned to have a non-zero field projection along the longitudinal trap axis. Displacing the terminator beam, which has a full width at 1/e of 16 μm, 32 μm into the load well ensures that only atoms in the load well are out-coupled.

5.4 Characterizing the atomtronic battery

The battery is characterized via observations of the atomic ensemble in the reservoir well and the emitted atom current while the battery supplies current to the load. The discharge behavior was recorded for several emission rates dictated by the height of the barrier, which is varied from $V_B = 20 - 70$ kHz, in 10 kHz increments between data sets. Throughout the following analysis the unit convention of Ref. [124] is followed, and both energies and particle currents are reported in units of Hz. Evolution of the battery reservoir is measured using both TOF and *in situ* absorption imaging techniques. Thermal, N_{th}, and condensed, N_c, atom numbers as well as the ensemble temperature are extracted from two-dimensional bimodal fits to the spatial density profile of atoms in TOF images (see Section 4.2.1).

One such dataset is presented in Figure 5.5, which shows the time evolution of the reservoir ensemble during battery discharge with $V_B = 50$ kHz. In this data set, the reservoir has an initial population of $N = 19.03(97) \times 10^3$ atoms, of which $N_c = 1170(84)$ are condensed, corresponding to chemical and thermal potentials of $\mu = 2.86(8)$ kHz and $T = 678(24)$ nK, respectively. These thermodynamic potentials provide a gradient between the reservoir and load wells that drives an initial atom current of $I = 334(22)$ kHz. As the battery reservoir discharges, it cools. After $\sim$ 30 ms a nearly constant chemical potential of $\mu = 3.86(16)$ kHz is reached and sustained for the remaining $\sim$ 50 ms. After 80 ms the thermal potential energy has decreased to $T = 440(11)$ nK, as shown in the inset of Figure 5.5, and the current to $I = 60.8(7.7)$ kHz. Battery discharge with other barrier heights exhibits similar behavior,

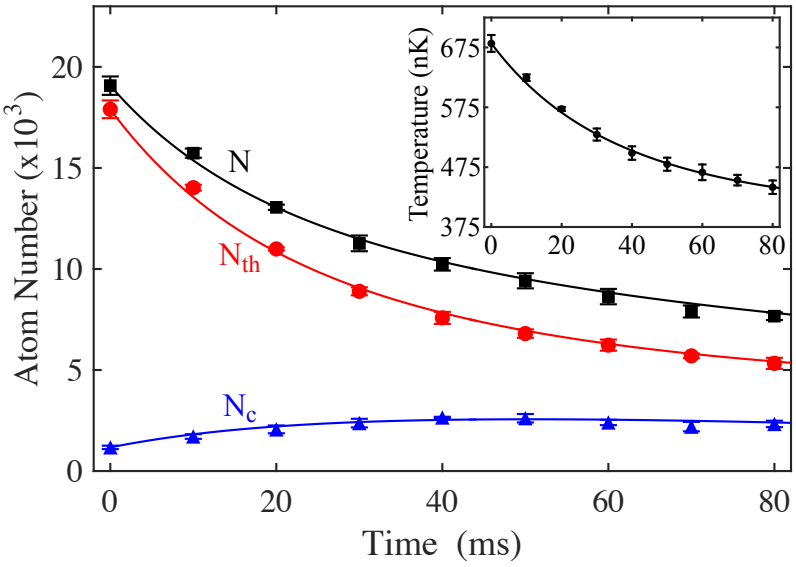

Figure 5.5: Time evolution of the total (black squares), thermal (red circles), and condensed (blue triangles) atom numbers in the reservoir for $V_B = 50$ kHz. The temperature of the reservoir ensemble is shown in the inset. Error bars represent the standard error of the mean for five experimental realizations. Solid lines show the results from numerical calculation of the reservoir population described in Section 5.4.1.

with lower values of V_B resulting in a more rapid depletion of both the reservoir atom number and temperature.

In-trap images are used to probe the spatial distribution of the atoms emitted into the load well and also to calibrate the height of the repulsive barrier. By extinguishing the terminator beam $\sim$ 4 ms prior to imaging ($\sim 1/4 \times 2\pi/\omega_{x,expt}$), atoms emitted into the load well are allowed to interact with the magnetic potential for a time equal to roughly one quarter of the longitudinal trap period. As a result, the images serve as a rudimentary spectrum analyzer, translating the displacement of atoms at their classical turning point in the load well into a measurement of their longitudinal energy. An example is shown in Figure 5.2(e). The longitudinal position and spatial distribution yield information regarding the height of the barrier and the momentum spread of atoms entering the drain well, respectively. The longitudinal momentum spread of the battery output current is determined by fitting a Gaussian to the longitudinal spatial distribution that peaks at ~ 40 μm, which corresponds to a spread in kinetic energy, ΔE. We find that $\Delta E \approx k_B T$, indicating that the current emitted into the load has an energy spread on the order of the temperature of the ensemble in the battery reservoir.

5.4.1 Modeling the battery

Presuming that the contribution to the total atom current due to tunneling is negligible, only atoms in the high energy tail of the distribution can contribute to the output current. Therefore, the system relies on thermalizing collisions to repopulate energy levels from which atoms are emitted. Given the tight radial confinement of the magnetic potential, the reservoir well is in the hydrodynamic regime along the longitudinal dimension of the trap when $\sigma \gg l$, where σ is the thermal width of the reservoir ensemble from Equation (2.15), and $l = 1/n\sigma_s$ is the mean free path between collisions [43, 127]. Under typical experimental conditions $\sigma/l \sim 100$, and the collision rate is sufficiently high for the reservoir ensemble to remain in a state of dynamical quasiequilibrium [128]. Therefore, the atomic ensemble can be described

in terms of equilibrium thermodynamic variables.

The discharge behavior of the atomtronic battery is modeled using rate equations for both the atom number and energy stored in the reservoir well:

$$\frac{dN}{dt} = -\gamma N_{th} f(\eta, \mu, T)\,, \tag{5.1}$$

$$\frac{dE}{dt} = \frac{dN}{dt}\,(\eta+\kappa)\,k_B T + \beta C, \tag{5.2}$$

which are derived from Equations (2.33) and (2.36), respectively. The magnitude of the particle current is governed by the probability that an atom has sufficient energy to traverse the barrier, $f(\eta, \mu, T)$ =1/exp$(\eta - \mu/k_B T)$, where $\eta = V_B/k_B T$ is referred to as the truncation parameter. This probability is scaled by the quantity γN_{th}, which encapsulates the rate at which the reservoir atoms encounter the barrier. Here, the collision rate, γ, is given by Equation (2.34). The energy current on the other hand is given by the product of the particle current and the average energy removed per particle given by $(\eta+\kappa)\,k_B T$. The κ-parameter indicates the average energy removed from the reservoir in excess of the barrier height energy, by each particle traversing the barrier. The value of κ is on the order of unity and depends on the dimensionality of the ensemble's momentum distribution relative to the allowed escape trajectories [53, 60]. For the potential studied here, $\kappa \sim 3$, whereas in isotropic evaporation, e.g., forced-RF evaporation, $\kappa \sim 1$ [122]. Determination of the $\kappa-$parameter is discussed further in the following section.

To account for additional heating or cooling effects external to the flow of atoms, the rate βC is included. This term does not affect the total atom number, but transfers energy to or from the reservoir ensemble according to the heat capacity, C, (see Equation (2.32)) and the total external heating or cooling rate, β. In the context of this demonstration, only heating due to technical trap noise[2] is included; however, this term could also be used to incorporate heat generation associated with irreversible processes during circuit operation [27].

[2] The heating rate due to technical noise, measured with $V_B = V_S$, increases the temperature of the reservoir ensemble by $\approx$ 80 nK over an 80 ms period.

Determining the κ-parameter

The excess energy parameter, κ, is determined from battery discharge data across a range of truncation parameters according to the relation

$$\kappa = \left(\frac{3}{2} + \delta_{3D}\right)(\alpha + 1) - \eta, \tag{5.3}$$

where $\delta_{3D} = 3/2$ for a three-dimensional harmonic oscillator [122]. Here, α represents the energy transfer efficiency,

$$\alpha = \frac{\dot{T}/T}{\dot{N}/N}. \tag{5.4}$$

The time derivatives of the temperature and number, $\dot{T}$ and $\dot{N}$, respectively, are extracted from the time evolution of the battery reservoir, shown in Figure 5.5. Values of κ for various truncation parameters are shown in Figure 5.6. Also shown are results from DSMC simulations[3] for the experimental conditions. The DSMC method is well-documented [129], and has been used to study collisions and evaporative processes in cold and ultracold atomic systems [128, 130, 131]. The horizontal and vertical positions of each point indicate $\bar{\eta}$ and $\bar{\kappa}$, the mean values of η and κ across the measured discharge time, respectively. Similarly, error bars indicate the range of η and κ values during discharge and incorporate statistical uncertainty from five experimental realizations. The horizontal dashed line at $\kappa = 2.9$ reflects the result of molecular-dynamics simulations reported in Reference [60]. As the truncation parameter is decreased, the κ-parameter determined from experimental data decreases to ~ 2.34 at $\bar{\eta} = 1.77$, following the trend of the DSMC results. The drop in κ at lower η reflects the increased coupling between the transverse modes of the reservoir well and the load, allowing less energetic atoms to traverse the barrier. Therefore, decreasing the barrier height increases the magnitude of the current, but each emitted particle possesses less energy in excess of V_B. The interplay between the magnitude of the current and κ plays a determining role in the power output of the battery, which is described in Section 5.4.2.

[3] Simulations of the κ-parameter were performed with code developed following References [129] and [130].

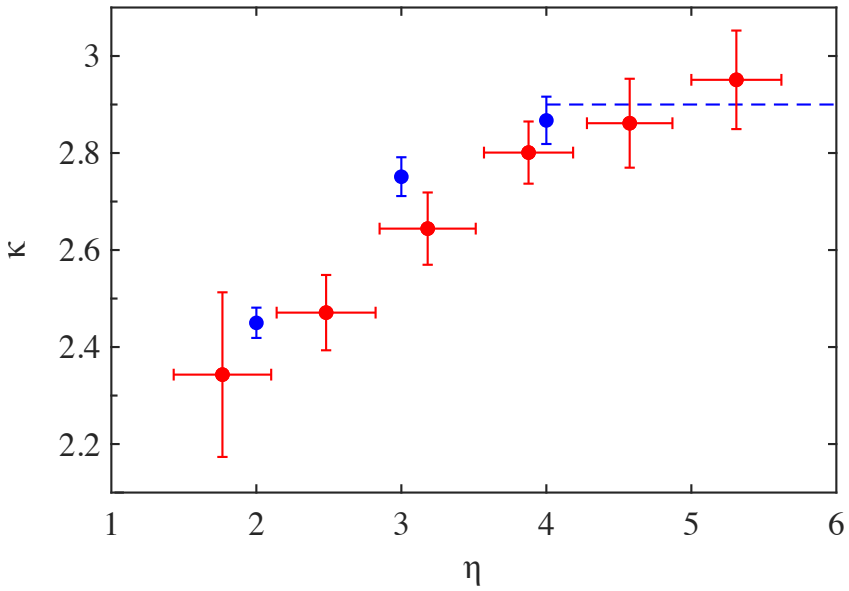

Figure 5.6: Comparison of the κ-parameter from experiment (red circles) and DSMC simulation results (blue circle). Horizontal and vertical error bars on the red points represent the standard deviation of η and κ during the time evolution of each experimental data set, respectively, while the points indicate the mean values, $\bar{\eta}$ and $\bar{\kappa}$. Results from DSMC simulations are compiled from 50 ms of evolution time during which κ is determined for each test particle that traverses the barrier. The data points and error bars at $\eta = 2,\ 3$, and 4 indicate the mean value and standard deviation of κ obtained by averaging over all emitted test particles. The horizontal, dashed blue line indicates the results of molecular-dynamics simulations reported in Reference [60].

Testing the validity of the rate equation model

To compare the battery rate equation model to experimental data, Equations (5.1) and (5.2) are integrated numerically using the fourth-order Runge-Kutta (RK4) method (see Reference [132]) in which parameters of the ensemble (e.g. N, E, and C) are updated at each time step using expressions derived in Section 2.1.3. Experimental parameters including $\bar{\kappa}$ and $\bar{\eta}$ from Figure 5.6 along with initial reservoir numbers and temperatures are used to initialize the calculation. Representative results of the numerical calculation for N, N_{th}, N_c, and T of the battery reservoir during discharge with $V_B = 50$ kHz are shown as solid lines in Figure 5.5 overlaying the experimental data. Results of the numerical calculation show agreement with the evolution of the reservoir ensemble to within the uncertainty of the experimental data. The numerically calculated state of the reservoir ensemble and output current are utilized in the analysis of the battery presented in the next section.

Thévenin equivalent circuit

The atomtronic battery is analyzed using the Thévenin equivalent circuit of a non-ideal electronic battery, shown in Figure 5.7, where equivalent elements of the two systems are labeled. Of particular interest is the role of dissipation in the atomtronic system. Dissipation in electronic devices manifests in the form of heat generated during the flow of current, i.e., Ohmic heating. Electronic batteries store energy, ε, and necessarily contain a finite internal resistance, R_{int}. When connected to a load with resistance R_L, current $I_L = \varepsilon / (R_{int} + R_L)$ flows through the combined battery/load circuit. Due to the non-zero internal resistance, power is dissipated within the battery equivalent to $P_{int} = I_L^2 R_{int}$. These relations are used to study dissipation in the atomtronic system, where μ replaces ε and dissipation in the reservoir is represented by an effective internal resistance, R_{int}.

The power dissipated within the atomtronic battery is calculated using the numerical results for the evolution of the reservoir ensemble during battery discharge. Here, power

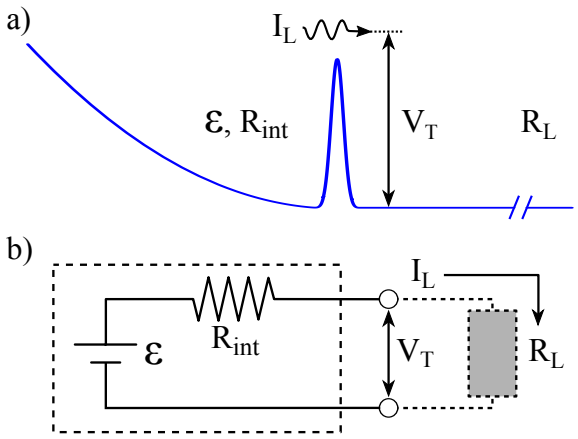

Figure 5.7: a) Diagram of the atomtronic battery potential showing elements that are conceptually equivalent to those of a non-ideal electronic battery. b) The Thévenin equivalent electronic circuit. The reservoir well contains the thermodynamic energy that is analogous to the electromotive force, ε, stored in the battery. Dissipation in the reservoir during discharge is represented by an effective internal resistance R_{int}. Current, I_L, emitted from the reservoir into the load well carries with it an average energy that is likened to the terminal voltage, V_T, of the electronic battery.

dissipated in the reservoir is equivalent to the change in internal energy of the ensemble stored in the reservoir well, given by $P_{int} = \dot{E} - \mu\dot{N}$. Therefore, the internal resistance is

$$\begin{aligned} R_{int} &= \frac{\dot{E} - \mu\dot{N}}{I_L^2} \\ &\simeq \frac{\mu - (\eta + \kappa)\, k_B T}{I_L}, \end{aligned} \tag{5.5}$$

which has units of [Hz/Hz]. In simplifying the expression for R_{int} to obtain Equation (5.5), $\dot{N}$ and $\dot{E}$ have been replaced by Equations (5.1) and (5.2), respectively, and $I_L = -\dot{N}$. Additionally, an additive factor of $\beta C/I_L^2$ has been omitted, as it is small compared to other contributions to the internal resistance. We find that the internal resistance is negative, synonymous with the observed cooling of the reservoir, and its magnitude increases in time. Figure 5.8 shows the evolution of the internal resistance as the atomtronic battery discharges for a subset of the experimental data, denoted by their mean truncation parameter, $\bar{\eta} =$ 1.77, 3.18, and 4.57. The magnitude of the internal resistance, $|R_{int}|$, increases more rapidly in time with smaller $\bar{\eta}$, but the initial value of $|R_{int}|$ is smaller. The observed increase in $|R_{int}|$ during battery discharge is indicative of an increased impedance to current flow, and is consistent with the behavior of electronic batteries.

The terminal voltage of the Thévenin equivalent circuit is given by

$$\begin{aligned} V_T &= \mu - I_L R_{int} \\ &\simeq (\eta + \kappa) k_B T, \end{aligned} \tag{5.6}$$

where Equation (5.5) has been inserted for R_{int}. Therefore, V_T is the average energy carried by each atom as it flows into the load, as in Equation (5.2). This result is intuitively satisfying as V_T represents the potential of the emitted atoms to do work on the connected load. The magnitude of V_T of the fully charged atomtronic battery depends on both the height of the barrier and the reservoir ensemble temperature, and to first order the terminal voltage evolves according to $\dot{V}_T \propto \kappa k_B \dot{T}$. The time-evolution of V_T is shown in Figure 5.9 for the same subset of $\bar{\eta}$ shown in Figure 5.8. Depletion of stored energy, accompanied by increasing

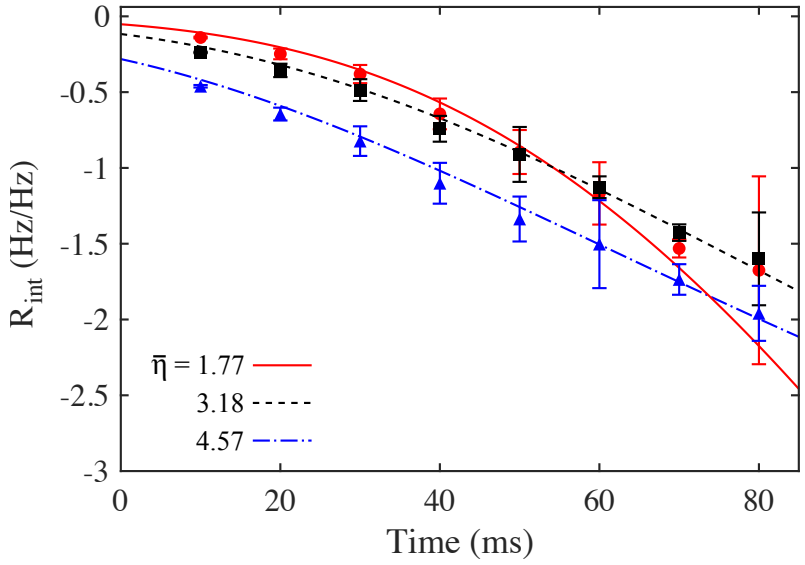

Figure 5.8: Internal resistance of the atomtronic battery during discharge calculated using Equation (5.5) for three barrier heights: $\bar{\eta} = 1.77$ (solid, red), 3.18 (dashed, black), and 4.57 (dash-dot, blue). Curves indicate results from the numerical model, while the data points show the corresponding results from experimental data for N, μ, T, and $\bar{\eta}$ along with the calculated values of $\bar{\kappa}$ and I_L. Error bars are propagated from the standard error of the mean for N, μ, and T.

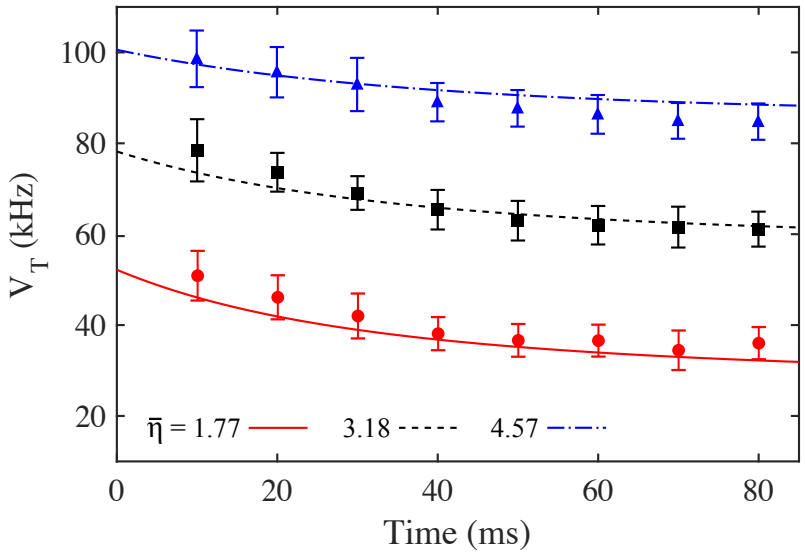

Figure 5.9: Effective terminal voltage, V_T, of the atomtronic battery during discharge for three barrier heights with mean truncation parameters: $\bar{\eta} = 1.77$ (solid, red), 3.18 (dashed, black), and 4.57 (dash-dot, blue). Data points show the corresponding results from the experimental data, calculated using Equation (5.6). Error bars are propagated from the standard error of the mean for N, μ, and T.

R_{int}, leads to a decrease in the voltage supplied by the battery. Again, this behavior is consistent with that of electronic batteries.

5.4.2 Battery performance

Performance of the atomtronic battery depends on $\bar{\eta}$, and is characterized by both the capacity of the battery and the peak power delivered to the impedance matched load.[4] Electronic battery capacity is characterized in multiple ways; however, two common metrics are the total current and total energy delivered to the load during the time it takes the terminal voltage to drop below a set depletion voltage [133]. In the atomtronic battery, the current capacity, C_c, is determined by integrating the current output from the time the barrier is lowered (from $V_S \to V_B$) until the discharge time, t_d, when V_T falls below 90% of its initial value. The calculated current capacity, which is plotted in Figure 5.10 for data sets with $\bar{\eta} \approx 1.77 - 5.28$, indicates that increasing the discharge time by an order of magnitude results in a $1.6(2)\times$ increase in C_c of the atomtronic battery. During the discharge time, shown as an inset in Figure 5.10, nearly half of the initial $\approx 20 \times 10^3$ atoms are emitted into the load. Current capacity in electronic batteries is often characterized in terms of Peukert's law, which states that battery current capacity obeys the relationship $C_c = I_L^{\rho} t_d$, where ρ is the Peukert constant [134]. An ideal battery has $\rho = 1$ while typical lead-acid electronic batteries have $\rho = 1.1 - 1.5$, and $\rho > 1$ indicates internal power loss [135]. Therefore, by increasing t_d the current capacity of a battery can be increased. Using measured values for the current and discharge time, along with the calculated current capacity, the Peukert constant of the atomtronic battery is found to be $\rho = \log(I_L)/\log(C_c t_d) = 2.1(3)$. This large value of ρ reflects the dissipation within the atomtronic battery reservoir.

The energy capacity, C_E, of the atomtronic battery is an extension of C_c, describing the total energy supplied by the battery, rather than the number of atoms. Figure 5.11

[4] Impedance matching implies that $P_L = V_T^2/R_L$, where $R_L = R_{int}$. Using the calculated values of R_{int} and V_T, the load resistance is calculated using $R_L = R_{int}/(\mu/V_T - 1)$. For all data sets we find $|R_L| = |R_{int}|$, confirming that the load well is impedance matched by the terminator beam.

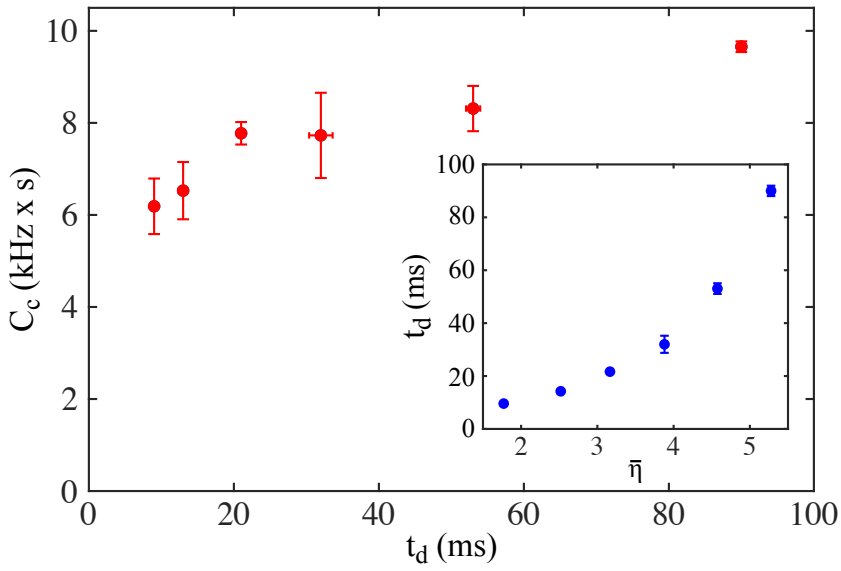

Figure 5.10: Current capacity, $C_c = \int_0^{t_d} I_L dt$, shown here in units of kHz $\times$ s, is found to increase monotonically with the discharge time, t_d, which is shown in the inset. The discharge time increases exponentially with the mean truncation parameter, which is consistent with Equation (5.2).

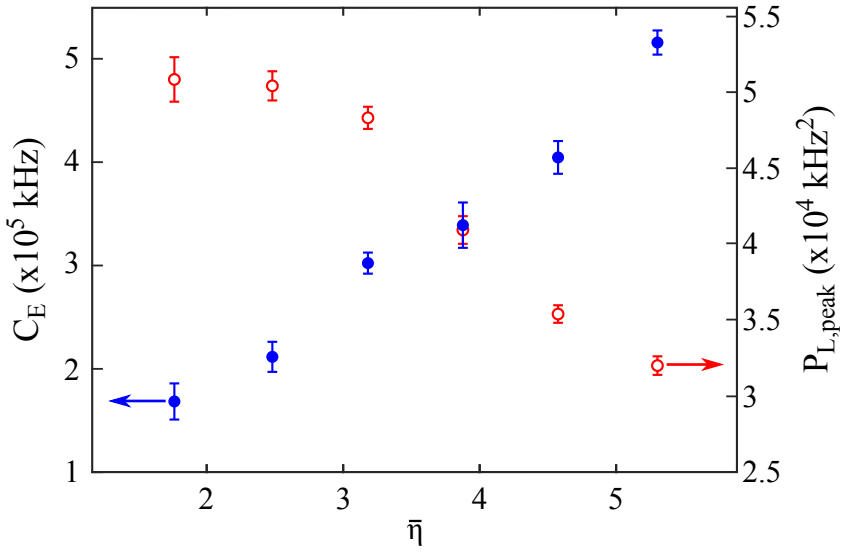

Figure 5.11: Atomtronic battery performance versus truncation parameter. Energy capacity, $C_E = \int_0^{t_d} I_L V_T dt$, (filled blue circles, left axis) increases linearly with increasing barrier height. Peak power output, $P_{L,peak}$, (open red circles, right axis) decreases monotonically with increasing barrier height. Values are determined from experimental data for N, μ, T, and $\bar{\eta}$ along with the calculated values of $\bar{\kappa}$ and I_L. Error bars are propagated from the standard error of the mean for N, μ, and T.

shows C_E, which is calculated in a similar manner to the current capacity, by integrating the power output to the load during the discharge time. Like the current capacity, the energy capacity shows an increasing trend with respect to the truncation parameter, in part due to the linearly increasing terminal voltage. Ultimately, the energy capacity is limited by the total energy of the ensemble initially stored in the reservoir, $E_{tot} = 6.5(9) \times 10^5$ kHz.

The peak power output, $P_{L,peak}$, of the atomtronic battery is determined from experimental data using the relation $P_L = I_L V_T$, and is shown in Figure 5.11. Output power of the atomtronic battery varies during the discharge time, providing a peak power immediately after reducing the barrier height to V_B. The battery is capable of supplying a maximum peak power of $P_L \approx 5 \times 10^4$ kHz^2 for $\bar{\eta} \lesssim 3$. At higher truncation parameters the peak power output declines due to the exponentially decreasing I_L, despite increasing V_T. Figure 5.11 encapsulate the performance of the atomtronic battery and illustrates that the battery can be operated in regimes of either large peak output power or large energy capacity.

5.5 An atomtronic transistor

With its behavior understood, the atomtronic battery can now be used to power other atomtronic circuit elements. Owing to the importance and ubiquity of its electronic counterpart, the device we seek to emulate is a three-terminal transistor. This is accomplished by adding a second optical barrier to the atomtronic battery system. In this configuration, the role of the battery is to maintain the chemical potential and temperature of the source well, allowing the triple-well system to be treated according to Section 2.2. In the following sections, the steady-state behavior of the atomtronic transistor[5] is explored by varying the relative height of the two barriers, which sets the feedback parameter, $\upsilon \equiv (V_{\mathrm{GD}} - V_{\mathrm{GS}})/k_B T_{\mathrm{s}}$. Measurements of the normalized temperature drop, $\tau = (T_{\mathrm{s}} - T_{\mathrm{g}})/T_{\mathrm{s}}$, and chemical potential drop, $\hat{\mu}_{\mathrm{sg}} = (\mu_{\mathrm{s}} - \mu_{\mathrm{g}})/k_B T_{\mathrm{s}}$, are compared to the analytic results of Section 2.2.3 and are found to confirm the ability to control the steady-state behavior of the atomtronic transistor

[5] The results discussed here are published in Reference [136].

via the feedback parameter.

5.5.1 The experimental triple-well system

Keeping with the nomenclature of field-effect transistors adopted in Section 2.2.1, the three regions of the experimental triple-well potential are labeled "source," "gate," and "drain." These regions are indicated in the longitudinal profile of the hybrid magnetic and optical trapping potential that is shown in the top of Figure 5.12. The two barriers are separated by 4.8 μm resulting in a gate well longitudinal trap frequency of $\omega_{x,G} \approx 2\pi \times$ 850 Hz.[6] In conjunction with the Gaussian profile of the barriers, this spacing minimizes the anharmonicity of the central well. Note that the degree of overlap between the two optical barriers contributes to an offset in the potential energy of the gate well. The shift in the minimum energy of each well due to the Gaussian shape of the barriers is denoted by $V_{i,0}$. For the data presented here, the barrier separation of 4.8 μm results in $V_{\mathrm{S},0} \approx V_{\mathrm{G},0} \approx V_{\mathrm{D},0} \approx 0$. As in the experimental characterization of the battery, the terminator beam is used to out-couple atoms that enter the drain well during transistor operation in order to observe the time dynamics of the source and gate wells.

The initial state of the transistor is prepared in a similar manner to the atomtronic battery (see Figure 5.2). By sweeping the source-gate barrier, with a height of $V_{\mathrm{S}} \approx 100$ kHz, all of the atoms are compressed into the source well before turning on the gate-drain barrier, leaving the gate and drain wells initially empty. Each experimental realization begins with a total source well atom number of $N_{\mathrm{s}} = 20.0(2) \times 10^3$ atoms, at a temperature $T_{\mathrm{s}} =$ 15.0(5) kHz, which corresponds to a TF chemical potential of $\mu_s = 3.0(2)$ kHz in the half-harmonic trap. At time $t = 0$ the barrier heights are set to the desired energies, V_{GS} and V_{GD}, and the system is allowed to evolve for a time Δt. Measurements on the state of the

[6] The longitudinal gate frequency is measured using the same method that was used to determine the radial trap frequency of the split-guide trap. By displacing the barriers slightly, and in unison, the first order longitudinal mode of the gate well is excited and the resulting heating is used to map out the excitation spectrum.

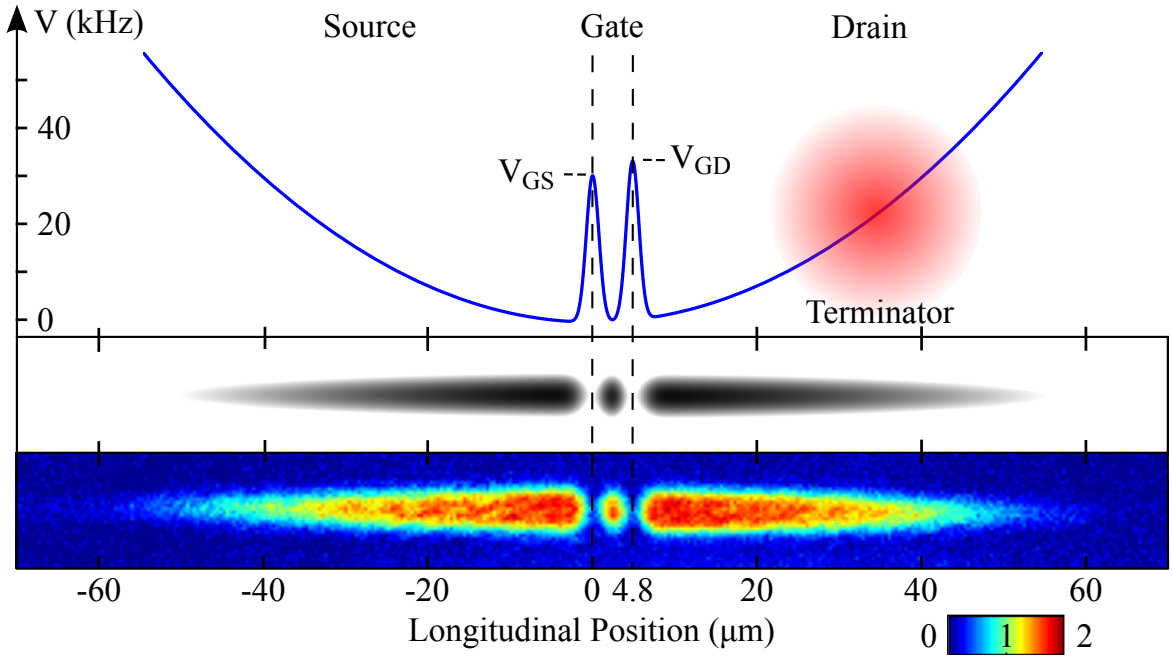

Figure 5.12: Top panel: Longitudinal potential energy profile of the hybrid magnetic and optical trap. Center panel: Calculated 2D energy contour. Bottom panel: *In situ* absorption image of approximately 4.5×10^4 ^{87}Rb atoms at $T \approx T_c$, revealing the three distinct regions of the triple-well potential

system are performed using absorption imaging techniques, either in TOF or *in situ*.

5.5.2 Transport dynamics in the atomtronic transistor

Quantitative data regarding the thermodynamic evolution of the source ensemble is extracted using TOF imaging. Figure 5.13 shows the total, N_{s}, thermal, $N_{\mathrm{th,s}}$, and condensed, $N_{\mathrm{c,s}}$, atom numbers determined from bimodal fits to the momentum distribution of the cloud in free expansion (see Section 4.2.1), for a representative data set with $V_{\mathrm{GS}} = 30$ kHz and $V_{\mathrm{GD}} = 33$ kHz. The decay of the total atom number in the source well reflects the flux of atoms emitted into the gate, and can be used to quantify the source-gate atom current, which is shown in Figure 5.14. As one might expect, the evolution of the source well mimics that of the battery reservoir. However, the magnitude of the net source-gate current is reduced due to the reverse current, I_{gs}, that flows from the gate, back into the source due to the presence of the gate-drain barrier.

Transport dynamics in the triple-well system are calculated according to the same RK4 numerical integration method that was used to model the battery evolution. The calculation is expanded to suit the transistor potential by including the three atom currents from Equation (2.33) and imposing particle and energy conservation given by Equations (2.35) and (2.36), respectfully. The steady-state solution for source and gate ensemble properties obtained via the RK4 calculation reproduces the analytical predictions for the temperature and chemical potential drops shown in Figures 2.5 and 2.6. Numerical calculations of the time evolution of the source well atom number and temperature are overlaid with the experimental data in Figure 5.13. The net source-gate current is also calculated and shown in Figure 5.14. After an initial transient period of ~ 20 ms, the numerically calculated atom numbers, temperature, and net source-gate current agree with the experimentally measured values to within the uncertainty of the data. It is suspected that the disagreement between the model and data at early evolution times is due to the initial non-equilibrium state of the gate well.

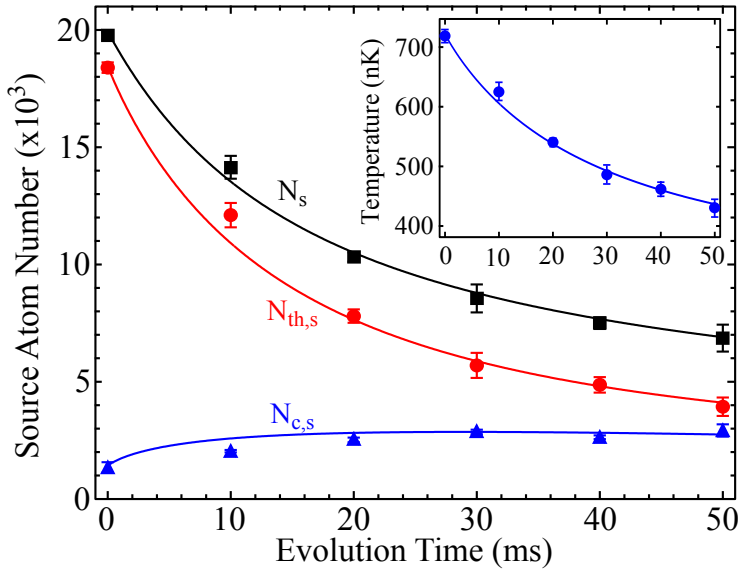

Figure 5.13: Gate well population as a function of the feedback parameter. The population is measured using a saturated probe beam intensity and undercounts the true number. Error bars represent the standard error on the mean from five experimental realizations at each feedback parameter.

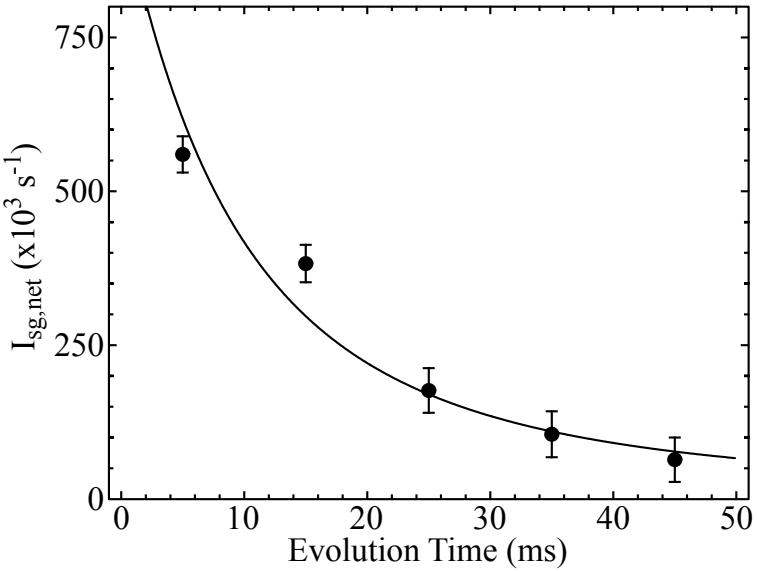

Figure 5.14: Net source-gate atom current determined from the first time derivative of the source well total atom number. Error bars indicate the error propagated from data in Figure 5.13.

Transport dynamics are further observed by probing the system *in situ*. Figure 5.15 presents a series of images showing the in-trap atomic distribution that includes the initial state, with all of the atoms contained in the source well, followed by the evolution of the system for $\Delta t = 0 - 50$ ms, during which $V_{\mathrm{GS}} = 30$ kHz and $V_{\mathrm{GD}} = 33$ kHz. This series of images was recorded using a weak probe beam ($I_{\mathrm{p}} \lesssim I_{\mathrm{sat}}$) in order to observe atoms that have reached the drain. As can be seen in the third frame of the series, atoms become trapped in the gate well by $\Delta t = 10$ ms. If atoms were not trapped in the gate, but rather only traversing it, one would expect there to be at most twice the density seen in the drain well, just to the right of the gate-drain barrier. We note that at early evolution times atoms that enter the gate well experience a region of substantial population inversion since energy states lying below the height of the barriers are initially unpopulated. While the route to steady-state is an analytically difficult problem, the role of interatomic interactions and manifestation of dissipation are made evident by the population growth in the gate well.

5.5.3 Source and gate wells in steady-state

In order to probe the steady-state behavior of the atomtronic transistor, the system must first evolve for a sufficiently long time such that the source and gate ensembles reach a quasi-steady-state. The required equilibration time is determined by measuring the gate well population as a function of time. In order to extract quantitative data from measured in-trap atomic density, the probe transition is strongly saturated, as described in Section 4.2.2. In the saturated probe regime one gains access to the high density source and gate well ensembles, but loses information regarding the atom current flowing in the drain. The evolution of the total gate well atom number, N_{g} is shown in Figure 5.16, for $\upsilon = 0.6$. Here, the atom number is calculated according to Equation (4.17). The data shows a rapid rise in the gate population, increasing to $N_{\mathrm{g}} = 1380(55)$ atoms after 20 ms, after which it settles to a value that agrees with the steady-state gate population, shown by the blue dashed line in Figure 5.16, that is calculated using the previously described RK4 method. In conjunction

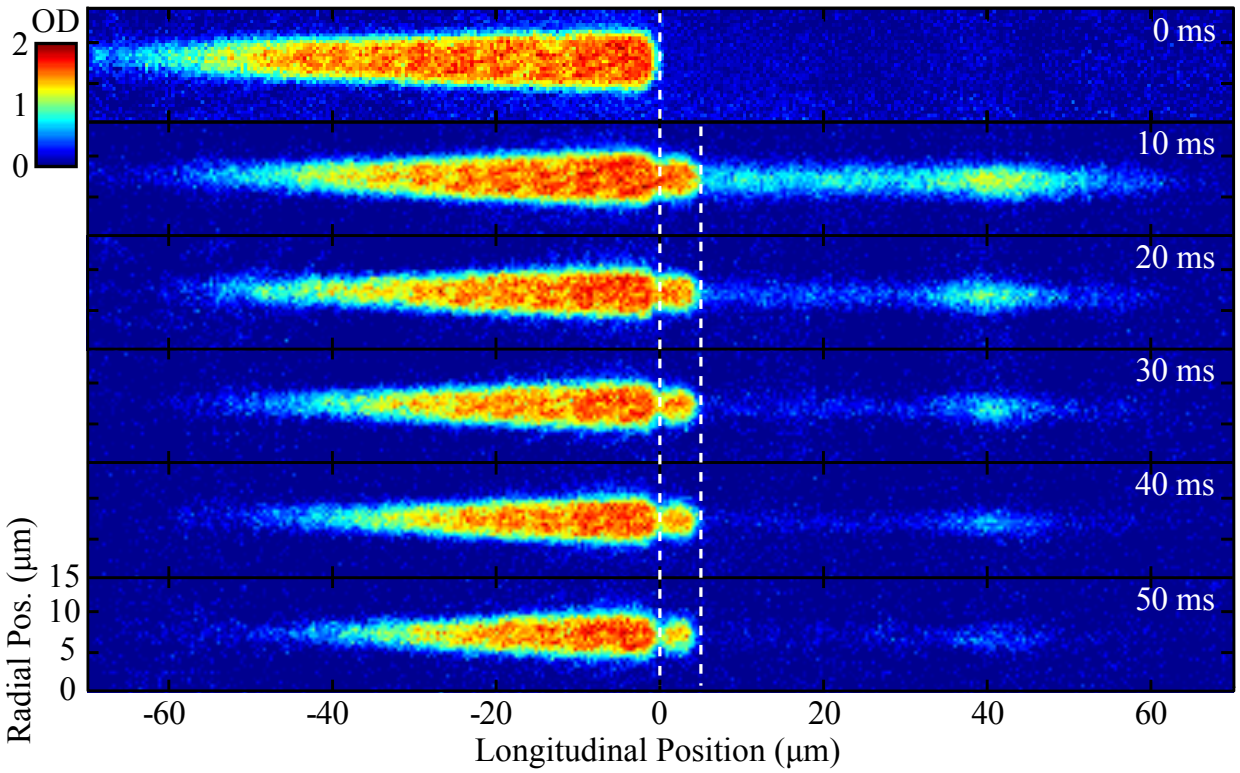

Figure 5.15: Time series of the atomtronic transistor as current flows from the source, through the gate, and into the drain. Vertical dashed lines indicated the location of the two repulsive, Gaussian barriers, here with heights of $V_{\mathrm{GS}} = 30$ kHz and $V_{\mathrm{GD}} = 33$ kHz.

with the agreement between the measured and calculated net source-gate current after ~ 20 ms, equilibration of the gate well population verifies that the system reaches a quasi-steady-state by $\Delta t = 30$ ms.

The tunability of the steady-state behavior of the atomtronic transistor is explored by measuring the in-trap atomic distribution with different feedback parameters, after an evolution time of $\Delta t = 30$ ms. Measurements are made with a gate-source barrier height fixed at $V_{\mathrm{GS}} = 30$ kHz, while the gate-drain barrier height is varied between data sets. The measured gate population is plotted in Figure 5.17 as a function of the feedback parameter. The data shows a rapid increase in the quasi-steady-state population of the gate well beginning at the feedback parameter $\upsilon \approx -0.25$. Population growth in the gate well when $V_{\mathrm{GD}} < V_{\mathrm{GS}}$ provides further evidence that dissipation occurs as atoms traverse the gate region. The source of dissipation is thought to arise due to collisions between particles entering the gate well. This hypothesis is supported by other works that study the filling rate of an initially empty well [59] and collision induced decoherence [137].

The temperatures of the source and gate well ensembles are also extracted from *in situ* images. Equation (2.15) is fit[7] to the thermal tails of the in-trap atomic density profiles along the radial trap direction to yield the characteristic widths that scale as $\sigma_i \propto \sqrt{T_i}$. The temperature drop, $\tau \equiv (T_{\mathrm{s}} - T_{\mathrm{g}})/T_{\mathrm{s}}$, is calculated from the measured values of T_{s} and T_{g} and is plotted in Figure 5.18. The data shows that $\tau > 0$ for $\upsilon \gtrsim 0$, indicating that atoms in the gate do in fact become colder than those in the source, just as was predicted in Section 2.2.3.

Experimental measurements of the steady-state gate atom number are compared to results of the RK4 numerical calculation performed for a range of feedback parameters that span those of the experimental data. The numerical results are indicated by the solid line in Figure 5.17. Deviation between the model prediction for the gate population and the

[7] Ideally one would fit the thermal distribution using Equation (2.18), which includes $g_{3/2}(z(x))$, where z(x) is given by Equation (2.28). Fits using this function were unstable and required care to ensure self-consistency of μ_i and N_i. Instead, the temperature is fit using Equation (2.15), which neglects the HF mean-field but provides a more robust, less hands-on fitting procedure.

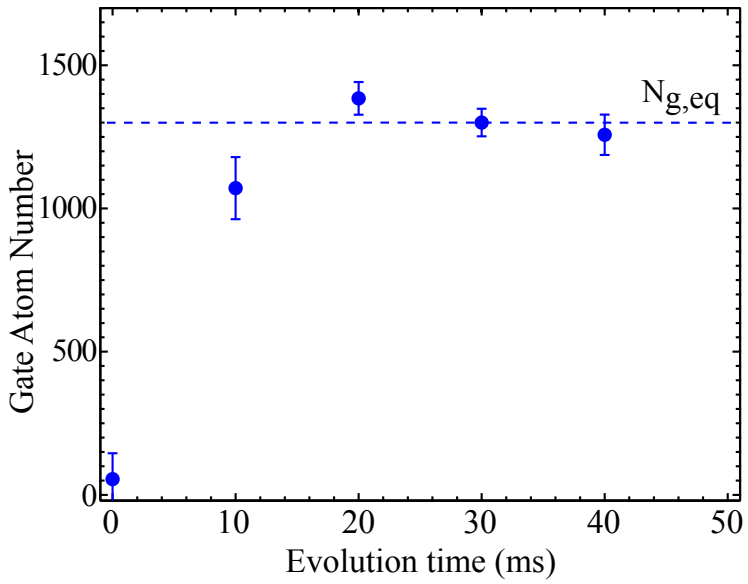

Figure 5.16: Time evolution of the measured gate well atom number versus time, relative to the calculated steady-state population, $N_{\mathrm{g,eq}}$, for $\upsilon = 0.6$. Error bars represent the standard error on the mean of three experimental realizations at each time.

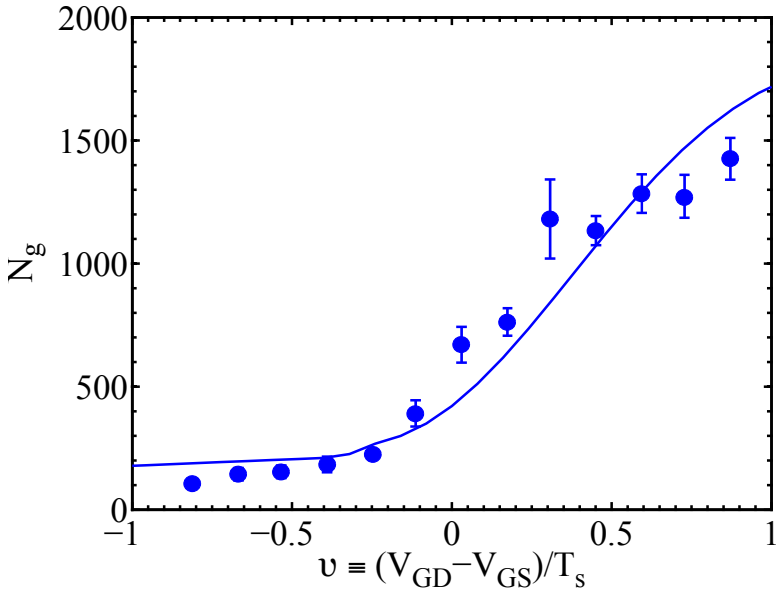

Figure 5.17: Chemical potential drop between the source and gate wells of the atomtronic transistor after an evolution time of 30 ms. Error bars represent the standard error on the mean for five experimental realizations at each feedback parameter.

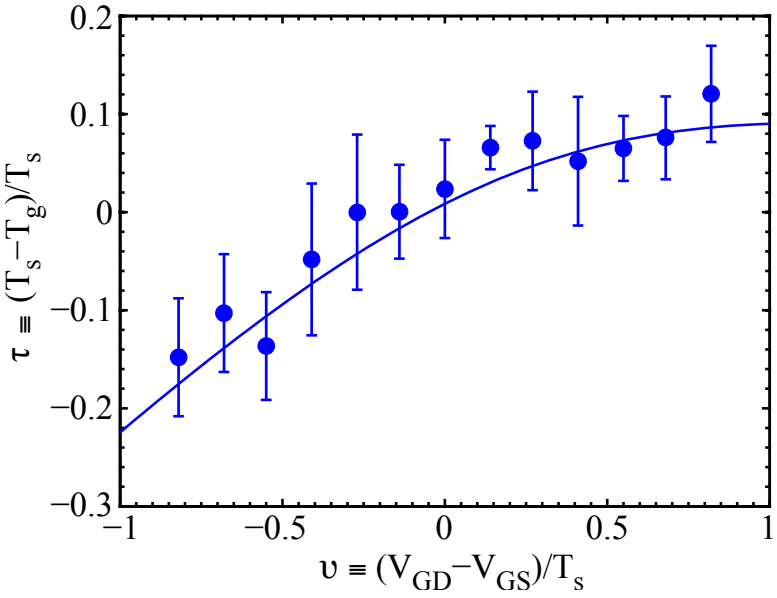

Figure 5.18: Temperature drop between the source and gate wells of the atomtronic transistor after an evolution time of 30 ms. Error bars represent the 95% confidence interval of the Gaussian fit to wings of the in-trap density profile for five experimental realizations at each feedback parameter.

experimental data at large feedback parameters is a result of the increasing atom density in the gate. Large densities lessen the reduction of the scattering cross section because the cloud is optically thicker.[8] As a result, the experimental data for the gate atom number at large positive feedback parameters is less than the numerically calculated population. The temperature drop data is also compared to the numerical calculation. As alluded to previously, results of the RK4 calculation accurately reproduce τ as a function of υ. The numerical results are indicated by the solid line in Figure 5.18. We find good qualitative agreement to within the error bars of the temperature drop data, which represent the 95% confidence interval of the fit to the in-trap density profile.

Using the gate well atom number from Figure 5.17 and temperature data from Figure 5.18, the chemical potential in the gate well is calculated in the TF limit in a harmonic well. The chemical potential drop, $\hat{\mu}_{\rm sg} \equiv (\mu_{\rm s} - \mu_{\rm g})/k_B T_{\rm s}$, characterizes the chemical potential gradient between the source and gate wells, and is shown in Figure 5.19. For values of $\upsilon > 0.2$ the chemical potential drop is negative, revealing that the chemical potential in the gate well exceeds that of the source well. Furthermore, we determine the critical feedback parameter, $\upsilon_{\rm BEC} = -0.24$, above which a condensate forms in the gate well in steady-state. Below this threshold ($\upsilon < \upsilon_{\rm BEC}$) the chemical potential drop reflects the positive chemical potential of the source well relative to $V_{\rm G,0}$. The same behavior was found in the analytic model for the steady-state behavior in the triple-well system shown in Figure 2.6 where the curves are dashed in the absence of a BEC.

5.5.4 Further discussion

It is worth elaborating further on the presence of a negative chemical potential gradient between the source and gate wells. At first glance it may appear that in order to sustain

[8] The saturation parameter, $s_0 = I_p/I_{sat}$, used in the experiment results in a reduction of the effective cross section (see Equation (4.18)) that is determined to be $C = (\sigma/\sigma_{eff}) = 9.3(1)$. Steady-state gate numbers at higher υ can be determined by further saturating the optical transition, but this also leads to a decrease in sensitivity to the population at $\upsilon \lesssim 0$.

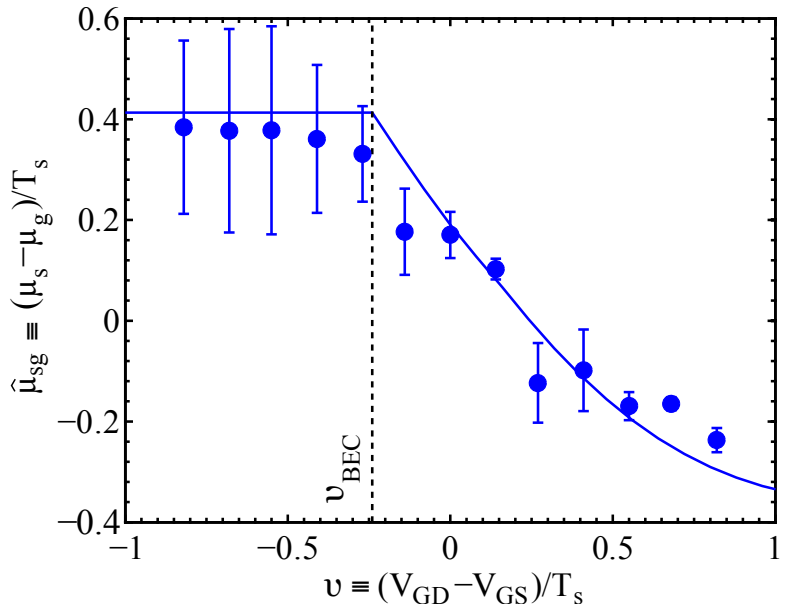

Figure 5.19: Chemical potential drop between the source and gate wells of the atomtronic transistor after an evolution time of 30 ms. Error bars represent the standard error on the mean propagated from the uncertainty in N_{gate} and T_{gate}.

a positive net source-gate current in this operating regime, work must constantly be done on the system. However, current flows due to gradients in both chemical potential and temperature. Thus, although the chemical potential gradient is negative, there is a positive temperature gradient that sustains current flow from source to gate. Additionally, a negative gradient in the chemical potential represents the conversion of thermal energy in the source to chemical potential energy in the gate. This process decreases the local entropy of the system; however, the presence of the terminator beam makes this an open system such that globally the entropy of the system increases and the second law of thermodynamics is upheld.

The data in Figures 5.18 and 5.19 confirm that by tuning the feedback parameter it is possible to achieve quasi-steady-state ensembles in the source and gate that are related by temperature and chemical potential drops. Returning to the analogy of electronic transistor operation, the resulting potential drops are a demonstration of the self-biasing behavior that were predicted in Section 2.2.3. Electronic transistor functionality largely depends on the bias or quiescent operating point set by the voltages at each of its three terminals. The experimental results demonstrated here show that the atomtronic transistor can be tuned to regions of either positive or negative chemical potential drops between the source and gate wells, indicating operation in forward and reverse-bias modes, respectively.

Chapter 6

Outlook

This dissertation has described the experimental realization of two fundamental atomtronic circuit elements: a battery and transistor. In addition to the demonstration of these atomtronic devices, a semiclassical analytical model was used to explore the transistor-like behavior of the triple-well system, explicitly its ability to exhibit current gain. Furthermore, the atom-chip-based apparatus that was constructed to demonstrate these atomtronic devices provides the experimenter the ability to reconfigure the trapping potential in order to prototype future atomtronic circuit elements. Building upon this body of work, three avenues of continued research are outlined in the following sections.

6.1 Current controlled atomtronic transistors

The first research avenue is a direct continuation of experimental work presented in Chapter 5 towards the goal of demonstrating a current controlled transistor, using the current gain predictions of the semiclassical model (Figure 2.7) as a guide. Ultimately, the utility of a transistor lies in the ability to control a large current or voltage at the output of the device via the application of a smaller control current or voltage. Such an ultracold atom amplifier would be immediately applicable to the AMO community.

In order to realize a current controlled atomtronic transistor, it is necessary to create a second reservoir to serve as the source of the control current. This is theoretically possible in the current experimental apparatus owing to the flexibility of the 2D AOD, though system

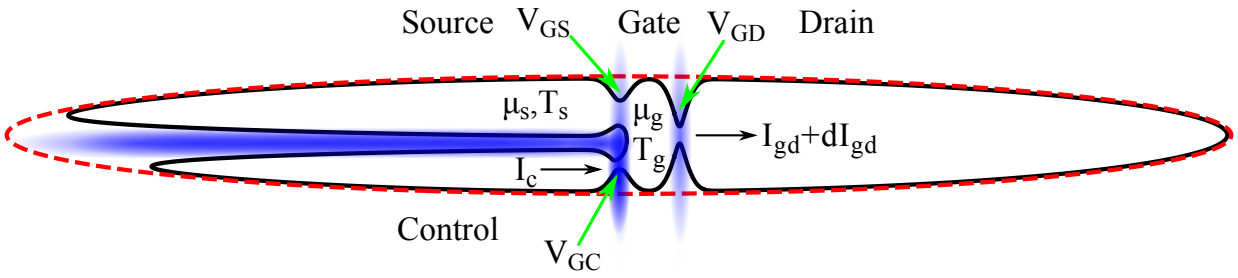

Figure 6.1: Possible experimental potential to study a current controlled atomtronic transistor. A contour of the total potential (solid black curve) is shown that has three wells. The bare magnetic potential is also shown (red dashed curve). A blue-detuned optical barrier bisects the original source well to create a control well. The three wells are then separated by independently controlled barriers, V_{GS}, V_{GC}, and V_{GD}. The initial state would be prepared according to the previously described procedure, followed by ramping up a barrier to separate the source and control wells.

initialization and actuation must be carefully considered. Figure 6.1 shows an illustration of one possible design that could be used to study current gain. An alternative approach would be to utilize the trapping techniques described in References [20, 138] or [139], in which an all optical potential allows atom currents to flow along two dimensions.

6.1.1 More complex atomtronic devices

Once a current controlled transistor has been realized, it becomes possible to again draw on the analogy with electronics to construct more complex atomtronic devices. In two dimensions, the current controlled transistor potential could be realized as is shown in Figure 6.2(a), which leaves the source, gate, and drain wells relatively unchanged from the implementation used to conduct the experiments of Chapter 5. One can imagine interconnecting multiple transistors to realize atomtronic analogues to logic gates and more complex transistor based circuits. As an example, a possible implementation of a flip-flop is shown in Figure 6.2(b). Since the current gain described in Section 2.2.4 is differential, the characteristic behavior of the electronic counterparts to these devices would then appear as a deviation from the steady-state output of each of the individual atomtronic transistors.

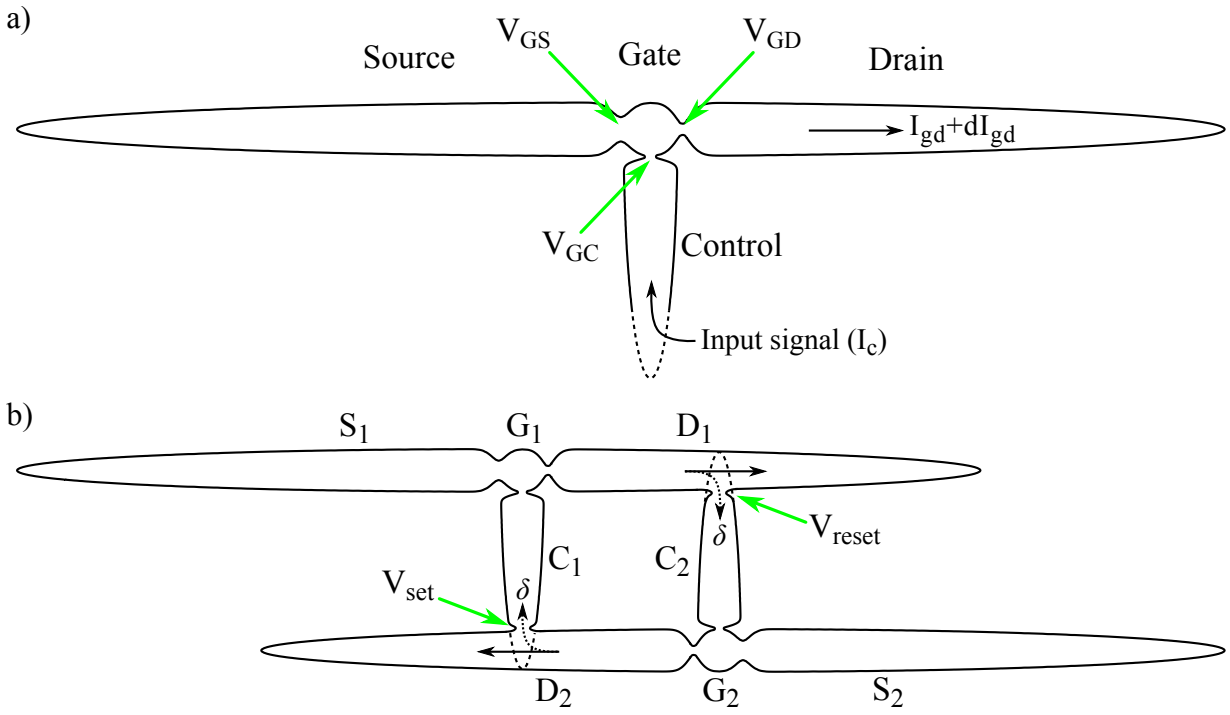

Figure 6.2: a) A possible two dimensional potential for a current controlled atomtronic transistor generated using all optical potentials. This geometry also allows the input current to originate from a separate potential from which the signal to be amplified originates. The behavior of the current controlled transistor is described in Section 2.2.4. b) One possible realization of a flip-flop circuit built from two transistor potentials shown in (a). This configuration would exhibit flip-flop-like behavior about the steady-state operating conditions determined by the feedback parameter of each transistor. For example, assuming a small coupling ratio, δ, between the drain current in D_1 and the connected control C_2, the drain current in D_1 would decrease to $I'_{\mathrm{gd},1} = (1-\delta)I_{\mathrm{gd},1}$, while the drain current in D_2 would increase to $I'_{\mathrm{gd},2} = (1+\delta A_I)I_{\mathrm{gd},2}$. The same behavior would occur in the other transistor, and the drain output currents of the two transistors would alternate with one higher and the other lower than the steady-state I_{gd}, and vice versa, depending on the sign of A_I set by υ. As in an electronic flip-flop, set and reset elements are included, here in the form of barriers. In analogy to grounding the gate input, a large $V_{(\mathrm{re})\mathrm{set}}$ shuts off current flow into the control gate of the respective transistor potential, i.e., $\delta \to 0$, returning the drain current to the steady-state value.

6.2 Coherent behavior

The work in this dissertation has approached the problem of realizing an atomtronic transistor from a semiclassical perspective in which the bulk of the quantum behavior is hidden within interactions that give rise to the positive valued chemical potential. However, an attractive concept in atomtronics is the ability to influence the coherence of an atomic signal. In the context of the triple well system studied here, coherence can refer to phase-locking between condensates in the source- and gate-wells, which is studied theoretically in Reference [26], or the coherence of the drain current. The remainder of this section discusses ongoing attempts to control the degree of coherence of the atom current emitted into the drain.

Conceptually, it should be possible to couple the motional state of the condensate trapped in the gate well to higher lying energy states, thus establishing coherence between energy levels that contribute to the gate-drain current. Figure 6.3 illustrates the simplified model of the gate well that is used to discuss the generation of coherence in the gate-drain current. Notice that states below the barrier height are considered, indicating the presence of quantum mechanical tunneling. Also, consider that the properties of the gate barriers including their widths, heights, and separation have been designed to provide preferential transmission of atoms in levels $|g\rangle$ and $|e\rangle$. Methods for designing such a potential are discussed in Section 6.3. The energy level spacing of $|g\rangle$ and $|e\rangle$ is given by $E/\hbar = \Omega$, and is equivalent to the oscillation frequency of the center of mass dipole mode of the gate well condensate. Intraparticle interactions, e.g. mean-field effects, lead to the conversion of energy stored in the collective motion of the condensate to the higher lying states, a process similar to Landau-damping [43]. In this manner, it is expected that the output modes of the gate, i.e., γ_g and γ_e, develop a coherent relationship to both the condensate in the gate well and one another. Ongoing theoretical treatment of this model system draws upon methods from semiclassical laser theory [140] with possible extension to the quantum master equation.

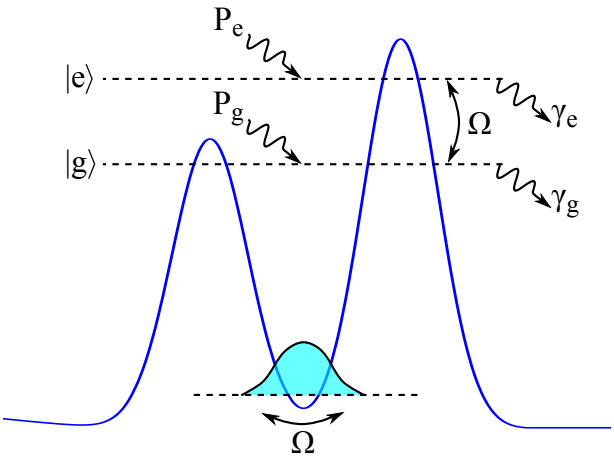

Figure 6.3: Schematic of the model system for realizing coherent transistor output. Gate well populations in energy levels $|g\rangle$ and $|e\rangle$ are pumped by the source-gate current, P_g and P_e, respectively, and decay by emitting current into the drain, at γ_g and γ_e. The gate well condensate prepared in the dipole mode (center of mass oscillation) then couples the two states, generating a coherent output current into the drain.

Coherence properties of atoms can be probed using several methods including spatial interference [141] and measurements of correlation functions [142, 143, 144]. Images of the spatial distribution of trapped atoms have been used to show that the correlations persist within the trap, but require Fourier analysis and well-characterized, high-resolution imaging [145]. Future implementation of such techniques may prove useful in measuring spatial correlations in the drain current of the atomtronic transistor.

6.3 Tailored barrier transmission

As alluded to in previous chapters, the ability to design the potential landscape of an atomtronic circuit element to realize specific behavior of the atomic current and thermodynamic potentials is an attractive and powerful concept. Ultimately, the relevant characteristics of the potential are the energy dependent transmission and reflection of matter waves. While this problem can be approached analytically, e.g. using the WKB approximation, solutions for all but the simplest of potentials are non-trivial and instead require numerical calculation. Drawing upon the analogy to the propagation of an electromagnetic wave in a transmission line, the generalized impedance (GI) concept provides an easily implemented numerical approach to determine the wave transmission and reflection of an arbitrary potential [65].

Originally developed to treat currents due to quantum mechanical tunneling in semiconductor electronics [146], the GI concept has been extended to treat wave transmission through arbitrary potentials [126]. Calculations using this method accurately reproduce the results of recent experiments that measure energy dependent reflection from a periodic potential synonymous with a Bragg reflector [67]. Synthesized potentials of this type could be applied towards the realization of resonant atomtronic circuit elements as well as other systems in the field of atom optics, such as a matter wave Fabry-Pérot interferometer [147]. Theoretical application of the GI concept to the atomtronic transistor system is ongoing and shows promise towards the experimental realization of previously discussed coherent output

currents and other interesting behavior that arises due to quantum mechanical tunneling.

Bibliography

[1] T. A. Edison, "Electric-Lamp." Patent 223,898, Jan. 1880.

[2] O. W. Richardson, The Emission of Electricity from Hot Bodies. London: Longmans, Green and Co., 2nd ed., 1921.

[3] J. Bardeen and W. H. Brattain, "The Transistor, A Semi-Conductor Triode," Physical Review, vol. 74, p. 230, 1948.

[4] J. A. Fleming, The Thermionic Valve and its Developments in Radiotelegraphy and Telephony. The Wireless Press, Ltd., 1919.

[5] L. J. Peters, Theory of Thermionic Vacuum Tube Circuits. New York: McGraw-Hill Book Company, Inc., 1st ed., 1927.

[6] E. L. Chaffee, Theory of Thermionic Vacuum Tubes. McGraw-Hill Book Company, Inc., 1933.

[7] J. Bardeen and W. H. Brattain, "Physical Principles Involved in Transistor Action," Physical Review, vol. 75, no. 8, p. 1208, 1949.

[8] D. Heiss, ed., Fundamentals of Quantum Information. New York: Springer, 2002.

[9] G. Leuchs and T. Beth, eds., Quantum Information Processing. Weinheim: Wiley-VCH, 2003.

[10] M. B. Squires, High repetition rate Bose-Einstein condensate production in a compact, transportable vacuum system. PhD thesis, University of Colorado at Boulder, 2008.

[11] S. R. Segal, Progress Towards an Ultracold Atomic Sagnac Gyroscope. PhD thesis, University of Colorado at Boulder, 2010.

[12] E. A. Salim, Ultracold matter systems and atomtronics instrumentation. PhD thesis, University of Colorado at Boulder, 2011.

[13] K. M. Hudek, A Compact and Transportable Ultracold Matter System and Progress Towards a Continuously Operating Neutral Rydberg Atom Quantum Computer. PhD thesis, University of Colorado at Boulder, 2012.

[14] R. Gati, M. Albiez, J. Fölling, B. Hemmerling, and M. K. Oberthaler, "Realization of a single Josephson junction for Bose-Einstein condensates," Applied Physics B, vol. 82, pp. 207–210, 2006.

[15] R. Gati and M. K. Oberthaler, "A bosonic Josephson junction," Journal of Physics B: Atomic, Molecular and Optical Physics, vol. 400, pp. R61–R89, 2007.

[16] M. Rab, J. H. Cole, N. G. Parker, A. D. Greentree, L. C. L. Hollenberg, and A. M. Martin, "Spatial coherent transport of interacting dilute Bose gases," Physical Review A, vol. 77, no. 061602, 2008.

[17] S. Moulder, S. Beattie, R. P. Smith, N. Tammuz, and Z. Hadzibabic, "Quantized supercurrent decay in an annular Bose-Einstein condensate," Physical Review A, vol. 86, no. 013629, 2012.

[18] C. Ryu, P. W. Blackburn, A. A. Blinova, and M. G. Boshier, "Experimental Realization of Josephson Junctions for an Atom SQUID," Physical Review Letters, vol. 111, no. 205301, 2013.

[19] S. Eckel, J. G. Lee, F. Jendrzejewski, N. Murray, C. W. Clark, C. J. Lobb, W. D. Phillips, M. Edwards, and G. K. Campbell, "Hysteresis in a quantized superfluid 'atomtronic' circuit," Nature, vol. 506, pp. 200–203, 2014.

[20] C. Ryu and M. G. Boshier, "Integrated coherent matter wave circuits," New Journal of Physics, vol. 17, no. 092002, 2015.

[21] B. T. Seaman, M. Krämer, D. Z. Anderson, and M. J. Holland, "Atomtronics: Ultracold-atom analogs of electronic devices," Phys. Rev. A, vol. 75, p. 023615, 2007.

[22] J. A. Stickney, D. Z. Anderson, and A. A. Zozulya, "Transistor-like behavior of a bose-einstein condensate in a triple-well potential," Physical Review A, vol. 75, p. 013608, 2007.

[23] R. A. Pepino, J. Cooper, D. Z. Anderson, and M. J. Holland, "Atomtronic Circuits of Diodes and Transistors," Physical Review Letters, vol. 103, no. 140405, 2009.

[24] R. A. Pepino, J. Cooper, D. Meiser, D. Z. Anderson, and M. J. Holland, "Open quantum systems approach to atomtronics," Phys. Rev. A, vol. 82, p. 013640, 2010.

[25] M. Gajdacz, T. Opatrný, and K. K. Das, "An atomtronics transistor for quantum gates," Physics Letters A, vol. 378, pp. 1919–1924, 2014.

[26] W. W. Chow, C. J. E. Straatsma, and D. Z. Anderson, "Numerical model for atomtronic circuit analysis," Physical Review A, vol. 92, no. 013621, 2015.

[27] R. Landauer, "Irreversibility and Heat Generation in the Computing Process," IBM Journal of Research and Development, vol. 5, pp. 183–191, 1961.

[28] J. Rothstein, "Information, measurement, and quantum mechanics," Science, vol. 114, pp. 171–175, 1951.

[29] D. G. Miller, "Thermodynamics of irreversible processes, the experimental verification of the Onsager reciprocal relations," Chemical Reviews, vol. 60, pp. 15–37, 1960.

[30] F. Jendrzejewski, S. Eckel, N. Murray, C. Lanier, M. Edwards, C. J. Lobb, and G. K. Campbell, "Resistive Flow in a Weakly Interacting Bose-Einstein Condensate," Physical Review Letters, vol. 113, no. 045305, 2014.

[31] P. Faist, F. Dupuis, J. Oppenheim, and R. Renner, "The minimal work cost of information processing," Nature Communications, vol. 6, no. 7669, 2015.

[32] A. Micheli, A. J. Daley, D. Jaksch, and P. Zoller, "Single Atom Transistor in a 1D Optical Lattice," Physical Review Letters, vol. 93, no. 140408, 2004.

[33] J. Y. Vaishnav, J. Ruseckas, C. W. Clark, and G. Juzeliūnas, "Spin Field Effect Transistors with Ultracold Atoms," Physical Review Letters, vol. 101, no. 265302, 2008.

[34] A. Benseny, S. Fernández-Vidal, J. Bagudà, R. Corbalán, A. Picón, L. Roso, G. Birkl, and J. Mompart, "Atomtronics with holes: Coherent transport of an empty site in a triple-well potential," Physical Review A, vol. 82, no. 013604, 2010.

[35] W. A. Davis, Radio Frequency Circuit Design. John Wiley & Sons Inc., 2nd ed., 1953.

[36] W. A. Edson, Vacuum Tube Oscillators. John Wiley & Sons Inc., 1953.

[37] R. K. Willardson and A. C. Beer, eds., Semiconductors and Semimetals, Vol. 7. Academic Press Inc., San Diego, 1971.

[38] P. Makotyn, C. E. Klauss, D. L. Goldberger, E. A. Cornell, and D. S. Jin, "Universal dynamics of a degenerate unitary Bose gas," Nature Physics, vol. 10, pp. 116–119, 2014.

[39] Y.-J. Wang, D. Z. Anderson, V. M. Bright, E. A. Cornell, Q. Diot, T. Kishimoto, M. Prentiss, R. A. Saravanan, S. R. Segal, and S. Wu, "Atom Michelson Interferometer on a Chip Using a Bose-Einstein Condensate," Physical Review Letters, vol. 94, no. 090405, 2005.

[40] T. Berrada, S. van Frank, R. Bücker, T. Schumm, J.-F. Schaff, and J. Schmiedmayer, "Integrated Mach–Zehnder interferometer for Bose–Einstein condensates," Nature Communications, vol. 4, no. 2077, 2013.

[41] R. K. Pathria and P. D. Beale, Statistical Mechanics. Boston: Elsevier, 3 ed., 2011.

[42] M. Inguscio, S. Stringari, and C. E. Wieman, eds., Bose-Einstein Condensation in Atomic Gases: Proceedings of the International School of Physics "Enrico Fermi". Oxford: IOS Press, 1999.

[43] C. J. Pethick and H. Smith, Bose-Einstein Condensation in Dilute Gases. Cambridge University Press, 2002.

[44] S. Giorgini, L. Pitaevskii, and S. Stringari, "Thermodynamics of a Trapped Bose-Condensed Gas," Journal of Low Temperature Physics, vol. 109, no. 1-2, pp. 309–355, 1997.

[45] A. Griffin, T. Nikuni, and E. Zaremba, Bose-Condensed Gases at Finite Temperatures. Cambridge University Press, Cambridge, 2009.

[46] K. Huang, Statistical Mechanics. New York: John Wiley & Sons Inc., 1987.

[47] D. Vudragović, I. Vidanović, A. Balaž, P. Muruganandamb, and S. K. Adhikari, "C programs for solving the time-dependent Gross–Pitaevskii equation in a fully anisotropic trap," Computer Physics Communications, vol. 183, pp. 2021–2025, 2012.

[48] S. C. Caliga, C. J. E. Straatsma, A. A. Zozulya, and D. Z. Anderson, "Principles of an atomtronic transistor," New Journal of Physics, vol. 18, no. 015012, 2015.

[49] S. M. Sze, Physics of Semiconductor Devices. John Wiley & Sons Inc., 1969.

[50] R. J. Smith, Circuits, Devices, and Systems. John Wiley & Sons Inc., 2nd ed., 1969.

[51] H. A. Bethe, "Theory of the Boundary Layer of Crystal Rectifiers," MIT Radiation Laboratory Report, vol. 43, no. 12, 1942.

[52] O. Luiten, M. Reynolds, and J. Walraven, "Kinetic theory of the evaporative cooling of a trapped gas," Physical Review A, vol. 53, 1996.

[53] J. T. M. Walraven, "Atomic hydrogen in magnetostatic traps," in Quantum Dynamics of Simple Systems (G.-L. Oppo, S. M. Barnett, R. Riis, and M. Wilkinson, eds.), pp. 315–352, IOP, Bristol, 1996.

[54] Y. Shin, M. Saba, A. Schirotzek, T. A. Pasquini, A. E. Leanhardt, D. E. Pritchard, and W. Ketterle, "Distillation of Bose-Einstein Condensates in a Double-Well Potential," Physical Review Letters, vol. 92, no. 150401, 2004.

[55] J.-P. Brantut, J. Meineke, D. Stadler, S. Krinner, and T. Esslinger, "Conduction of Ultracold Fermions Through a Mesoscopic Channel," Science, vol. 337, 2012.

[56] J.-P. Brantut, C. Grenier, J. Meineke, D. Stadler, S. Krinner, C. Kollath, T. Esslinger, and A. Georges, "A Thermoelectric Heat Engine with Ultracold Atoms," Science, vol. 342, pp. 713–715, 2013.

[57] E. L. Hazlett, L.-C. Ha, and C. Chin, "Anomalous thermoelectric transport in two-dimensional Bose gas," no. arXiv:1306.4018, 2013.

[58] J. G. Lee, B. J. McIlvain, C. J. Lobb, and W. T. H. III, "Analogs of Basic Electronic Circuit Elements in a Free-Space Atom Chip," Scientific Reports, vol. 3, no. 1034, 2013.

[59] R. Labouvie, B. Santra, S. Heun, S. Wimberger, and H. Ott, "Negative Differential Conductivity in an Interacting Quantum Gas," Physical Review Letters, vol. 115, no. 050601, 2015.

[60] C. F. Roos, P. Cren, D. Guéry-Odelin, and J. Dalibard, "Continuous loading of a non-dissipative atom trap," Europhys. Lett., vol. 61, no. 2, pp. 187–193, 2003.

[61] F. Dalfovo, S. Giorgini, L. P. Pitaevskii, and S. Stringari, "Theory of Bose-Einstein condensation in trapped gases," Rev. Mod. Phys., vol. 71, pp. 463–512, 1999.

[62] V. C. Wilson, "Conversion of Heat to Electricity by Thermionic Emission," Journal of Applied Physics, vol. 30, no. 4, pp. 475–481, 1959.

[63] L. Onsager, "Reciprocal Relations in Irreversible Processes. I.," Physical Review, vol. 37, no. 405, 1931.

[64] S. Mokhov and B. Y. Zeldovich, "Strength of electromagnetic, acoustic and Schrodinger reflections," Proc. R. Soc. A, vol. 464, no. 2099, pp. 3071–3080, 2008.

[65] A. N. Khondker, M. R. Khan, and A. F. M. Anwar, "Transmission line analogy of resonance tunneling phenomena: The generalized impedance concept," Journal of Applied Physics, vol. 63, no. 5191, 1988.

[66] C. Cheiney, C. M. Fabre, F. Vermersch, G. L. Gattobigio, R. Mathevet, T. Lahaye, and D. Guéry-Odelin, "Matter-wave scattering on an amplitude-modulated optical lattice," Physical Review A, vol. 87, no. 013623, 2013.

[67] C. M. Fabre, P. Cheiney, G. L. Gattobigio, F. Vermersch, S. Faure, R. Mathevet, T. Lahaye, and D. Guéry-Odelin, "Realization of a Distributed Bragg Reflector for Propagating Guided Matter Waves," Physical Review Letters, vol. 107, no. 230401, 2011.

[68] H. Ott, J. Fortagh, G. Schlotterbeck, A. Grossmann, and C. Zimmermann, "Bose-Einstein Condensation in a Surface Microtrap," Physical Review Letters, vol. 87, no. 230401, 2001.

[69] D. M. Farkas, K. M. Hudek, E. A. Salim, S. R. Segal, M. B. Squires, and D. Z. Anderson, "A compact, transportable, microchip-based system for high repetition rate production of Bose–Einstein condensates," Applied Physics Letters, vol. 96, no. 093102, 2010.

[70] D. M. Farkas, E. A. Salim, and J. R.-Serrano, "Production of Rubidium Bose-Einstein Condensates at a 1 Hz Rate," arXiv:1403.4641, 2014.

[71] J. Rudolph, W. Herr, C. G. andT. Sternke, A. Grote, M. Popp, D. Becker, H. Müntinga, H. Ahlers, A. Peters, C. Lämmerzahl, K. Sengstock, N. Gaaloul, W. Ertmer, and E. M. Rasel, "A high-flux BEC source for mobile atom interferometers," New Journal of Physics, vol. 17, no. 065001, 2015.

[72] W. Ketterle and D. E. Pritchard, "Trapping and Focusing Ground State Atoms with Static Fields," Applied Physics B, vol. 54, pp. 403–406, 1992.

[73] J. Schmiedmayer, "A wire trap for neutral atoms," Applied Physics B, vol. 60, pp. 169–179, 1995.

[74] T. Roach, H. Abele, M. G. Boshier, H. L. Grossman, K. P. Zetie, and E. Hinds, "Realization of a Magnetic Mirror for Cold Atoms," Phys. Rev. Lett., vol. 75, no. 4, pp. 629–632, 1995.

[75] J. H. Thywissen, M. Olshanii, G. Zabow, M. Drndić, K. S. Johnsonb, R. M. Westervelt, and M. Prentiss, "Microfabricated magnetic waveguides for neutral atoms," European Physics Journal D, vol. 7, pp. 361–367, 1999.

[76] R. Folman, P. Krüger, J. Schmiedmayer, J. Denschlag, and C. Henkel, "MIcroscopic atom optics: from wires to an atom chip," Advances in atomic, molecular, and optical physics, vol. 48, pp. 263–356, 2002.

[77] M. J. Pritchard, A. S. Arnold, D. A. Smith, and I. G. Hughes, "Single-impulse magnetic focusing of launched cold atoms," Journal of Physics B: Atomic, Molecular and Optical Physics, vol. 37, pp. 4435–4450, 2004.

[78] W. H. Wing, "On neutral particle trapping in quasistatic electromagnetic fields," Prog. Quant. Electr., vol. 8, pp. 181–199, 1984.

[79] A. Haase, D. Cassettari, B. Hessmo, and J. Schmiedmayer, "Trapping neutral atoms with a wire," Physical Review A, vol. 64, no. 043405, 2001.

[80] S. Gov, S. Shtrikman, and H. Thomas, "Magnetic trapping of neutral particles: Classical and quantum-mechanical study of a Ioffe–Pritchard type trap," Journal of Applied Physics, vol. 87, no. 8, pp. 3989–3998, 2000.

[81] D. E. Pritchard, "Cooling Neutral Atoms in a Magnetic Trap for Precision Spectroscopy," Phys. Rev. Lett., vol. 51, no. 15, pp. 1336–1339, 1983.

[82] E. A. Salim, J. DeNatale, D. M. Farkas, K. M. Hudek, S. E. McBride, J. Michalchuk, R. Mihailovich, and D. Z. Anderson, "Compact, microchip-based systems for practical applications of ultracold atoms," Quantum Inf. Process., vol. 10, no. 6, pp. 975–994, 2011.

[83] S. Du, Atom-chip Bose-Einstein condensation in a portable vacuum cell. PhD thesis, University of Colorado at Boulder, 2005.

[84] E. A. Salim, S. C. Caliga, J. B. Pfeiffer, and D. Z. Anderson, "High resolution imaging and optical control of Bose-Einstein condensates in an atom chip magnetic trap," Appl. Phys. Lett., vol. 102, p. 084104, 2013.

[85] Boulder labs Inc, 7105 LaVista Pl. Suite 200, Niwot, CO 80503: www.boulderlabs.com.

[86] R. Folman, P. Krüger, D. Cassettari, B. Hessmo, T. Maier, and J. Schmiedmayer, "Controlling Cold Atoms using Nanofabricated Surfaces: Atom Chips," Physical Review Letters, vol. 84, no. 20, pp. 4749–4752, 2000.

[87] C. J. E. Straatsma, M. K. Ivory, J. Dugan, J. R.-Serrano, D. Z. Anderson, and E. A. Salim, "On-chip optical lattice for cold atom experiments," Optics Letters, vol. 40, no. 14, pp. 3368–3371, 2015.

[88] F. H. Mies, C. J. Williams, P. S. Julienne, and M. Krauss, "Estimating Bounds on Collisional Relaxation Rates of Spin-Polarized ^{8}7Rb Atoms at Ultracold Temperatures," J. Res. Natl. Inst. Stand. Technol., vol. 101, no. 521, 1996.

[89] T. A. Savard, K. M. O'Hara, and J. E. Thomas, "Laser-noise-induced heating in far-off resonance optical traps," Physical Review A, vol. 56, no. 2, pp. 1095–1098, 1997.

[90] M. E. Gehm, K. M. O'Hara, T. A. Savard, and J. E. Thomas, "Dynamics of noise-induced heating in atom traps," Physics Letters A, vol. 58, no. 5, pp. 3914–3921, 1998.

[91] M. K. Ivory, A. R. Ziltz, C. T. Fancher, A. J. Pyle, A. Sensharma, B. Chase, J. P. Field, A. Garcia, D. Jervis, and S. Aubin, "Atom chip apparatus for experiments with ultracold rubidium and potassium gases," Review of Scientific Instruments, vol. 85, no. 043102, 2014.

[92] T. P. Purdy and D. M. Stamper-Kurn, "Integrating cavity quantum electrodynamics and ultracold-atom chips with on-chip dielectric mirrors and temperature stabilization," Applied Physics B, vol. 90, no. 3, pp. 401–405, 2008.

[93] P. Treutlein, Coherent manipulation of ultracold atoms on atom chips. PhD thesis, Ludwig-Maximilians Universität München and Max-Planck-Institut für Quantenoptick, 2008.

[94] H.-C. Chuang, E. A. Salim, V. Vuletic, D. Z. Anderson, and V. M. Bright, "Multilayer atom chips for atom tunneling experiments near the chip surface," Sensors and Actuators A, vol. 165, pp. 101–106, 2011.

[95] M. Trinker, S. Groth, S. Haslinger, S. Manz, T. Betz, S. Schneider, I. Bar-Joseph, T. Schumm, and J. Schmiedmayer, "Multilayer atom chips for versatile atom micromanipulation," Applied Physics Letters, vol. 92, no. 254102, 2008.

[96] S. Groth, P. Krüger, S. Wildermuth, R. Folman, T. Fernholz, J. Schmiedmayer, D. Mahalu, and I. Bar-Joseph, "Atom chips: Fabrication and thermal properties," Applied Physics Letters, vol. 85, no. 14, pp. 2980–2982, 2004.

[97] G. Nellis and S. Klein, Heat Transfer. Cambridge University Press, Cambridge, 2009.

[98] I. Bloch, J. Dalibard, and W. Zwerger, "Many-body physics with ultracold gases," Rev. Mod. Phys., vol. 80, pp. 885–964, 2008.

[99] W. S. Bakr, J. I. Gillen, A. Peng, S. Fölling, and M. Greiner, "A quantum gas microscope for detecting single atoms in a Hubbard-regime optical lattice," Nature, vol. 462, pp. 74–77, 2009.

[100] J. Sherson, C. Weitenberg, M. Endres, M. Cheneau, I. Bloch, and S. Kuhr, "Single-atom-resolved fluorescence imaging of an atomic Mott insulator," Nature, vol. 467, pp. 68–72, 2010.

[101] L. W. Cheuk, M. A. Nichols, M. Okan, T. Gersdorf, V. V. Ramasesh, W. S. Bakr, T. Lompe, and M. W. Zwierlein, "Quantum-Gas Microscope for Fermionic Atoms," Physical Review Letters, vol. 114, no. 193001, 2015.

[102] G. J. A. Edge, R. Anderson, D. Jervis, D. C. McKay, R. Day, S. Trotzky, and J. H. Thywissen, "Imaging and addressing of individual fermionic atoms in an optical lattice," Physical Review A, vol. 92, no. 063406, 2015.

[103] P. Schauß, J. Zeiher, T. Fukuhara, S. Hild, M. Cheneau, T. Macrì, T. Pohl, I. Bloch, and C. Gross, "Crystallization in Ising quantum magnets," Science, vol. 347, no. 6229, pp. 1455–1458, 2015.

[104] M. Endres, M. Cheneau, T. Fukuhara, C. Weitenberg, P. Schauß, C. Gross, L. Mazza, M. C. Bañuls, L. Pollet, I. Bloch, and S. Kuhr, "Single-site- and single-atom-resolved measurement of correlation functions," Applied Physics B, vol. 113, pp. 27–39, 2013.

[105] S. Braun, J. P. Ronzheimer, M. Schreiber, S. S. Hodgman, T. Rom, I. Bloch, and U. Schneider, "Negative Absolute Temperature for Motional Degrees of Freedom," Science, vol. 339, pp. 52–55, 2013.

[106] M. Fox, Optical Properties of Solids. Oxford: Oxford University Press, 2001.

[107] R. Grimm, M. Weidemüller, and Y. B. Ovchinnikov, "Optical Dipole Traps for Neutral Atoms," Advances in atomic, molecular, and optical physics, vol. 42, pp. 95–170, 2000.

[108] W. Ketterle, D. S. Durfee, and D. M. Stamper-Kurn, "Making probing and understanding Bose-Einstein condensates," in Proceedings of the Enrico Fermi summer school, 1999.

[109] R. Loudon, The Quantum Theory of Light, vol. 3rd. Oxford: Oxford University Press, 2003.

[110] D. A. Steck, Rubidium 87 D Line Data. http://steck.us/alkalidata.

[111] P. Würtz, Imaging the microscopic structure of ultracold quantum gases. PhD thesis, Technical University of Kaiserslautern, 2012.

[112] M. R. Matthews, Two-Component Bose-Einstein Condensation. PhD thesis, University of Colorado at Boulder, 1999.

[113] P. C. Haljan, Vortices in Bose-Einstein Condensates. PhD thesis, University of Colorado at Boulder, 2003.

[114] G. Reinaudi, T. Lahaye, Z. Wang, and D. Guéry-Odelin, "Strong saturation absorption imaging of dense clouds of ultracold atoms," Optics Letters, vol. 32, no. 21, 2007.

[115] J. Szczepkowski, R. Gartman, M. Witkowski, L. Tracewksi, M. Zawada, and W. Gawlik, "Analysis and calibration of absorptive images of Bose-Einstein condensates at nonzero temperature," Review of Scientific Instruments, vol. 80, no. 053103, 2009.

[116] M. Pappa, P. C. Condylis, G. O. Konstantinidis, V. Bolpasi, A. Lazoudis, O. Morizot, D. Sahagun, M. Baker, and W. von Klitzing, "Ultra-sensitive atom imaging for matter-wave optics," New Journal of Physics, vol. 13, no. 115012, 2011.

[117] F. Gerbier, J. H. Thywissen, S. Richard, M. Hugbart, P. Bouyer, and A. Aspect, "Critical Temperature of a Trapped,Weakly Interacting Bose Gas," Physical Review Letters, vol. 92, no. 030405, 2004.

[118] H. J. Lewandowski, Coherences and correlations in an ultracold Bose gas. PhD thesis, University of Colorado at Boulder, 2002.

[119] L. Allen and J. H. Eberly, Optical resonance and two-level atoms. New York: Wiley, 1975.

[120] B. E. A. Saleh and M. C. Teich, Fundamentals of Photonics. New York: John Wiley & Sons Inc., 1991.

[121] Andor, Unravelling Sensitivity, Signal to Noise and Dynamic Range – EMCCD vs CCD. http://www.emccd.com/what_is_emccd/unraveling_sensitivity/, 2005.

[122] W. Ketterle and N. J. V. Druten, "Evaporative Cooling of Trapped Atoms," in Advances in Atomic, Molecular, and Optical Physics (B. Bederson and H. Walther, eds.), vol. 37, pp. 181–236, Academic Press, San Diego, 1996.

[123] H. J. Lewandowski, D. M. Harber, D. L. Whitaker, and E. A. Cornell, "Simplified System for Creating a Bose–Einstein Condensate," Journal of Low Temperature Physics, vol. 132, no. 516, pp. 309–367, 2003.

[124] A. A. Zozulya and D. Z. Anderson, "Principles of an atomtronic battery," Phys. Rev. A, vol. 88, p. 043641, 2013.

[125] D. J. Griffiths and C. A. Steinke, "Waves in locally periodic media," American Journal of Physics, vol. 69, pp. 137–154, 2001.

[126] B. G.-Medina, "Wave transmission through periodic, quasiperiodic, and random one-dimensional finite lattices," American Journal of Physics, vol. 81, pp. 104–111, 2013.

[127] D. M. Stamper-Kurn, H. J. Miesner, S. Inouye, M. R. Andrews, and W. Ketterle, "Collisionless and Hydrodynamic Excitations of a Bose-Einstein Condensate," Phys. Rev. Lett., vol. 81, p. 3, 1998.

[128] H. Wu, E. Arimondo, and C. J. Foot, "Dynamics of evaporative cooling for Bose-Einstein condensation," Physical Review A, vol. 56, no. 560, 1997.

[129] G. A. Bird, Molecular gas dynamics and the direct simulation of gas flows. Oxford: Clarendon Press, 1994.

[130] A. C. J. Wade, D. Baillie, and P. B. Blakie, "Direct simulation Monte Carlo method for cold-atom dynamics: Classical Boltzmann equation in the quantum collision regime," Physical Review A, vol. 84, no. 023612, 2011.

[131] A. G. Sykes and J. L. Bohn, "Nonequilibrium dynamics of an ultracold dipolar gas," Physical Review A, vol. 91, no. 013625, 2015.

[132] W. H. Press, S. A. Teukolsky, W. T. Vetterling, and B. P. Flannery, Numerical Recipes - The Art of Scientific Computing. New York: Cambridge University Press, 3rd ed., 2007.

[133] J. Zhang and J. Lee, "A review on prognostics and health monitoring of Li-ion battery," Journal of Power Sources, vol. 196, pp. 6007–6014, 2011.

[134] M. R. Jongerden and B. R. Haverkort, "Battery Modeling," Technical Report 1381-3625, Centre for Telematics and Information Technology University of Twente, 2008.

[135] J. Jung, L. Zhang, and J. Zhang, eds., Lead-Acid Battery Technologies - Fundamentals, Materials, and Applications. New York: CRC Press, 2016.

[136] S. C. Caliga, C. J. E. Straatsma, and D. Z. Anderson, "Transport dynamics of ultracold atoms in a triple-well transistor-like potential," New Journal of Physics, vol. 18, no. 025010, 2016.

[137] L. Gilz, L. R-Pérez, and J. R. Anglin, "Length scales involved in decoherence of trapped bosons by buffer-gas scattering," Physical Review A, vol. 89, no. 052131, 2014.

[138] K. Henderson, C. Ryu, C. MacCormick, and M. G. Boshier, "Experimental demonstration of painting arbitrary and dynamic potentials for Bose–Einstein condensates," New Journal of Physics, vol. 11, no. 043030, 2009.

[139] M. Pasienski and B. DeMarco, "A high-accuracy algorithm for designing arbitrary holographic atom traps," Optics Express, vol. 16, no. 2176, 2008.

[140] M. Sargent III, M. O. Scully, and W. E. Lamb, Jr., Laser Physics. Boulder: Westview Press, 5th ed., 1987.

[141] I. Bloch, T. W. Hänsch, and T. Esslinger, "Measurement of the spatial coherence of a trapped Bose gas at the phase transition," Nature, vol. 403, pp. 166–170, 2000.

[142] A. Öttl, S. Ritter, M. Köhl, and T. Esslinger, "Correlations and Counting Statistics of an Atom Laser," Physical Review Letters, vol. 95, no. 090404, 2005.

[143] R. G. Dall, S. S. Hodgman, A. G. Manning, M. T. Johnsson, K. G. H. Baldwin, and A. G. Truscott, "Observation of atomic speckle and Hanbury Brown–Twiss correlations in guided matter waves," Nature Communications, vol. 2, no. 291, 2011.

[144] A. Perrin, R. Bücker, S. Manz, T. Betz, C. Koller, T. Plisson, T. Schumm, and J. Schmiedmayer, "Hanbury Brown and Twiss correlations across the Bose–Einstein condensation threshold," Nature Physics, vol. 8, pp. 195–198, 2012.

[145] A. Blumkin, S. Rinott, R. Schley, A. Berkovitz, I. Shammass, and J. Steinhauer, "Observing Atom Bunching by the Fourier Slice Theorem," Physical Review Letters, vol. 110, no. 265301, 2013.

[146] Y. Ando and T. Itoh, "Calculation of transmission tunneling current across arbitrary potential barriers," Journal of Applied Physics, vol. 61, pp. 1497–1502, 1987.

[147] M. Wilkens, E. Goldstein, B. Taylor, and P. Meystre, "Fabry-Pérot interferometer for atoms," Physical Review A, vol. 47, no. 3, pp. 2366–2369, 1993.

Appendix A

Derivation of the normalized temperature and chemical potential drops

This section provides the derivations of the key relations in the analytic steady-state model of the atomtronic transistor, the normalized temperature and chemical potential drops provided in equations (2.39) and (2.40), respectfully. Given that the source well is maintained at a finite $\mu_{\rm s}$ & $T_{\rm s}$, and there are no external sources of atoms into the system, the potential drops are derived in a form that depends solely on $\mu_{\rm s}$ and $T_{\rm s}$. The first step in both derivations is to re-cast the current conservation relation from equation (2.35),

$$I_{\rm sg} = I_{\rm gs} + I_{\rm gd},$$

in terms of the feedback parameter, υ, which controls the ratio of $I_{\rm gd}/I_{\rm gs}$. Beginning from the expression for $I_{\rm gd}$ from equation (2.33),

$$I_{\rm gd} = \gamma_{\rm g} N_{\rm th,g}\, \exp[-(V_{\rm GD} - V_{\rm G,0} - \mu_{\rm g})/k_B T_{\rm g}]$$

and inserting unity as $1 = \exp\left[(V_{\rm GS} - V_{\rm GS})/k_B T_{\rm g}\right]$, one finds

$$I_{\rm gd} = \gamma_{\rm g} N_{\rm th,g} \exp\left[-(V_{\rm GD} - V_{\rm GS})/k_B T_{\rm g}\right] \exp\left[-(V_{\rm GS} - V_{\rm G,0} - \mu_{\rm g})/k_B T_{\rm g}\right]. \tag{A.1}$$

Next, inserting the barrier height difference, $\Delta V = V_{\rm GD} - V_{\rm GS}$, and pulling out a factor of $I_{\rm gs}$ simplifies equation (A.1) to

$$I_{\rm gd} \;=\; I_{\rm gs} e^{-\Delta V/k_B T_{\rm g}}, \tag{A.2}$$

which shows that the ratio $I_{\rm gd}/I_{\rm gs} = \exp\left[-\Delta V/k_B T_{\rm g}\right]$. Plugging equation (A.2) into the expression for current conservation and inserting the feedback parameter, $\upsilon \equiv (V_{\rm GD} - V_{\rm GS})/k_B T_{\rm s} \equiv \Delta V/T_{\rm s}$, along with $T_{\rm g}/T_{\rm s} = (1-\tau)$ simplifies equation (A.1) to

$$I_{\rm sg} \;=\; I_{\rm gs}\left(1 + e^{-\upsilon/(1-\tau)}\right). \tag{A.3}$$

Equation (A.3) is the modified current conservation relation and it is used in derivations of the transcendental equations for both τ and $\hat{\mu}_{\rm sg}$.

Temperature drop

In the derivation of the transcendental relation for the temperature drop temperature drop, $\tau \equiv \left(T_{\rm s} - T_{\rm g}\right)/T_{\rm s}$, one begins from the energy conservation equation, originally presented in equation (2.36):

$$I_{\rm sg}(V_{\rm GS} + \kappa_{\rm GS} k_B T_{\rm s}) \;=\; I_{\rm gs}(V_{\rm GS} + \kappa_{\rm GS} k_B T_{\rm g}) + I_{\rm gd}(V_{\rm GD} + \kappa_{\rm GD} k_B T_{\rm g}).$$

Dividing through by $I_{\rm gs}$, one then uses equation (A.3) to replace the ratio $I_{\rm sg}/I_{\rm gs}$ and equation (A.2) to replace to replace the ratio $I_{\rm gd}/I_{\rm gs}$, yielding

$$\begin{aligned}\left(V_{\rm GS} + \kappa_{\rm GS} k_B T_{\rm s}\right)\left(1 + e^{-\upsilon/(1-\tau)}\right) \;&=\; \left(V_{\rm GS} + \kappa_{\rm GS} k_B T_{\rm g}\right) \\ &+\; \left(V_{\rm GD} + \kappa_{\rm GD} k_B T_{\rm g}\right) e^{-\upsilon/(1-\tau)}.\end{aligned} \tag{A.4}$$

The remaining steps include algebraic manipulation of equation (A.4),

$$\kappa_{\rm GS}\left(k_B T_{\rm s} + k_B T_{\rm g}\right) \;=\; e^{-\upsilon/(1-\tau)}\left(\Delta V + \kappa_{\rm GD} k_B T_{\rm g} - \kappa_{\rm GS} k_B T_{\rm s}\right),$$

followed by dividing through by $k_B T_{\rm s}$ and inserting τ where appropriate,

$$\kappa_{\rm GS}\tau \;=\; e^{-\upsilon/(1-\tau)}\left(\upsilon + \kappa_{\rm GD}(1-\tau) - \kappa_{\rm GS}\right).$$

Finally, one obtains the expression for the temperature drop,

$$\tau \;=\; e^{-\upsilon/(1-\tau)}\frac{\upsilon + \left(\kappa_{\rm GD} - \kappa_{\rm GS}\right)}{\kappa_{\rm GS} + \kappa_{\rm GD} e^{-\upsilon/(1-\tau)}}. \tag{A.5}$$

Chemical potential drop

The transcendental relation for the normalized chemical potential drop is derived in a similar manner to the temperature drop. Beginning again from the modified current conservation relation, equation (A.1), this time insert the expressions for currents from equation (2.33):

$$\gamma_{\rm s} N_{\rm th,s} \exp\left[-\frac{V_{\rm GS}-\mu_{\rm s}}{k_B T_{\rm s}}\right] = \gamma_{\rm g} N_{\rm th,g} \exp\left[-\frac{V_{\rm GS}-V_{\rm G,0}-\mu_{\rm g}}{k_B T_{\rm g}}\right]\left(1+e^{-\upsilon/(1-\tau)}\right) \quad \text{(A.6)}$$

To begin, the previous equation is rearranged to group like-terms in the exponentials,

$$\exp\left[\frac{\mu_{\rm s}}{k_B T_{\rm s}} - \frac{\mu_{\rm g}+V_{\rm G,0}}{k_B T_{\rm g}}\right] = \frac{\gamma_{\rm g} N_{\rm th,g}}{\gamma_{\rm s} N_{\rm th,s}} \exp\left[\frac{V_{\rm GS}}{k_B T_{\rm s}} - \frac{V_{\rm GS}}{k_B T_{\rm g}}\right]\left(1+e^{-\upsilon/(1-\tau)}\right). \quad \text{(A.7)}$$

Next, take the natural log of both sides and use the identity: $\ln[A\times B]=\ln[A]+\ln[B]$,

$$\frac{\mu_{\rm s}}{k_B T_{\rm s}} - \frac{\mu_{\rm g}+V_{\rm G,0}}{k_B T_{\rm g}} = \ln\left[\frac{\gamma_{\rm g} N_{\rm th,g}}{\gamma_{\rm s} N_{\rm th,s}}\right] + \left(\frac{V_{\rm GS}}{k_B T_{\rm s}} - \frac{V_{\rm GS}}{k_B T_{\rm g}}\right) + \ln\left[1+e^{-\upsilon/(1-\tau)}\right]. \quad \text{(A.8)}$$

Inserting the definition for the feedback parameter and the temperature drop further simplifies the expression to

$$\hat{\mu}_{\rm s} - \frac{\hat{\mu}_{\rm g}+\hat{V}_{\rm G,0}}{1-\tau} = -\hat{V}_{\rm GS}\left(\frac{\tau}{1-\tau}\right) + \ln\left[\frac{\gamma_{\rm g} N_{\rm th,g}}{\gamma_{\rm s} N_{\rm th,s}}\right] + \ln\left[1+e^{-\upsilon/(1-\tau)}\right], \quad \text{(A.9)}$$

where the ($\hat{}$) indicates the quantity is normalized to the source temperature. Using the expressions for the number of thermally excited atoms in the ensemble, equation (2.30), the critical temperature, equation (2.8), and the thermal atom collision rate, equation (2.34), the ratio γN_{th} factors simplifies to

$$\begin{aligned}\frac{\gamma_{\rm g} N_{\rm th,g}}{\gamma_{\rm s} N_{\rm th,s}} &= \left(\frac{T_{\rm g}}{T_{\rm s}}\right)^5 \frac{1+\frac{\zeta(2)}{\zeta(3)}\frac{\mu_{\rm g}}{k_B T_{\rm g}}}{1+\frac{\zeta(2)}{\zeta(3)}\frac{\mu_{\rm s}}{k_B T_{\rm s}}}, \\ &= (1-\tau)^4 \frac{1-\tau+\frac{\zeta(2)}{\zeta(3)}\hat{\mu}_{\rm g}}{1+\frac{\zeta(2)}{\zeta(3)}\hat{\mu}_{\rm s}}.\end{aligned}$$

Finally, one obtains the expression for the chemical potential drop,

$$\begin{aligned}\hat{\mu}_{\rm sg} &= (1-\tau)\ln\left[(1-\tau)^4\left(1+e^{-\frac{\upsilon}{1-\tau}}\right)\right] - \tau\left(\hat{V}_{\rm GS}-\hat{\mu}_{\rm s}\right) \\ &+ (1-\tau)\ln\left[\frac{1-\tau+\frac{\zeta(2)}{\zeta(3)}\left(\hat{\mu}_{\rm s}-\hat{V}_{\rm G,0}-\hat{\mu}_{\rm sg}\right)}{1+\frac{\zeta(2)}{\zeta(3)}\hat{\mu}_{\rm s}}\right], \quad \text{(A.10)}\end{aligned}$$

after replacing the normalized gate chemical potential by $\hat{\mu}_{\rm g} = \hat{\mu}_{\rm s} - \hat{V}_{\rm G,0} - \hat{\mu}_{\rm sg}$.